Direct writing of Josephson junctions in superconducting nitrides with focused helium ion beam

Master's thesis, 1.7.2020

Author:

AKI RUHTINAS

Supervisor:

ILARI MAASILTA

UNIVERSITY OF JYVÄSKYLÄ
DEPARTMENT OF PHYSICS

Abstract

Ruhtinas, Aki
Direct writing of Josephson junctions in superconducting nitrides with focused helium ion beam
Master's thesis
Department of Physics, University of Jyväskylä, 2020, 133 pages

Direct writing of Josephson junctions using focused ion beam in YBCO thin films was demonstrated by Cybart et al. in 2015. This method could possibly simplify the fabrication of Josephson junctions for superconducting devices as well as provide versatile tool to investigate the physics of disorder-driven superconductor-insulator transition (SIT).

In this thesis this method is used to locally control the SIT in superconducting nitride thin films via disorder induced by the helium ion beam, and we demonstrate how this can be used in Josephson junction fabrication. Here high quality superconducting thin films of NbN, TiN and NbTiN grown with an infrared pulsed laser deposition (PLD) technique are used for the device fabrication. To our knowledge, this is the first time when superconducting niobium titanium nitride is deposited with pulsed laser deposition. During this project some modifications and improvements to the PLD setup were made, and they are briefly discussed in the thesis.

Low temperature measurements of the fabricated samples revealed that in all of the studied nitrides superconductivity can be suppressed by helium ion irradiation, with higher helium ion fluence resulting in a lower critical temperature T_c. This controllable T_c suppression combined with the high spatial resolution of the helium ion microscope was proven to enable successful fabrication of SNS-type Josephson junctions with highly tunable weak links.

Most promising candidate among the three superconducting nitrides seems to be NbTiN, because of its high T_c ($15.3\,\mathrm{K}$) and low resistivity. In addition, we demonstrate that NbTiN thin films can be pushed to the insulating side of the SIT with a high enough helium ion fluence. Thus, fabrication of insulating barrier SIS Josephson junctions was also shown to be possible. However, in all of the fabricated devices exhibiting clear insulating behaviour, critical current was suppressed.

Fabrication of Josephson junctions with direct writing has not been previously reported on conventional low temperature superconductors, and this work could open up new exciting possibilities in Josephson junction fabrication in the future. Suitable acronym for this new kind of device could be Disordered weak link Josephson Junction (dJJ).

Keywords: disorder, nitride, superconductor-insulator transition, Josephson junction, helium ion beam

Tiivistelmä

Ruhtinas, Aki
Josephsonin liitosten suorakirjoitus heliumionisuihkulla suprajohtavissa nitrideissä
Pro gradu -tutkielma
Fysiikan laitos, Jyväskylän yliopisto, 2020, 133 sivua

Vuonna 2015 Cybart et al. osoittivat että Josephsonin liitoksia voi tehdä kuvioimalla suoraan heliumionisuihkulla YBCO ohutkalvoja. Tämä menetelmä on hyvin lupaava, sillä se voisi mahdollistaa Josephsonin liitosten valmistamisen aikaisempaa yksinkertaisemmalla menetelmällä. Lisäksi tätä menetelmää voisi mahdollisesti käyttää suprajohde-eriste transition tutkimiseeen.

Tässä tutkielmassa fokusoitua heliumionisuihkua käytetään tuottamaan epäjärjestystä nitridiohutkalvoihin ja näin lokaalisti kontrolloimaan suprajohde-eriste-transitiota tällä alueella. Tämän menetelmän osoitetaan soveltuvan Josephsonin liitosten tekemiseen suprajohtavissa nitrideissä. Tässä työssä käytetyt suprajohtavat TiN, NbN ja NbTiN ohutkalvot kasvatetaan pulssilaserkasvatuksella(PLD), ja huomionarvoista on että tämä on ilmeisesti ensimmäinen kerta kun NbTiN ohutkalvoja kasvatetaan PLD:n avulla. Tämän projektin aikana PLD-laitteistoa paranneltiin, ja nämä muutokset käydään läpi tässä tutkielmassa.

Valmistetut näytteet karakterisoitiin matalan lämpötilan mittausten avulla. Kaikissa tutkituissa nitrideissä suprajohtavaa kriittistä lämpötilaa voitiin laskea heliumionisuihkun avulla, ja lasku oli sitä suurempi mitä isompi annos heliumionisuihkua materiaaliin kohdistettiin. Tässä työssä osoitetaan että tätä kontroilloitua T_c:n laskua voidaan käyttää SNS-tyyppisten Josephsonin liitosten valmistamiseen, jolloin heikon linkin ominaisuuksia voidaan säätää hyvin paljon.

NbTiN osoittautui kaikista lupaavimmaksi materiaaliksi, koska sillä on korkea T_c (15.3 K) ja pieni resistiivisyys. Lisäksi tässä tutkielmassa osoitetaan että NbTiN voidaan saada eristäväksi kohdistamalla siihen tarpeeksi suuri annos heliumioneja, jolloin myös SIS-tyypin liitoksia voidaan tehdä. SIS-liitoksia voitiin tehdä onnistuneesti, mutta kaikissa selvästi eristävissä näytteissä kriittinen virta oli suppressoitu.

Aikaisemmin ei ole raportoitu Josephsonin liitosten valmistamista nitrideissä suorakirjoittamisen avulla, ja tämä työ voikin avata uusia mahdollisuuksia

Josephsonin liitosten valmistukseseen tulevaisuudessa. Sopiva lyhenne tälläiselle uudelle Josephsonin liitokselle voisi olla mahdollisesti "Epäjärjestyneen heikon linkin Josephsonin liitos" eli dJJ.

Avainsanat: Epäjärjestys, nitridi, suprajohde-eriste transitio, Josephsonin liitos, heliumionisuihku

Preface

The work presented in this Master's thesis has been carried out at the Department of Physics and Nanoscience Center at the University of Jyväskylä.

First and foremost, I would like to thank my supervisor Prof. Ilari Maasilta for his excellent guidance along the project and for the opportunity to work in his magnificent group. I am grateful for the interesting projects I have been able to work with, and the topic of this thesis was especially interesting and inspiring.

As always, a lot of people have helped me during this project. Technical support from the laboratory engineers Dr. Kimmo Kinnunen and Mr. Tarmo Suppula has been crucial throughout the project, and is gratefully acknowledged. Thanks to Dr. Pasi Myllyperkiö for his help during the modifications of the pulsed laser deposition system, and to Prof. Tero Heikkilä for insightful discussions on the theoretical aspects of the thesis. I highly appreciate help of Mr. Teemu Loippo and Dr. Kai Arstila with the helium ion microscopy. I would also like to thank all the group members, particularly Mr. Geng Zhuoran and Mr. Tatu Korkiamäki, for their help and ideas during the project.

Topic of this thesis consists of several aspects of my past projects I have been honoured to be involved in, thus special thanks to Mr. Andrii Torgovkin for introducing me to the pulsed laser deposition and to the experimental nanoscience, and to Dr. Olivier Bourgeois and Dr. Tuyen Nguyen from Institut Néel, Grenoble, for introducing me to the fascinating world of superconductor-insulator transitions.

I am most grateful to my grandma, parents and my little brother for their support and encouragement, and I am thankful for support from all of my friends.

Jyväskylä, July 2020

Aki Ruhtinas

Contents

1 Introduction

During the first quantum revolution the universe proved to behave very differently from what classical mechanics dictates. The new emerged field of quantum mechanics predicted a lot of counter-intuitive and mind-boggling results that were eventually verified by experiments. While deep understanding of the theory was, and still is, inadequate and unsatisfactory, quantum mechanics has enabled detailed calculations and exceptionally accurate predictions on different physical systems. These have ultimately lead on to such a technological breakthroughs as laser and microprocessors.

During last few decades we have entered the era of the second quantum revolution. As the field of quantum mechanics has matured, we have now ingredients and knowledge to build the next generation devices that use directly the bizarre quantum phenomena such as entanglement and superposition. For example, quantum computing could potentially increase our computational resources to an unparalleled level, and quantum sensing and information could change the way we perceive the universe and communicate in everyday life.

However, this revolution needs hardware to be successful. One platform that can be used for quantum devices is superconducting electronics, which is currently most used and promising candidate for quantum computing and information. Also, many state of the art detectors and measurement devices are constructed using superconducting electronics. Operation of most, if not all, of these devices are based on the basic component of the superconducting electronics: the Josephson junction. This thesis focuses on development and characterization of Josephson junctions fabricated with new method, helium ion beam direct writing (Figure 1).

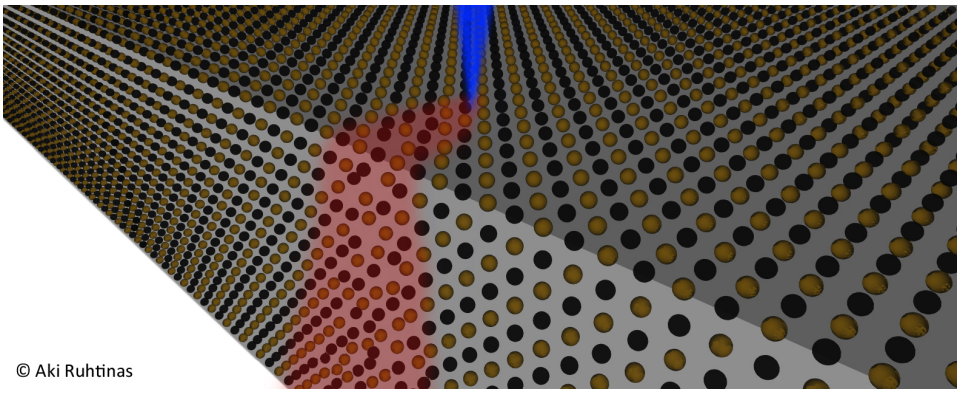

Figure 1. Artistic impression of the focused helium ion beam creating a disordered region to the TiN crystal lattice. This is the working principle of the Josephson junction fabrication in this project.

1.1 Introduction to Josephson junctions

Before we dive more into the physics of superconductivity and Josephson junctions later on in section 2, let us briefly take a glance on the topic. These junctions are basic components in superconducting electronics, and are used for example in voltmeters [1], voltage standards [2], thermometers [3], SQUID magnetometers [1], sensitive detectors [4],superconducting qubits [5], [6] and superconducting computing (RSFQ logic) [7], to name a few. When this component is so widely used, it is easy to imagine how there is an enormous demand on new and better fabrication techniques.

Because of the wide usage of Josephson junctions, fabrication of these junctions is well established. The most common type of junctions have two superconducting aluminium electrodes separated by a thin aluminium oxide barrier to form the so called SIS type Josephson junction. The advantage in using these materials is that aluminium has a stable native oxide that is easy to fabricate by simple oxidation, resulting in high quality barriers. Other materials can also be used, but the fabrication is done via more or less the same fabrication route, where a thin insulating barrier is formed between two overlapping electrodes (Figure 2).

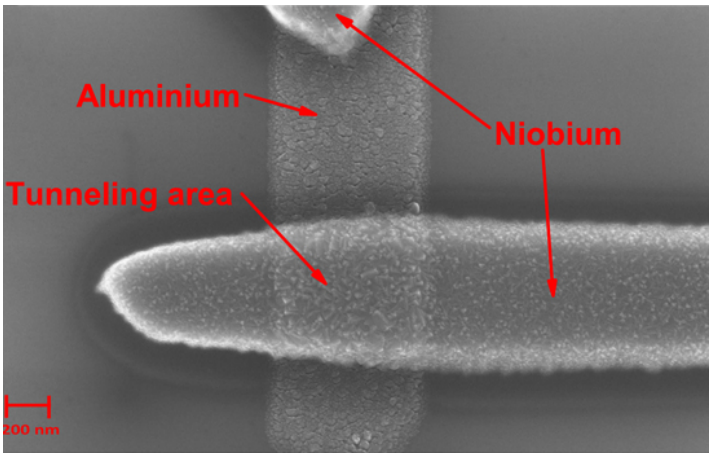

Figure 2. The usual way to fabricate Josephson junctions with an insulating barrier, here for example a slightly unconventional Al-AlOx-Nb Josephson junction. An insulating barrier is formed between two overlapping electrodes (in this case Al and Nb) by oxidation. Figure adapted from Ref. [8], reprinted with permission. ©2016 IOP Publishing Ltd.

This conventional fabrication scheme of SIS-type Josephson junctions possesses several disadvantages. Usual superconductor aluminium has a low superconducting critical temperature, which limits its usage to very low temperatures ($\sim$ 100 mK), and also its small superconducting gap is a problem in some applications. This can be circumvented with the use of superconductors with higher T_c, such as Nb, but this possesses another problems regarding for example how the barrier is made. In addition, with the conventional SIS fabrication scheme, tuning of barrier properties is especially difficult, and it is often restricted only to a barrier thickness control.

For low temperature superconductors, SNS Josephson junctions are most often fabricated using stack of normal metal and superconducting films, where superconductor is removed from a certain area and thus two superconducting electrodes are connected only by the underlying metal layer. With this method one can produce high quality reproducible SNS junctions, however high characteristic voltage $I_C R_N$ (product of the critical current I_c and the normal state resistance R_N) values needed for some applications are often difficult to obtain. Also geometry is not as ideal as truly planar geometry would be.

While the fabrication of Josephson junctions might be relatively straightforward

when the usual geometries with overlapping electrodes is used, fabrication of Josephson junctions with a planar geometry is extremely difficult, in particular when conventional low temperature superconductors are used. Thus, there is a need for a method where Josephson junctions can be easily and reproducible fabricated using simple fabrication techniques in the planar geometry. This is what is the aim of this thesis, and here we are using a helium ion beam to create disorder to a localized area, creating thus a Josephson junction. The ability to use this kind of "direct writing" of Josephson junctions for conventional low temperature superconductors could open up new interesting possibilities for fabrication of different superconducting nanoelectronics. If direct writing would prove to be easy, fast and reproducible way to fabricate Josephson junctions, it could potentially revolutionize the way superconducting nanoelectronics is fabricated.

1.2 Helium ion beam direct writing for high temperature superconductors

Before helium ion beam direct writing, for high temperature superconductors (HTS) planar Josephson junctions has been fabricated using grain boundaries. This fabrication method has produced the most reliable, simple, and most frequently used Josephson junctions for high-Tc superconductors [9]. Because the fabrication of Josephson junctions using conventional microfabrication techniques in high-Tc superconductors is very difficult, there has been a demand for simpler approach. SNS type Josephson junctions has previously been fabricated with both electron beam irradiation [10], [11] and masked ion beam irradiation [12], [13], but barrier dimensions were too big to create tunnel junctions.

When helium ion microscopes became available commercially in 2007, new possibilities in nanofabrication opened. With a commercial HIM one can achieve a beam diameter of 0.5 nm [14], which is small enough for tunnel junction fabrication. In 2015, utilising helium ion beam and disorder driven SIT transition in high temperature superconductor YBCO, Cybart et al. were able to produce Josephson junctions by direct writing with HIM [15]. In their publication, they showed that with a helium ion fluence of $2 \cdot 10^{16}$ ion/cm^2 the Josephson junction was SNS-type, but with a fluence of $6 \cdot 10^{16}$ ion/cm^2, the junction was showing SIS-type characteristics. As a result, they made succesfully Josephson junctions with $I_c R_N$

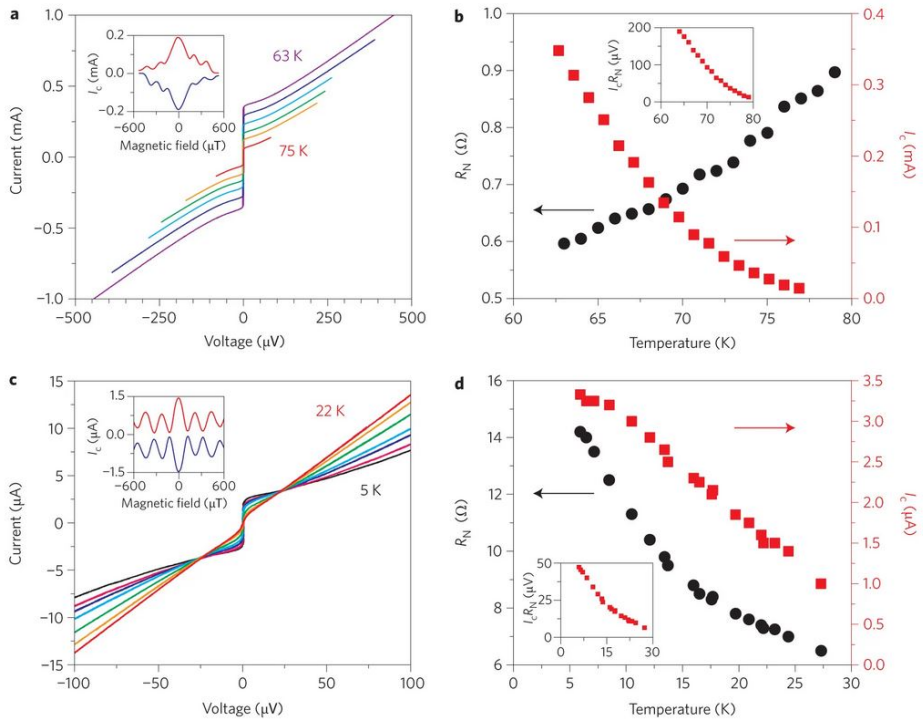

Figure 3. Electrical transport measurements for the Josephson jucntions made by helium ion beam direct writing. a) Current–voltage characteristics of a SNS Josephson junction, b) I_c, R_N and their product for the junction. Similarly in c) and d), there is same graphs for an SIS Josephson junction. Increase in the barrier resistance when the temperature is decreased (d) implies insulating barrier. Insets in the leftmost figures show Fraunhofer diffraction pattern for the critical current in a magnetic field applied perpendicular to the film. Figure from Ref. [15], reprinted with permission. ©2015 Springer Nature.

values between 50 and 200 μV, approximately an order of magnitude higher than with masked ion irradiated junctions and roughly the same order as with other HTS Josephson junctions [15], see Figure 3.

After the direct writing with He beam for a HTS superconductor was proven to be a viable method to produce highly tunable Josephson junctions, there has been efforts to apply this in the fabrication of nanoscale superconducting quantum interference devices (SQUIDs)[16]–[19]. In the most recent publication from February 2020 by Li et al.[19] they used a 35 nm thick YBCO film, which they irradiated with helium ion beam using a helium ion microscope. In Figure 4, we can see a nano-

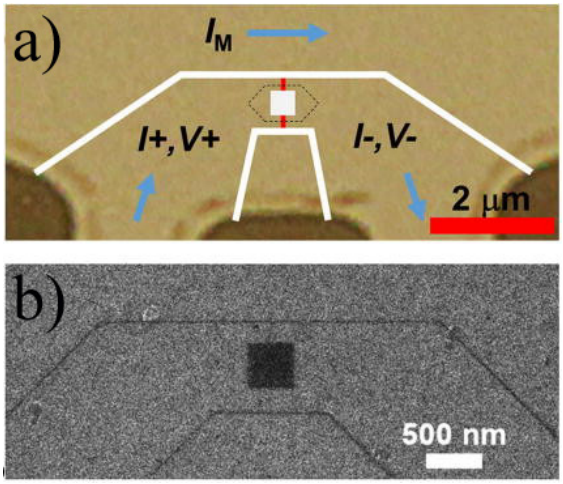

Figure 4. Nanoscale SQUID fabricated with a helium ion beam. In a) there are white lines that are used to define the SQUID geometry, irradiated with a high fluence, and red lines that define the Josephson junctions, irradiated with a smaller fluence and a smaller beam diameter. In b) a HIM image of the ready SQUID device is shown. Figure adapted from Ref. [19], licensed under a CC BY license.

scale SQUID fabricated with this technique. An irradiation of $\sim 8 \cdot 10^{17}$ ion/cm^2 was used to define the structure, and a smaller fluence of $\sim 6 \cdot 10^{16}$ ion/cm^2 was used to define a very small insulating barrier to form the Josephson junctions.

Beside YBCO, there has been some research conducted with other materials, namely MgB_2. In 2018, Kasaei et al. used helium ion beam direct writing to define Josephson junctions in MgB_2 [20]. In their work, direct writing with two helium ion fluences were studied, $9 \cdot 10^{15}$ ion/cm^2 and $2 \cdot 10^{16}$ ion/cm^2, and direct writing with both of the fluences showed Josephson coupling that is characteristic of a highly uniform barrier. Thus they were able to fabricate high quality planar SNS Josephson junctions, but fabrication of SIS junctions was not reported in that study.

There has been only very few published research concerning the use of ion beams in general in suppression of superconductivity, and to our knowledge only two in nitrides [21], [22]. In the publication by Prikhodko et al. [21], NbN was irradiated with a composite ion beam of protons and oxygen ions which resulted in the reduction of T_c. However, in this study the reduction was mainly due implantation of oxygen ions to the lattice and not by disorder, and thus

mechanism of the T_c suppression is slightly different.

During the very end of this thesis project, a new work concerning fabrication of NbN nanowires with HIM was published as a preprint [22]. In this paper, a helium ion beam from a helium ion microscope was used to suppress superconductivity, and thus a NbN nanowire could be defined by direct writing. In this research, they showed that superconductivity is suppressed below 4.2 K after an irradiation with $1 \cdot 10^{18}$ ion/cm^2, a similar result obtained in this thesis. As a conclusion, they showed that it is possible to fabricate a nanowire with this technique, and that this could be useful a method particularly for the fabrication of superconducting nanowire single-photon detectors (SNSPDs).

2 Superconductivity

Superconductivity, discovered already in 1911 by H. Kamerlingh Onnes in pure mercury, is an intriguing phenomena where material becomes perfect electrical conductor at sufficiently low temperatures. In 1933, Meissner and Ochsenfeld found that superconductors are not just perfect conductors, but material in superconducting state demonstrates Meissner effect: it behaves like a perfect diamagnet and expels external magnetic fields [1]. After these discoveries, the microscopic theory of superconductivity remained an unsolved puzzle until 1950s and 1960s when surprisingly complete and solid theoretical picture of the conventional superconductors was found. Later on, the discovery of high temperature superconductors in 1986 revealed a class of superconductors that can not be explained by these theories, raising huge theoretical and experimental interest towards superconductivity that is continuing to date. Here, we are dealing with conventional superconductors, so let us quickly go through the microscopic theory of superconductivity.

2.1 BCS theory

In 1956 Leon Cooper made a revolutionary prediction: for an arbitrarily weak electron–electron attraction, a two-particle bound state is formed and this state will destabilize the Fermi surface. This is the foundation of microscopic theory of superconductivty, the celebrated BCS theory[23] constructed by Bardeen, Cooper and Schrieffer. In conventional superconductors the origin of this attractive interaction is phonons. This phonon mediated attraction develops because there is a positive screening charge created by the ionic lattice around a moving electron, and this charge remains for a while after the electron has moved away. Therefore a retarded attraction is formed between electrons, driving the Cooper pairing (Figure 5). A correlated many-body state of the pairs condenses macroscopically, forming a Cooper pair condensate and the superconducting phase. Cooper pairing can be described by a pair potential, and for conventional superconductors which exhibit spin singlet pairing it is given by [24]

$$\Delta(\vec{r}) = \lambda(\vec{r})F(\vec{r}), \tag{1}$$

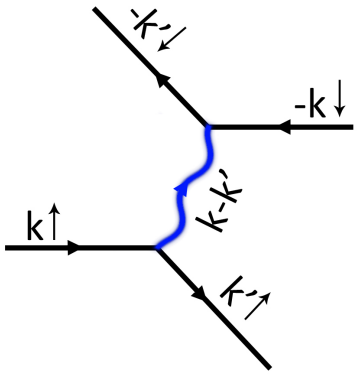

Figure 5. Virtual phonon exchange process responsible for the attraction between electrons in the BCS theory.

where $\lambda(\vec{r})$ is the strength of the attractive interaction and $F(\vec{r}) = \langle\psi_\downarrow(\vec{r})\psi_\uparrow(\vec{r})\rangle$ is correlation function for an electron pair. Thus pair potential is the order parameter for the superconducting phase transition, and its absolute value gives the gap in the quasiparticle excitation spectrum. An effective mean field Hamiltonian in the presence of the attractive interaction and spin singlet pairing is [1]

$$H_{eff} = \int d\vec{r} \sum_\sigma \Psi^\dagger_\sigma(\vec{r}) H_0 \Psi_\sigma(\vec{r}) + \int d\vec{r}[\Delta(\vec{r})\Psi^\dagger_\uparrow(\vec{r})\Psi^\dagger_\downarrow(\vec{r}) + \Delta^*(\vec{r})\Psi_\uparrow(\vec{r})\Psi_\downarrow(\vec{r})], \tag{2}$$

$$H_0 = \frac{1}{2m}\left(\frac{\hbar}{i}\nabla - \frac{e\mathbf{A}}{c}\right)^2 - U(\vec{r}) - \mu, \tag{3}$$

where $\Psi_\sigma(\vec{r}), \Psi^\dagger_\sigma(\vec{r})$ are the fermionic annihilation and creation operators in position space, respectively. H_0 is the single-particle Hamiltonian of the electron gas, where $\mathbf{A}$ is vector potential, $U(\vec{r})$ potential and μ chemical potential. When this Hamiltonian is diagonalized with a Bogoliubov transformation, one ends with the Bogoliubov-de Gennes equations [1]

$$\begin{pmatrix} H_0(\vec{r}) & \Delta(\vec{r}) \\ \Delta^*(\vec{r}) & -H_0^\dagger(\vec{r}) \end{pmatrix} \begin{pmatrix} u_n(\vec{r}) \\ v_n(\vec{r}) \end{pmatrix} = E_n \begin{pmatrix} u_n(\vec{r}) \\ v_n(\vec{r}) \end{pmatrix}, \tag{4}$$

where $u_n(\vec{r})$ and $v_n(\vec{r})$ are the coefficients for the Bogoliubov transformation and can be identified as probabilities that the Cooper pair is unoccupied or occupied, respectively. Unlike in the classical BCS treatment, Bogoliubov equations (Eg. (4)) can be used for spatially inhomogeneous superconductors, and therefore it is more

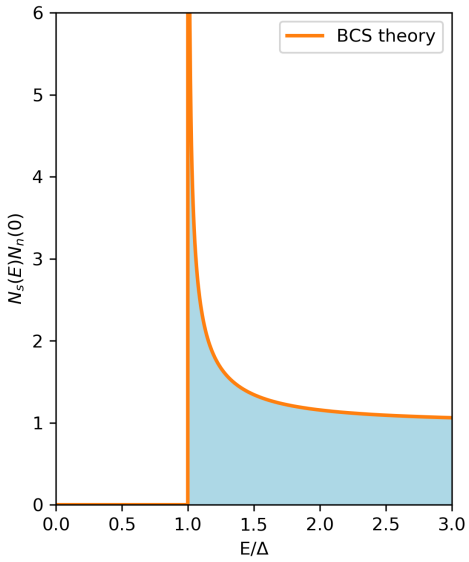

Figure 6. The density of states in a superconductor in BCS theory.

useful approach for the current purposes. The size of the superconducting gap can be derived from the BCS theory, and in weak coupling limit at zero temperature it is [1]

$$\Delta(T=0) = 1.764 k_B T_c, \tag{5}$$

while the temperature dependence in the same limit and near T_c is approximately [1]

$$\frac{\Delta(T)}{\Delta(0}) \approx 1.74\sqrt{1-\frac{T}{T_c}}. \tag{6}$$

The density of states for the quasiparticle excitations is of the form [25]

$$N_s^*(E) = N_n(0)\left(\frac{E}{\sqrt{E^2-|\Delta|^2}}\right)\theta(E-|\Delta|), \tag{7}$$

where $N_n(0)$ is the normal state density of states at Fermi energy. The density of states is plotted in Figure 6 using Eq. (7). In practice, this is broadened for example by disorder, finite lifetime of quasiparticles and strong-coupling corrections, but these nonidealities can be modelled by introducing a Dynes parameter Γ [26] so that Equation (7) becomes

$$N_s^*(E) = N_n(0)\left|Re\left(\frac{E+i\Gamma}{\sqrt{(E+i\Gamma)^2-|\Delta|^2}}\right)\right|, \tag{8}$$

Often, it is useful to gain insights to relevant length scales involved in the system, and in superconductivity two of the most important length scales are the penetration depth λ_p and the coherence length ξ_0. The penetration depth describes the decay length of the magnetic field within the superconductor, while the coherence length can be understood as a size of a Cooper pair. Out of these two, the coherence length is more important for this project, because it is the characteristic length against which one should compare a possible weak link length. The coherence length of a superconductor is given by [24]

$$\xi_0^{clean} = \frac{\hbar v_F}{\pi|\Delta|}, \quad \xi_0 \ll l_{el} \tag{9}$$

$$\xi_0^{dirty} = \sqrt{\frac{\hbar D}{2|\Delta|}}, \quad \xi_0 \gg l_{el} \tag{10}$$

where the expressions are given in clean and dirty limits, respectively. Here l_{el} is the elastic mean free path against which ξ_0 needs to be compared in order to decide the correct limit. Determination of the Fermi velocity v_F or the diffusion constant D is somewhat nontrivial task, and coherence lengths were not measured here. For example, the coherence length of $Nb_{0.62}Ti_{0.38}N$ has been determined to be around 2.5 nm [27], while in NbN, the coherence length is of the order of 5 nm [27]. In titanium nitride, coherence length of 8.2 nm has been measured [28].

2.2 Josephson junctions

When superconducting electrodes are coupled by a weak link, there occurs a remarkable phenomenon called the *Josephson effect*, predicted theoretically by Brian Josephson in 1962 [29]. In the Josephson effect, Cooper pairs are tunnelling through a weak link.

Although the original prediction of Josephson was only for tunnel junctions, it turns out that it is a much more general effect taking place not only in insulating barriers, but also in the so called weak links. The requirement is that the coupling of the superconductors needs to be sufficiently weak that in the weak link there is sufficiently small probability to find Cooper pairs in that region. At the same time barrier needs to be thin enough so that tunnelling is possible.

In the Josephson effect, zero voltage supercurrent flows through the two superconducting electrodes, and in the simplest model vaid for tunnel junctions this

current is given by [1]

$$I = I_c \sin(\Delta\varphi), \tag{11}$$

where I_c is critical current of the junction and $\Delta\phi$ the phase difference of the two superconducting electrodes. Hence, current can flow even in the absence of a potential drop; this is often referred as the *dc Josephson effect*. If a voltage difference over the junction is maintained, then phase difference evolves as [1]

$$\frac{d}{dt}\Delta\varphi = 2eV/\hbar, \tag{12}$$

and solving this for a constant voltage yields

$$I = I_c \sin(\Delta\varphi(0) + 2eVt/\hbar), \tag{13}$$

thus producing an alternating current with a frequency of $f = 2eV/\hbar$ and an amplitude of I_c. Consequently, this is known as the *ac Josephson effect*. Altogether these effects make Josephson junctions to act as a nonlinear circuit elements, and this has opened up wide possibilities for their applications.

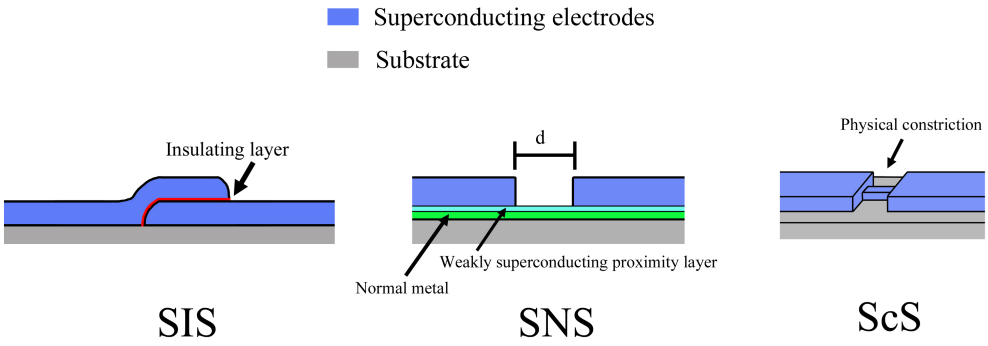

Figure 7. Schematics of three types of Josephson junctions made with conventional geometries.

A weak link between the superconducting electrodes can either be a normal metal (SNS junction), an insulator (SIS junction) or a physical constriction of the superconductor (ScS junction). Different types of junctions are presented in Figure 7. Here, we are interested in fabricating a weak link by disorder, and we are fabricating only first two kind of junctions. Junction with physical constriction can also be fabricated with the helium ion beam, but helium ion beam milling is a relatively well established technology and hence out of the scope of this project.

2.2.1 SIS tunnel junctions

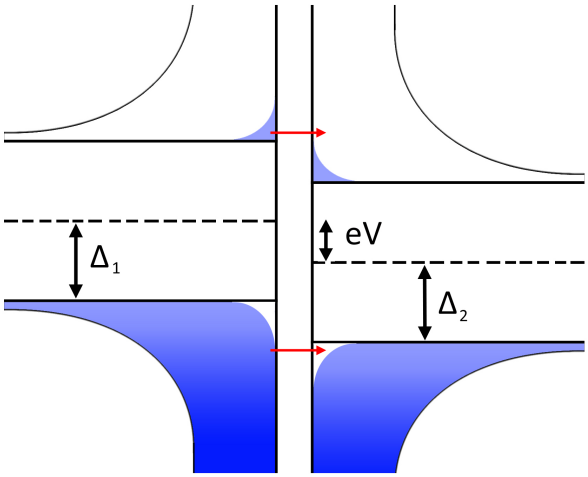

Figure 8. A diagram describing tunnelling through an insulating barrier separating two superconductors within semiconductor model. Superconductors on the left and right side of the barrier have gaps of Δ_1 and Δ_2, respectively. At zero temperature, current can flow only if $eV > \Delta_1 + \Delta_2$, but at T>0 thermally excited electrons and holes can tunnel (red arrows) with smaller voltages.

Two superconductors coupled by a thin tunneling barrier creates a SIS type of junction. Tunneling current between two electrodes can be calculated from a simple tunneling Hamiltonian [1], [30]

$$H_T = \sum_{\sigma\vec{k}\vec{q}} T_{\sigma\vec{k}\vec{q}} c^{\dagger}_{\vec{k}\sigma} c_{\vec{q}\sigma} + H.c, \tag{14}$$

where all the tunnelling barrier properties have been absorbed in the tunnelling matrix element $T_{\sigma\vec{k}\vec{q}}$. When Fermi Golden Rule is applied to Eq.(14) and the superconductor is represented by the semiconductor model [1] (Figure 8), the tunnelling current through the SIS junction is [1], [30]

$$I_{SIS} = \frac{4\pi e}{\hbar}|T|^2 N_1(0) N_2(0) \int_{-\infty}^{\infty} N_{1S}(E) N_{2S}(E+eV)[f(E,T) - f(E+eV,T)]dE \tag{15}$$

where T is a constant tunnelling matrix element, $N_{1,2}$ are the normal state densities of states and $N_{S1,2}$ are the normalized densities of states in superconducting phase. This equation does not take Josephson effect into account. When Josephson effect is considered, there is also a current contribution from Cooper pair tunneling at

zero voltage, and the equation for temperature dependence of the critical current is [31]

$$I_c R_n = \frac{\pi\Delta}{2e} \tanh\left(\frac{\Delta}{2k_B T}\right), \tag{16}$$

where R_n is resistance of the barrier.

2.2.2 RCSJ model

Although the equations described above are sufficient to characterize the zero voltage Josephson behaviour, for the finite voltage effects the so called RCSJ (resistively and capacitively shunted junction) model is often used. In RCSJ model, an ideal Josephson junction is shunted by a resistance R and a capacitance C, and thus the current is combination of three parallel channels [1]

$$I = I_{c0}\sin(\gamma) + V/R + C\frac{dV}{dt}. \tag{17}$$

where we have the gauge invariant phase difference γ defined by [1]

$$\gamma = \Delta\varphi - (2\pi/\Phi_0)\int \mathbf{A}\cdot d\vec{s}, \tag{18}$$

hence $\Delta\varphi$ and γ are the same at zero magnetic field. Eliminating V and using Equation (13) we have

$$\frac{I}{I_{c0}} = \frac{d^2\gamma}{d\tau^2} + \beta_c\frac{d\gamma}{d\tau} + sin(\gamma), \tag{19}$$

where

$$\tau = \sqrt{\frac{2eI_{c0}}{\hbar C}}t = \omega_p t, \tag{20}$$

where ω_p is the plasma frequency. We can also define quality factor $Q = \omega_p RC$, which is often expressed with alternative form using Stewart-McCumber parameter $\beta_c = Q^2$. Now, junctions can be divided to overdamped or underdamped junctions, depending on whether the junction exhibits a small or a large capacitance C, respectively. In the overdamped junctions where $Q \ll 1$, the DC current-voltage characteristics can be found by solving equation (19) in small Q limit [1]

$$V = R(I^2 - I_{c0}^2)^{1/2}. \tag{21}$$

When the capacitance C is large and the junction is underdamped, the current-voltage characteristics of the junction become hysteretic. However, one should be careful when interpreting the current-voltage characteristics, since hysteresis might be of the thermal origin [32].

2.2.3 SNS Josephson junctions

A Josephson weak link can also be metallic, and in this case a SNS type junction is formed. While in a SIS junction Josephson current was due tunneling, in the SNS case supercurrent passes through the weak link via the proximity effect [1]. Fact that supercurrent is passing through the weak link via the proximity effect rather than tunnelling adds more complexity to the problem, and usually one needs to consider the Usadel or Eilenberger equations for the SNS case [33]. For temperatures close to T_c (0.3<T/T_c<1), Likharev has worked out temperature dependence of I_cR_n [33]

$$I_cR_n = \frac{2}{\pi e}\frac{|\Delta|^2}{k_BT_c}\frac{L/\xi_N}{\sinh(L/\xi_N)}, \tag{22}$$

where L is the length of the normal metal and ξ_N is the normal metal coherence length given by

$$\xi_N = \sqrt{\frac{\hbar D}{2\pi k_BT}}, \qquad D = \frac{1}{e^2N(0)\rho_n}, \tag{23}$$

where $N(0)$ is the normal metal density of states at the Fermi level and ρ_n is the resistivity of the normal layer. Characteristic voltage of the SNS junction I_cR_n is often relevant parameter when quality of the junction needs to be estimated for use in different applications. For example, in rapid single flux quantum (RFSQ) circuits SNS junctions with high I_cR_n is preferred, as I_cR_n needs to be higher than $\sim 0.3\,\mathrm{mV}$ in order to operate RFSQ logic at $50\,\mathrm{GHz}$ frequency [34].

In the SNS junctions influence of normal metal length is relevant question. When normal metal layer is much thinner than coherence length junction behaves like ideal Josephson junction, but in long junctions behaviour is altered. In this case junctions should be of the order of coherence length, and thus it is not necessary to take into account effects related to long junctions. However reduced dimensionality of the junctions leads to important effects, especially when tunnel junctions are considered, and this is what we will next go through more in detail.

2.3 Phenomena unique to small junctions

With helium ion beam direct writing, one can decrease the size of the tunnel junctions down to really small dimensions, and up to some point it is actually easier to fabricate small junctions rather than big ones. Subsequently, in this project most of the tunnel junctions are rather small, and thus it is important to discuss the new phenomena arising when dimensions are decreased.

When the size of a junction is small enough, the charge of a single electron begins to matter. In suitable systems, the charging energy of a single electron, given by [35]

$$E_c = \frac{e^2}{C}, \tag{24}$$

where e is elementary charge and C capacitance, suppresses transported current through the structure at low enough temperatures and voltages. This effect can be observed for example when a conducting island is formed between two tunnel junctions in series or in small single junctions that are in highly resistive environment. Additionally, this Coulomb blockade effect arises not only in tunnel junctions but also in more transparent junctions, although in that case the effective charging energy is decreased significantly. [24], [35]

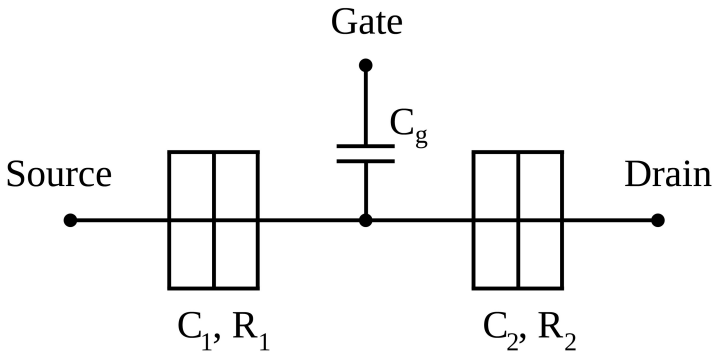

Figure 9. Schematic representing single electron transistor (SET).

The single electron transistor (SET) is one of the systems that hosts Coulomb blockade effects. These devices are versatile objects and are planned to be used in for example in ultra-low power electronics [36]. Direct writing of a single electron transistor with a focused ion beam has already been demonstrated [37], and there is ongoing EU-project attempting to fabricate SETs using ion beams [38]. Ion

beams are appealing alternative for SET fabrication because of the strict sub-5 nm size constraint for room temperature operation.

Single electron transistors consist of a conducting island formed usually between two tunnel junctions placed in series (Figure 9). When a voltage is applied between the drain and source, electrons are pushed through the conducting island. This current is suppressed by Coulomb blockade when gate voltage is zero, but when enough voltage is applied to the gate, the island goes to the non-blocking state and tunnelling of the electrons to the island is allowed. For a symmetric bias applied to both source and drain, a bias voltage of $V > (e - 2\text{mod}(Q_g,e))/C$ is needed for the current to flow. Charge Q_g is the so called gate charge and can be adjusted using the gate voltage V_g. When the gate voltage is changed, current trough the SET oscillates between almost zero and a finite value producing the so called Coulomb oscillations. [24], [39]

2.3.1 Tunnelling in electromagnetic environment

In most cases it is not necessary to take into account inelastic tunnelling, but this situation changes if small junctions are to be considered. Additionally, tunnel barriers are fabricated in this project by localizing electrons via disorder, and it is known that localized electrons can contribute to inelastic tunnelling [40], [41], making this topic even more relevant here. The effect of the environment on electron tunnelling is more prominent when charge relaxation is slow, and this environmental effect is often referred as dynamical Coulomb blockade.

Although energy loss in tunnelling is usually caused by the electron-electron interaction, often it is more useful to consider the interaction between an electron and electromagnetic excitations. The reason why this approach is justified is because a perturbation caused by tunnelling of an individual electron quickly propagates through the whole system, affecting a large number of electrons. Tunnelling in an electromagnetic environment can thus be described using the so called spin-boson model and the function $P(E)$ describing the probability for disposing energy E to the environment. [35], [42]

The exact form of the $P(E)$ function depends heavily on the environment, and these different environments can be classified using the power-law dependence of one-boson probability at low energies [42]:

$$P_1(E) \propto E^s (E_{cut})^{-1-s} \mathrm{e}^{-E/E_cut}, \tag{25}$$

where E_{cut} is a cut-off energy and parameter s can be used to classify environments, so that $s > -1$ is superohmic, $s = -1$ is ohmic and $s < -1$ is subohmic environment. The total probability can be found by plugging $P_1(E)$ into the equation [42]

$$P(E) = \int \frac{dt}{2\pi\hbar} \mathrm{e}^{-iEt/\hbar} \exp\left(\int dE' P_i(E')(\mathrm{e}^{-iE't/\hbar} - 1) \right). \tag{26}$$

Now, if single electron tunnelling is considered, the I-V curve can be found directly from equation [42]

$$I = G_T \int dE P(E) \left(\frac{E - eV}{\exp(\frac{E-eV}{k_B T}) - 1} - \frac{E + eV}{\exp(\frac{E+eV}{k_B T}) - 1} \right). \tag{27}$$

For finite temperatures this expression must be evaluated numerically. At zero temperature, I-V curves for a junction in high impedance environment are given by [42]

$$I(V) = \frac{eV - E_c}{eR_T} \Theta(eV - E_c), \tag{28}$$

where $\Theta(E)$ is step function. This corresponds to a Coulomb blockade that is broadened away upon increasing the temperature or decreasing the impedance of environment. For finite temperatures, $P(E)$ for this same high impedance limit is given by [42]

$$P(E) = \frac{1}{\sqrt{4\pi E_c k_B T}} \exp\left(\frac{-(E - E_c)^2}{4E_c k_B T} \right), \tag{29}$$

that can be used to calculate I-V curves numerically using Eq. (27).

In this project, we are especially interested in Josephson junctions where also Cooper pair tunnelling needs to be considered. This tunnelling rate is also altered as one would expect, and it turns out that now Cooper pair tunnelling is directly related to $P(E)$, so that current through the junction is given by [42]

$$I = \frac{eE_J^2}{2\hbar}(P(2eV) - P(-2eV)). \tag{30}$$

If the environmental resistance is high enough, E_J decreases when the voltage is decreased, and thus coherent supercurrent vanishes. This is due to voltage fluctuations caused by the environment, and these voltage fluctuations may destroy supercurrent at high temperatures even when environment has low impedance. [35]

2.4 MIM tunnel junctions

Tunnelling current between two normal metals separated by a thin insulator can be calculated using similar equation as (15), producing ohmic behaviour. Such equation holds only for small voltages, and for larger voltages nonlinearities appear. These nonlinearities can be discussed when for example Wentzel–Kramers–Brillouin (WKB) approximation is applied for the tunneling problem. This approximation is also used by Simmons model [43] predicting that in first order correction the tunnel junction conductance increases quadratically as

$$G = G_0 \left(1 + \frac{V^2}{V_0^2}\right), \tag{31}$$

where

$$V_0^2 = \frac{4\hbar^2 \phi_0}{e^2 m_e d^2} \tag{32}$$

$$G_0 = \frac{e^2 A \sqrt{2m_e \phi_0}}{h^2 d} \mathrm{e}^{-2d/\hbar\sqrt{2m_e\phi_0}}. \tag{33}$$

Here ϕ_0 is the effective height of the barrier, d the thickness of the barrier and A is the tunnel junction area.

Most commonly used material for tunnelling barriers is aluminium oxide, as one can fabricate high quality barriers consistently with AlOx. For these kind of junctions usual barrier height is $\sim 2\,\mathrm{eV}$ and thickness $\sim 1\,\mathrm{nm}$ [44], and these values are often obtained using Simmons model.

3 Quantum phase transitions

Even in highly quantum mechanical systems phase transitions are generally considered to be classical for $T > 0$; even though quantum mechanics might be needed to explain existence of the order parameter, its behaviour is governed by thermal fuctuations. At nonzero temperatures, the energy scale of thermal fluctuations is usually much larger than the typical energy scale of quantum fluctuations, and continuous phase transitions can be described by classical physics. [45]

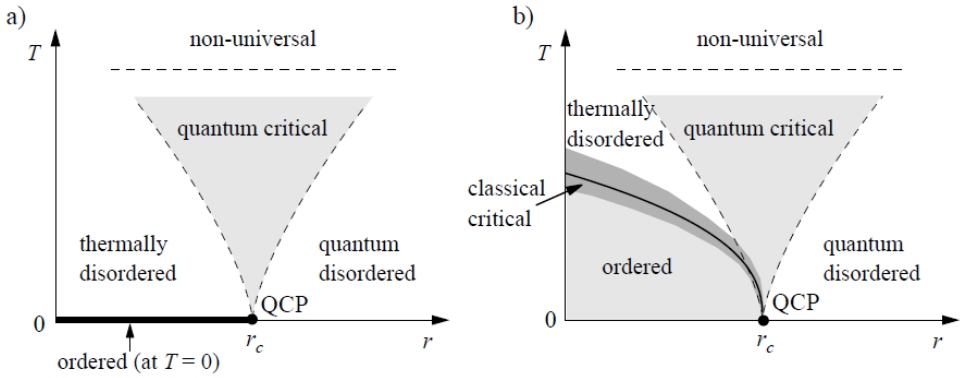

Figure 10. Two different phase diagrams in the vicinity of a quantum critical point. a) Order is present only at zero temperature and b) Order exists also at nonzero temperatures. Here r is the control parameter that tunes the system through the QPT, and T is temperature. Figure from Ref. [45], reprinted with permission. ©2003 IOP Publishing Ltd.

However, when temperature approaches absolute zero, quantum fluctuations start to play a role, and at zero temperature the classical phase transition is replaced by a quantum phase transition (QPT). In QPT, controlling a parameter of the Hamiltonian such as the magnetic field, the charge density or the disorder causes the material to undergo a phase transition driven by quantum fluctuations. This transition happens at $T = 0$ at the so called quantum critical point (QCP), where parameter r reaches its critical value r_c. At QCP, correlation length diverges and the energy scale vanishes. If this transition would happen only at zero temperature, the whole QPT discussion would be merely an academic peculiarity, but it turns out that this is not the case: in the vicinity of the quantum critical point, there is a quantum critical region where both type of fluctuations are important, and this

region may persist to relatively high temperatures. Thus the phase diagram in the vicinity of QCP is a result of interplay between these quantum and thermal fluctuations, and phase diagrams are qualitatively different depending on whether a long-range order exists at finite temperatures or not (Figure 10). [45]

Thus, quantum phase transitions are relevant also for nonzero temperature behaviour, and there has been an increasing effort to understand this phenomenon during last decades. Deep understanding of QPT could be useful in finding solutions to major open problems in condensed matter physics, such as non-Fermi-liquid behaviour and high temperature superconductivity.

3.1 Structural disorder in condensed matter systems

In physics, order is defined to be the presence of some symmetry or correlation in a many-body system. Symmetry is one of the most profound properties of a many body system; for each rule of symmetry there is a corresponding conservation law. The entropy, closely related to order or disorder of the system, is an important quantity in every thermodynamic process. Therefore it is not suprising that the presence of order and disorder affects the behaviour of the system often very dramatically.

Disorder can be either annealed or quenched. In the annealed disorder, the random degrees of freedom are ergodic, and the system is in a thermodynamic equilibrium. In the latter case, the random degrees of freedom are not evolving in time, i.e. system is "frozen" and not in thermodynamic equilibrium. This is the type of disorder we are interested in, more specifically the quenched structural disorder, where the translational symmetry of crystal lattice is broken. As often is the case, here this broken symmetry is related to a phase transition of the system.[45]

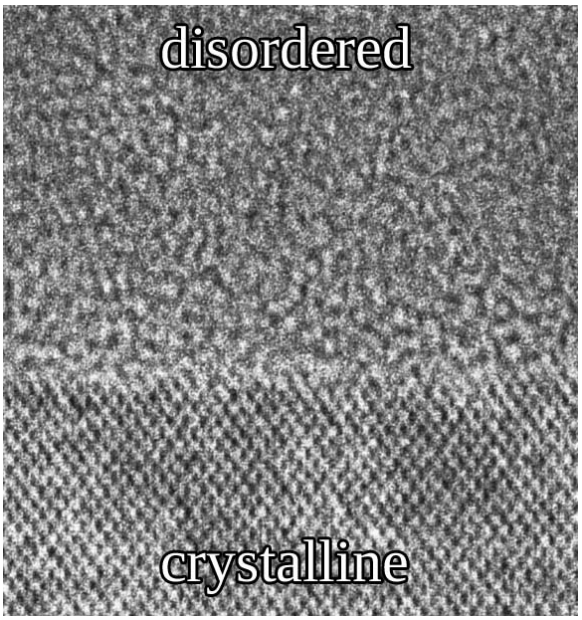

Figure 11. Ordered and disordered phases visible in cross-section high resolution transmission electron microscope (HRTEM) image of an amorphous Si thin film deposited on a crystalline Si substrate. Figure adapted from Ref. [46], reprinted with permission. ©2002 American Institute of Physics.

Structural disorder in condensed matter systems can either appear in the atomic scale, when disorder is considered to be homogeneous (Figure 11), or at larger length scales, when material is considered to be granular. The disorder we are dealing with in this study is presumably homogeneous, as a helium ion beam works in the atomic scale thus creating supposedly homogeneous disorder. However, nitride thin films are known to be polycrystalline and the ion beam is scanned with discrete steps, so the possibility of granularity in the samples cannot be completely ruled out.

But how can one quantify and measure the disorder level W? In the literature, the most often used definition for the disorder is the product of the Fermi wavevector k_F and the elastic mean free path l, so that $W \propto k_F l$ [47]. This can be estimated directly from the sheet resistance, given in the Drude model as [48]

$$R_{\square} = \frac{h}{e^2 k_F l}. \tag{34}$$

Because the measurement of the sheet resistance is straightforward, in the experimental section we will use $R_{\square}$ to quantify the level of disorder. The sheet

resistance is related to the resistance R by equation

$$R_{\square} = R\frac{W}{L}, \tag{35}$$

where W is width and L is length, thus a thickness measurement is not needed for the sheet resistance calculation. In the following sections, we will look at how disorder affects the material properties and the ground state of a system.

3.2 Metal-insulator transitions

Before discussing superconductor-insulator transitions, let us first review the theory of metal-insulator transitions (MIT). Theoretical models describing MIT have been introduced already long ago by Anderson [49], Mott [50] and others, but metal-insulator transitions are still not completely understood to date. Models describing MIT can be divided into models that describe either non-interacting or interacting electrons. Examples of the former case are the Anderson and the Peierls metal-insulator transitions, where the transition arises from increasing disorder. An example for latter case is the Mott transition, where the transition happens in an ordered system due decreasing electron concentration in the presence of a Coulomb electron-electron interaction.

Because here we are interested in systems with a strong random potential and disorder driven transitions, the assumption is that we are mainly dealing with Anderson type systems. However, interactions probably play some role in the metal-insulator transition. The influence of interactions in the presence of strong disorder is not completely understood to date, although there has been effort to construct theories with interactions taken into account [51].

3.2.1 Anderson localization

In 1958, Philip W. Anderson made a prediction that the electron wave function in a sufficiently strong random potential may be profoundly altered [49]. Anderson described this effect with a tight-binding Hamiltonian

$$H = \sum_i \epsilon_i c_i^\dagger c_i - g \sum_{\langle ij \rangle} (c_i^\dagger c_j + c_j^\dagger c_i^\dagger), \tag{36}$$

where the last sum goes over the nearest neighbour sites. Here g is the hopping amplitude between sites and (c_i,$c_j^\dagger$) are the fermionic creation and annihilation operators. Disorder is introduced in this model in such way that the on-site energies ϵ_i are independent random variables uniformly distributed within $[-W/2,W/2]$. In the absence of disorder, the Hamiltonian (36) is translationally invariant, and the solutions are of the form of plane waves. Hence the electronic states are extended, i.e. delocalized, as usual. However in the presence of strong disorder ($g/W \to 0$), the envelope of the wavefunction decays exponentially from a point in space [47]:

$$|\psi(\vec{r})| \sim \mathrm{e}^{-|\vec{r}-\vec{r}_0|/\xi_{loc}}, \tag{37}$$

where $\xi_{loc} \sim l\mathrm{e}^{k_f l}$ is the localization length. Now, if the Fermi energy is in the region of localized states, zero temperature conductivity will vanish, whereas with the extended states there is a finite zero temperature conductivity. Instead of disorder, one can also vary the energy of eigenstates and determine the critical energy at which the transition from a metal to an insulator occurs - this point is often referred to as the mobility edge E_m. [47]

As the Anderson model is difficult to use in dimensions over 1D, in 1970s Thouless and co-workers developed the so called scaling theory of localization to describe the effects in higher dimensions. The scaling theory works well in systems with a strong uncorrelated random potential and time-reversal symmetry, and the theory predicts that electron localization is a result of coherent interference between electron waves. This interference eventually builds up at long distances, and ultimately produces the disorder-driven metal–insulator transition. Quantum mechanical treatment of the intereference reveals that the probability for an electron to return to its starting point is enhanced in random media: quantum mechanics doubles the probability for electrons to bounce back compared to classical electrons. [25], [47]

Localization is very sensitive to the dimensionality, and while quantum corrections for the conductivity are finite in three dimensions, these corrections diverge in two or lower dimensions. This can be shown with the scaling theory. In the scaling theory, conductance G is normalized to a dimensionless parameter g, so that

$$g(L) = \frac{G(L)}{e^2/\hbar}, \tag{38}$$

and this dimensionless g satisfies the scaling equation [47]

$$\frac{d\ln(g(L))}{d\ln(L)} = \beta(g), \tag{39}$$

where $\beta(g)$ is the scaling function. With a large g, the Drude model can be used, but when $g \to 0$, $g(L)$ decays exponentially and $\beta(L) \sim -\ln(g)$. When different dimensions are analysed, it appears that for $d = 3$ there is critical conductance g_c, below which the disorder driven metal-insulator transition arises. However, for $d \leq 2$ no matter how weak the disorder is, electrons are always localized and the material becomes an insulator. The absence of a metallic phase in two dimensions is still under a debate, as some evidence on anomalous "Bose metal" phase in 2D exists [52].

The insulating state can be seen from the weak localization correction [25]: if inelastic scattering is neglected, the total conductivity with the weak localization correction for two dimensions

$$\sigma \approx \sigma_0 \left[1 - \frac{1}{2\pi k_f l} \ln\left(\frac{L}{l}\right) \right], \tag{40}$$

where L is the size of the system. In length scales that are in the vicinity of the localization length ($L \sim l\mathrm{e}^{k_f l}$), conductivity is always of the order of $e^2/\hbar$, but at longer scales the system behaves as an insulator [25].

3.2.2 Conductivity of localized electrons

Understanding the behaviour of the resistance as a function of temperature in localized electron systems would be useful for this study. Hence, we will now consider a simple model that describes the conductivity of localized electrons [53], where the density of states consists of localized electrons below the mobility edge E_m, and extended electrons above the mobility edge. The conductivity of this system depends on the relative positions of the Fermi energy E_F and E_m, and it is proportional to electron concentration above the mobility edge. Therefore we have

$$\sigma = \sigma_0 \mathrm{e}^{-(E_m - E_F)/k_B T}. \tag{41}$$

If the Fermi energy is below but near the mobility edge, in this case conductivity is dominated by thermally excited electrons. However, if E_F is below E_m by more than few $k_B T$, conductivity is due electron hopping between the localized states via a tunneling process. As the wave functions decay exponentially as in Eq. (37), the probability for hopping between sites i and j depends exponentially on distance r_{ij}. The hopping process happens from an occupied to a unoccupied state, and the probability of such process is given by [53]

$$P_{i\to j} \propto \mathrm{e}^{-\alpha|r_{ij}|}\mathrm{e}^{-(E_i - E_j)/k_B T}, \tag{42}$$

where α describes the decay of the wavefunction. If one assumes a constant density of states $D(E)$ near E_F, and takes into account condition for the initial state to be in a sphere of radius R, jumps are allowed if

$$E < E_{max} = E_j - \frac{3}{4\pi R^3 D(E_F)}, \tag{43}$$

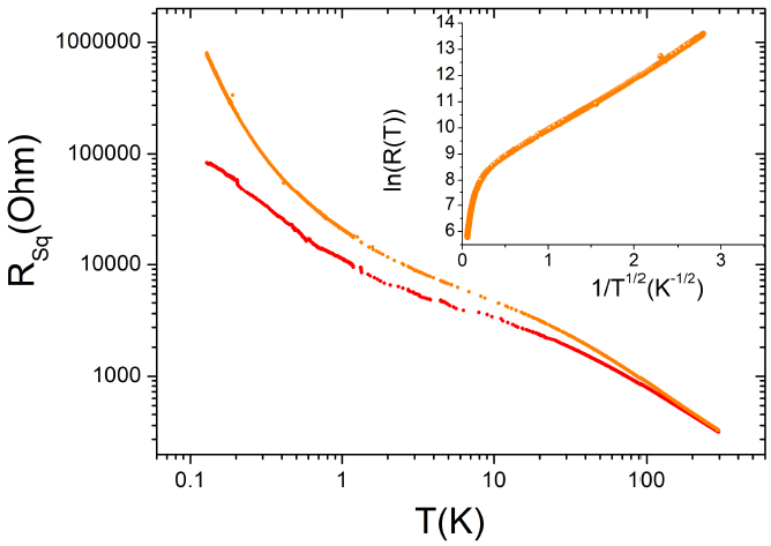

Figure 12. The temperature dependence of the sheet resistance in two insulating niobium nitride thin film samples made for resistive thermometry. The exponential increase in the resistance as the temperature decreases suggests that the system consists of localized electrons. Measurement was performed by the author, figure published in Ref. [54].

where $r_{ij} < R$. Now the total conductivity is

$$\sigma \propto \mathrm{e}^{-\alpha R} \int_{-\infty}^{E_{max}} \mathrm{e}^{-(E_j - E)/k_B T} dE \propto \mathrm{e}^{-\alpha R} \mathrm{e}^{-3/4\pi R^3 D(E_F) k_B T}. \tag{44}$$

Minimizing the exponent gives the optimal jump distance R_m, and when this is inserted back into Equation (44), one obtains temperature dependence of conductivity:

$$\sigma(T) = \sigma_0 \mathrm{e}^{-(T/T_0)^{1/4}}, \qquad T_0 = \frac{(4\alpha)^3}{9\pi D(E_F) k_B}, \tag{45}$$

where α is unknown numerical coefficient. This is the Mott variable range hopping prediction. Here constant density of states near E_F was assumed, but this is not true. Efros and Shklovskii were able to calculate energy dependence in the vicinity of E_F, and found that so called Coulomb gap is formed in the energy spectrum [55]. When this is taken into account to the calculation presented above, conductivity is

$$\sigma(T) = \sigma_0 \mathrm{e}^{-(T/T_0)^{1/2}}, \qquad T_0 = \frac{e^2}{\kappa \xi_{loc}}, \tag{46}$$

where κ is the dielectric constant and ξ_{loc} is the localization length. In both equations, comparison to experiments should be done by fitting σ_0 and T_0 to the experimental data. In Figure 12 there is resistance as a function of temperature for two insulating niobium nitride samples made for resistive thermometry, showing typical behaviour of localized electrons.

3.3 Superconductor-to-insulator transition

A famous prediction made by Philip W. Anderson in 1959 states that disorder does not considerably affect the superconducting critical temperature [56]. The explanation behind this so called Anderson theorem is that Cooper pairs are formed from time-reversed eigenstates, and the density of these states is not altered drastically by disorder. This picture applies in a semi-classical approximation, when $k_f l \gg 1$ and disorder is weak. However when disorder is strong and $k_f l \sim 1$, it turns out that there is significant suppression of superconductivity, and ultimately superconductor-to-insulator transition (SIT). This transition is a type of quantum phase transition, and the transition can be driven not only by disorder, but also by the magnetic field and the charge density. [45], [57], [58]

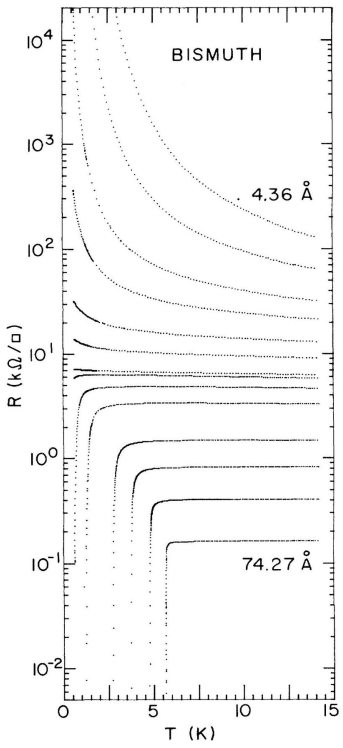

Figure 13. SIT transition in ultrathin homogeneous bismuth films. A precise thickness control is achieved by vapour depositing films *in situ* on a liquid helium cooled Ge substrate. Ultrathin films exhibit a direct transition from an insulator to a superconductor upon increasing thickness and thus decreasing disorder. Quantum critical point is roughly at R_q. Figure from Ref. [59], reprinted with permission. ©1989 American Physical Society.

Usually SIT is studied by adjusting the film thickness (disorder driven SIT) or changing the magnetic field (field driven SIT). An example of the former type of a measurement is the classical experiment carried out by Haviland et al. in 1989, where they showed a clear disorder driven SIT in bismuth thin films (Figure 13). Although there are numerous measurements of SIT transition, there are many different types of behaviour observed, and so far there is no single theory that explains all of the experimental results. Hence, to date there is no leading theory for the SIT transition, such as the BCS theory is for the superconductivity itself. During past few decades, there has been an effort to construct proper theories for SIT, and here we go through the main three proposed mechanisms for SIT transition: the fermionic scenario, the bosonic scenario and the pseudo-spin mechanism. [45], [57], [58]

Most theories describing SIT are applicable in the 2D limit, where thickness of the film is smaller than coherence length. Unfortunately, thin films studied in this project can be regarded to be mostly 3D - thicknesses were over 20 nm and the coherence length of nitrides is of the order of few nanometers. This may limit the applicability of some of the theories to samples studied in this thesis, but as the thinnest films are in the vicinity of 2D limit these theories should still be quite useful. In 2D, the superconducting transition begins with the superconducting order parameter becoming finite at T_c, followed by the Berezinskii-Kosterlitz-Thouless (BKT) transition establishing a global phase-coherent phase at $T_{BKT} < T_c$. However often T_{BKT} does not deviate much from T_c, and because we are presumably dealing with 3D films, we do not consider this effect here. [60]

.

3.3.1 Bosonic scenario

Dirty boson model was one of the first models that was developed to explain SIT. It describes bosons in lattice sites with a disorder potential and was developed by Fisher et al. in 1989 [61]. The theory is partially based on previous models by Efetov [62] and Gold [63] describing granular superconductors and Bose-Einstein condensation of a bosonic gas, respectively. The dirty boson model describes interacting bosons in a random potential, and in this model Cooper pairs survive the increase of disorder, but are localized. In the dirty boson model superconducting state consists of localized vortices and a Cooper pair condensate, while the insulating state consists of condensed vortices and localized Cooper pairs [48]. Hence, the superconducting order parameter stays finite throughout the transition.

The dirty boson model is based on the Hubbard model in the presence of disorder. The Hamiltonian is of the form

$$H = H_0 + H_1, \tag{47}$$

where

$$H_0 = \frac{U}{2}\sum_{\mathbf{r}} \hat{n}_{\mathbf{r}}^2 - \sum_{\mathbf{r}} (\mu + v_{\mathbf{r}} - zt)\hat{n}_{\mathbf{r}} \tag{48}$$

$$H_1 = -t \sum_{\langle \mathbf{r},\mathbf{r}' \rangle} (\hat{\Phi}_{\mathbf{r}}^{\dagger}\hat{\Phi}_{\mathbf{r}'} + \hat{\Phi}_{\mathbf{r}}\hat{\Phi}_{\mathbf{r}'}^{\dagger}). \tag{49}$$

In H_0 U is the on-site repulsion, μ is the chemical potential, z the number of nearest neighbors. The random on-site potential is described by term $v_{\mathbf{r}}$. The second term H_1 is the hopping term between lattice sites, where t is the hopping strength and $\hat{n}_{\mathbf{r}} = \hat{\Phi}_{\mathbf{r}}^{\dagger}\hat{\Phi}_{\mathbf{r}}$ is the bosonic number operator on site $\mathbf{r}$. The last summation is over pairs of nearest neighbors, so that each pair is counted only once. This model predicts that the transition is direct, and thereby a metallic ground state is only present as a singularity in the quantum critical point. Interestingly, the transition point should be universal and happen when the sheet resistance is $R_{\square} = h/4e^2 \approx 6{,}453\,\mathrm{k}\Omega$. SIT has been reported to occur near this point for example in Bi, Pb and InO, but for some other materials suchs as TiN this was found not to be the case. Although this model is not able to explain very well experimental findings in homogeneously disordered superconductors, there is experimental evidence that not only in InOx but also in TiN thin films the superconductor–insulator transition is driven by this Cooper-pair localization [64], [65].

3.3.2 Fermionic scenario

The fermionic scenario of the SIT transition was first introduced by Finkel'stein around 30 years ago [66], [67]. In the fermionic scenario, the effective attractive interaction between electrons gradually vanishes, and thus Cooper pairs are no longer formed. This is followed by the Anderson localization arising in the normal fermionic system, and thus the superconducting ground state is replaced by an insulating one. With the renormalization group approach, Finkel'stein derived an equation for the suppression of superconductivity by disorder [66]:

$$\frac{T_c}{T_{c0}} = \mathrm{e}^{-\frac{1}{\gamma}} \left[\left(1 + \frac{\sqrt{r/2}}{\gamma - r/4} \right) / \left(1 - \frac{\sqrt{r/2}}{\gamma - r/4} \right) \right]^{1/\sqrt{2r}}, \tag{50}$$

where the parameters γ and r are defined as

$$\gamma = \frac{1}{\ln\left(\frac{k_B T_{c0} \tau}{2\pi\hbar}\right)}, \quad r = \frac{e^2}{2\pi\hbar} R_\square, \tag{51}$$

where $R_\square$ is the sheet resistance in the normal state, τ the mean free time, and T_{c0} the superconducting critical temperature for the bulk superconductor. In this model, the suppression of superconductivity comes from the interplay between Coulomb and spin density interactions when there is impurity scattering present [66]. In the fermionic scenario, superconductivity does not vanish at an universal value of $R_\square$, and this is what is often experimentally observed. [57]

3.3.3 Pseudo-spin scenario

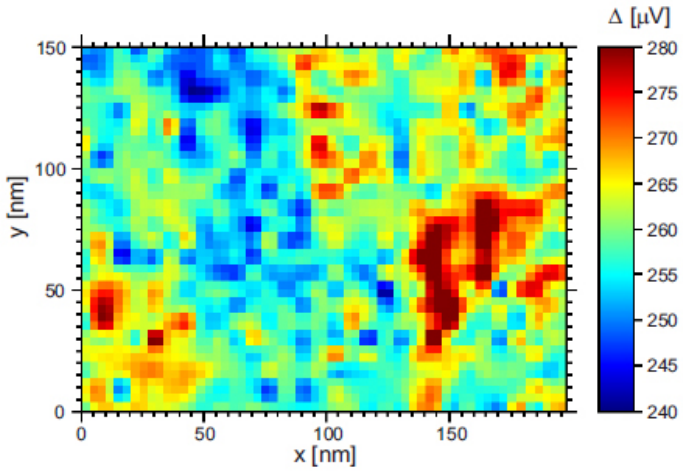

Figure 14. Scanning tunneling microscope (STM) measurements of the inhomogenities of the superconducting gap in TiN. The order parameter varies spatially in the scale of a few tens of nanometers. Figure from Ref. [68], reprinted with permission. ©2008 American Physical Society.

The pseudo spin scenario was proposed quite recently by Feigel'man et al. [69], and it describes SIT due to the competition between Cooper pairing and Cooper pair localization. In this scenario, electrons in the vicinity of the mobility edge form localized Cooper pairs that are strongly coupled. These pairs have a large binding energy, and this produces single electron gap in the insulating state. Superconductivity in this system is due Cooper pair tunneling between sites. The Hamiltonian of the model is [69]

$$H = \sum_{i\sigma} \epsilon_i c^\dagger_{i\sigma} c_{i\sigma} - \frac{\lambda}{\nu_0} \sum_{ij} M_{ij} c^\dagger_{i\uparrow} c^\dagger_{i\downarrow} c_{j\downarrow} c_{j\uparrow}, \tag{52}$$

where ν_0 is the density of states, λ is the Cooper coupling constant, and M_{ij} is given by

$$M_{ij} = \int d\vec{r} \psi_i^2(\vec{r}) \psi_j^2(\vec{r}), \tag{53}$$

where $\psi_i(\vec{r})$,$\psi_j(\vec{r})$ are single-electron eigenstates. The Hamiltonian in Eq. (52) includes hopping of pairs that is required for the global superconducting order to form. One should notice that this scenario does not take into account of the

Coulomb repulsion, but that the transition arises from random energy of the each pair. While the pseudo-spin scenario shares similarities with the bosonic scenario, in this model for example spatial distribution of the superconducting order parameter is extremely inhomogeneous, which has been observed to be the case for example in TiN [68](Figure 14). Also a giant negative magnetoresistance peak observed in TiN [70] is predicted by the pseudo-spin scenario. However weak insulating behavior observed in NbSi and other materials is not explained by this scenario [48]. One interesting feature of this model is that it predicts the temperature dependence of conductivity to be different from the variable range hopping described in section 3.2.2, with conductance predicted to behave as [69]

$$\sigma(T) = \sigma_0 \mathrm{e}^{-T/(T\ln(T_0/T))}, \qquad T_0 = \frac{c}{3}\Delta_p \approx 0.25\Delta_p, \tag{54}$$

where Δ_p is the pairing energy and c is a numerical constant. Difference between the pseudo-spin model and the standard variable range hopping is that in this scenario, low-energy states are exponentially rare.

4 Helium ion beam induced damage in nitrides

An ion beam focused on a crystalline material is known to create disorder. In order to estimate the interaction of helium ion beam with matter, we use here the SRIM software to simulate the ion beam damage to the target. This is a vast topic, and we do not dig too far into details here. The main aim in this section is to estimate size and depth profile of damaged area and amount of possible milling, and to justify the assumption that changes in material properties are mainly due to increased disorder. In addition, the width of the damaged track was estimated from the experiments.

4.1 SRIM simulations

The Stopping and Range of Ions in Matter (SRIM) is a widely used group of computer programs that model interaction of ions with matter. SRIM was developed by James F. Ziegler and Jochen P. Biersack already in 1980s, and the latest release is from year 2013 [71]. Simulations are based on the binary collision approximation, a type of Monte Carlo simulation method. SRIM is widely used in many applications involving ion beams, such as ion implantation, ion stopping and range as well as sputtering calculations, to name a few. In the simulations of this thesis, software version SRIM-2008 was used.

In this SRIM simulations, the substrate was chosen to be magnesium oxide, as it was mainly used in this thesis, and for the simulations its density was defined to be $3{,}58\,\mathrm{g/cm^3}$ which is the value reported in Ref. [72, p.108]. Niobium nitride composition was presumed to be stoichiometric for the SRIM simulations, and its density was set to a literature value $8{,}4\,\mathrm{g/cm^3}$ [73].

Based on previous measurements on elemental composition, TiN films are often rich in nitrogen [74], nevertheless for the SRIM simulations, stoichiometric TiN was chosen and should be sufficiently accurate. Densities of the pulsed laser deposition (PLD) grown TiN thin films have not been determined, and because the composition is approximated to be stoichiometric, for simulations the literature value of $5{,}43\,\mathrm{g/cm^3}$ [75, p.50-52] was used.

As this was the first time NbTiN has been deposited at NSC (or anywhere else) with PLD, the exact composition of PLD grown NbTiN film is unkonwn. For the SRIM simulation, the NbTiN composition was estimated to be $Nb_4Ti_1N_5$ so that

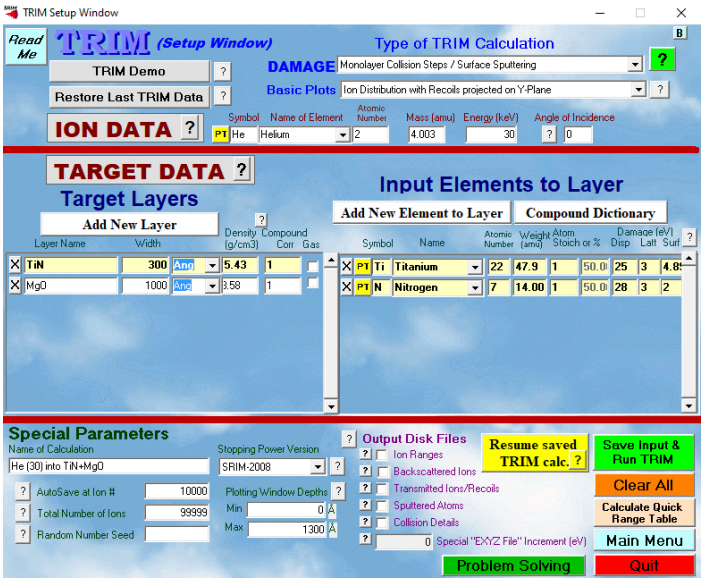

Figure 15. Screenshot of the SRIM software user interface with usual settings used in the simulation.

(Nb+Ti)/N ratio is one. The estimation of the Nb/Ti ratio is based on the fact that in the alloy target there is roughly four times more Nb than Ti and that in PLD there is nearly stoichiometric transfer from the target to the film. In the literature, density of $7{,}6\,\mathrm{g/cm^3}$ has been reported for NbTiN [76]. This value is quite close what would be expected from linear interpolation between TiN and NbN adjusted by the Nb/Ti ratio, and thus there is some confidence to use this density value for the SRIM simulations.

SRIM simulations were performed using "Detailed Calculation with full Damage Cascades" type of calculation, with 250 nm thick film and "Monolayer Collision Steps/ Surface Sputtering" type of TRIM calculation for thinner films, as this gives accurate data for thin films [71]. The incoming helium ion beam energy was set to 30 keV, as this was the beam energy used in HIM irradiation (Figure 15). The elements were added to the nitride and the substrate layer one by one without using the "Compound dictionary" and adjusting stoichiometry. Thus there was no chemical bonding included. However, deviations caused by the bonding contributions are below 2% for NbN [71], and thus the effect of bonding is presumably negligible for all of the studied nitrides. SRIM also assumes that the material is fully amorphous, and does not account for dynamical composition changes. Thus

deviation from actual damage, especially at high ion beam fluences, might be expected. However, these simulations should be sufficiently close to the reality, at least to estimate qualitatively for example the damaged area width.

4.2 SRIM simulation results

To get an idea how the helium ion beam interaction differs between the different nitrides, the first SRIM simulations for all of the nitrides were performed with layer thickness of 250 nm. For each simulation, a total of 10000 incoming ions were simulated to get reasonably good statistics for the current purpose. Depending on the layer thickness and the real time plotting options, this took some tens of minutes of computing time. Simulation results are shown in the Figure 16, with each of the plots containing roughly 500 individual simulated ions.

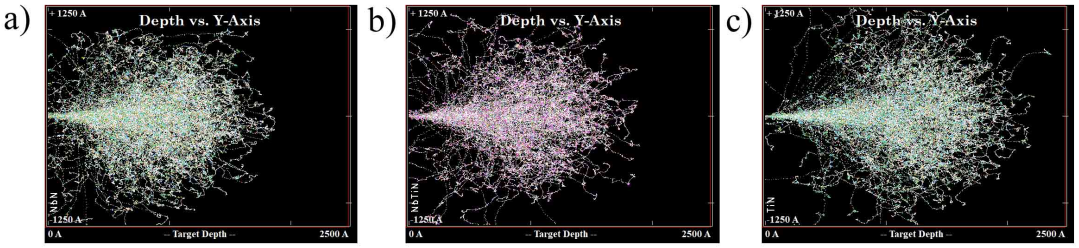

Figure 16. SRIM simulations of 30 keV helium ions impinging to a) NbN b) NbTiN and c) TiN. Simulations reveal that the helium ion range is increased and damaged area radius decreased when the target atoms are lighter.

As can be seen from Figure 16, the interaction of a helium beam differs slightly between the studied nitrides. Niobium is a heavier element than titanium, hence longitudinal range of helium atoms is smaller in NbN than in TiN. With heavier elements also the damaged area is wider, and thus TiN would be the best material for He irradiation. However, NbTiN seems to be a good compromise, because it has good superconducting properties similar to NbN, but added titanium enhances both the electrical properties and the behaviour under helium ion beam irradiation. When helium ion ranges are plotted as a function of the target depth (Figure 17), one can see that most of the helium ions are stopped only after hundred nanometers. Thus, when thin enough films are irradiated, there should be very

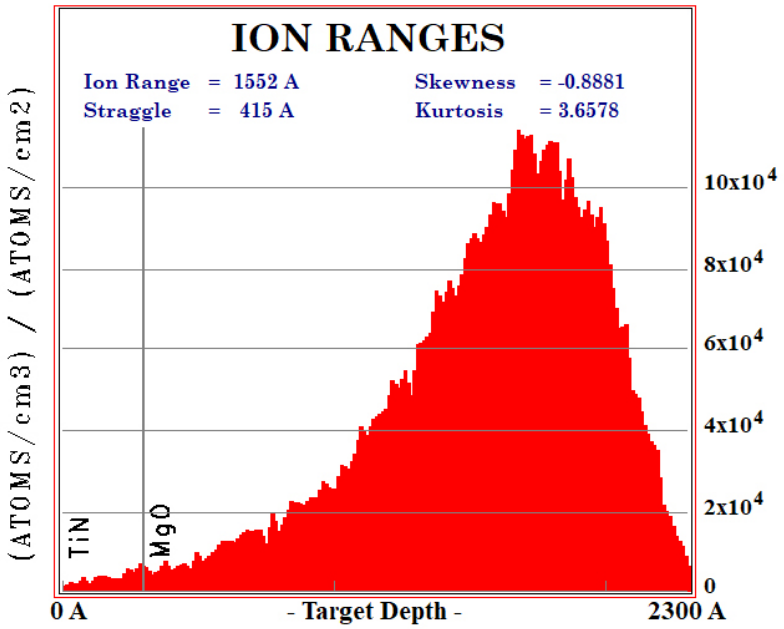

Figure 17. SRIM simulation of 30 nm TiN on top of 200 nm MgO substrate irradiated with 30 keV helium ions. Most of the helium ions are clearly trapped in substrate rather than in TiN film.

small amount of helium ions implanted inside the thin film. From this we can conclude that the implanted helium ions should not contribute to the thin film properties.

Another problem is how the substrate behaves after a large amount of helium ions is implanted inside the substrate lattice. This can cause helium ions to form bubbles inside the substrate, and ultimately to burst and destroy the substrate at the irradiated area. This problem is known in the literature to be problematic at least for a silicon substrate, and this was confirmed during this project also (Figure 18). However when MgO was used as a substrate in this thesis, it was observed that there seemed to be little to no effect due to helium ion implantation. This is not previously reported in literature: actually, there are some contrary results reported in Ref. [77]. Because MgO seemed to work well as a substrate, we did not perform dedicated experiments on this topic.

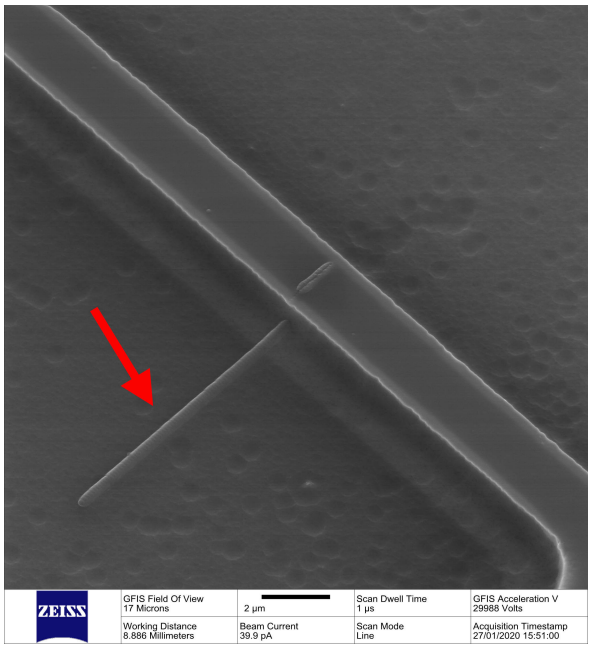

Figure 18. Helium ion gas bubbles formed inside a silicon substrate during high fluence helium ion irradiation with HIM (red arrow). In the figure, there is 100 nm thick NbTiN wire deposited on 50 nm thick SiN layer. During electron beam lithography, pattern was overetched so that the SiN was removed and etch continued rather deep to also underneath Si substrate. Hence there is an exposed bare silicon substrate outside the NbTiN wire.

In addition to thick film simulations, also thinner films were simulated. From Figure 16 can be seen that in order to get a reasonably small laterally damaged area, the film thickness needs to be reduced down to few tens of nanometers. This is a trade-off, as the superconducting properties are typically weakened when the film thickness is reduced. This is probably due to an increased disorder, so that in thinner films disorder in the unirradiated film is already higher - this could also be an advantage because then smaller fluences are required.

Because the film thickness was difficult to control in PLD growth, target thickness of thin films was set to be roughly 30 nm. This thickness is relatively easy to fabricate with PLD and RIE thinning by plasma etching. In order to determine the lateral size of the damaged area as well as its depth profile, a 30 nm thick NbTiN thin film on top of 5 nm MgO substrate was simulated with SRIM. As before, the energy of incoming helium ions was set to 30 keV and the material parameters

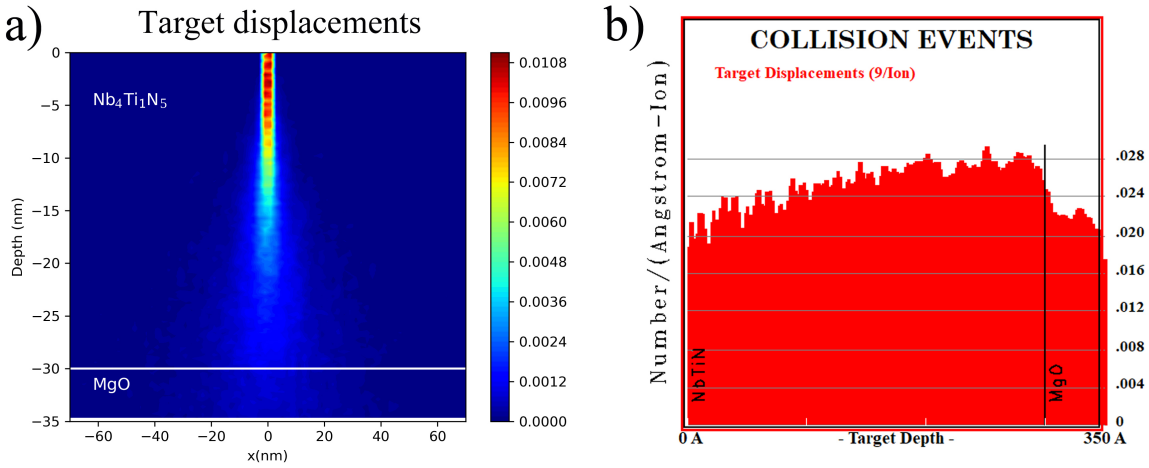

Figure 19. SRIM simulations of 30 keV helium ions impinging a 30 nm thick NbTiN thin film, with 5 nm MgO substrate layer included in the simulation. The target material dislocations are plotted in a) 2D and b) dislocation/ion as a function of depth.

were unchanged. Now 10^5 ions were simulated in order to get better statistics. The simulation results are shown in Figure 19. In Figure 19 a) data is exported from SRIM and post-processed with python to get contour plots, while Figure 19 b) is taken directly from the SRIM software.

From Figure 19a) can be seen that damaged area is 2-3 nm in during the first 10-15 nanometers, and then starts to get wider. If the thin film is 30 nm thick, at the substrate interface the damaged area is already tens of nanometers wide. Because of the PLD growth mechanisms and the imperfect lattice match with MgO, the nitride thin film in the vicinity of substrate is presumed to be more disordered, and this effect could compensate the smaller ion beam induced damage in the area. If the film is in the insulating state in the wide damaged area near the substrate, a thin junction can be formed in the upper part of the thin film. However, to get more uniform junctions, thinner films would be better, and in the future this should be taken into account.

To get idea of the milling, sputtering yields were extracted from the simulations. Most informative is to look at TiN and NbN sputtering, as NbTiN is a composite of these two. The sputtering yields of both NbN and TiN were quite similar, and both niobium and titanium sputtering was around 0.016 atom/ion. Nitrogen sputtering

was stronger than Nb or Ti, and in NbN, nitrogen was sputtered more easily than in TiN. In NbN, the nitrogen sputtering yield was 0.04 atom/ion while in TiN it was 0.03 atom/ion.

From the experiments, sputtering or milling was not found to be serious issue, but the higher nitrogen sputtering yield may cause changes to the film composition. Because this issue was difficult to estimate or quantify with measurements, the possible nitrogen deficiencies were not considered by any means. When total sputtering of NbN is estimated using simulated yield, a fluence of $\sim 3 \cdot 10^{17}$ ion/cm^2 is needed to sputter 30 nm thick film.

4.3 Helium ion beam damage: experiments

To estimate what kind of damage there is in reality, nitride samples were irradiated with different doses to see what level of sputtering and what was expected width of the irradiated line with each HIM spot size setting. Sputtering yield of nitrides was found to be quite low, and HIM images alongside transport measurements revealed that for $\sim$30 nm films fluence of $1 \cdot 10^{19}$ ion/cm^2 is not enough to mill film completely through. There is roughly two order of magnitude difference between this observation and simulations, and this is mainly explained by finite size of the He beam. Precise estimation of the ion beam milling rate was not performed, because this was not crucial for the project.

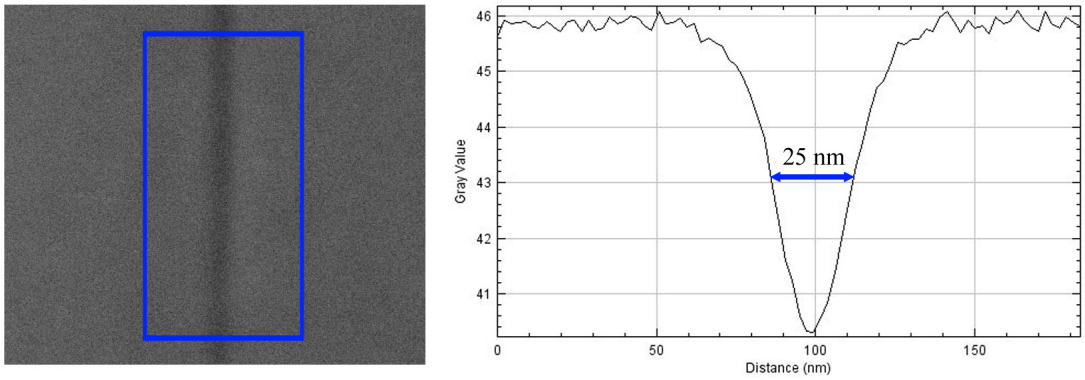

Figure 20. Estimation of damaged area size from a HIM image. On the left there is a HIM image of the irradiated line, where darker area is carbon deposition during HIM irradiation. On the right there is a profile of the image gray values averaged over the blue rectangle area. Irradiation was done with HIM spot size 2, and in this case FWHM width of the carbon deposit is 25 nm.

Estimation of HIM irradiation linewidth was done by estimating the damaged area width from HIM images with ImageJ software (Figure 20). In Table 1 expected linewidth for each spot size is presented. Although the actual damage to the film is not visible at low fluences, a estimation was still possible from the carbon deposit. This is possible because the helium ion beam charges the film during irradiation, and carbon impurities deposit on the irradiated area. This carbon deposit is visible in HIM images and can be used to estimate the damaged area size. However, this is an indirect measurement of the damaged area size, and one should be very careful when using values obtained with this estimation. Nevertheless, it seems that the linewidth estimation obtained with this method agrees reasonably well when compared to milling tests and later with the transport measurements, and thus we are using the Table 1 values in calculations for now on.

Table 1. HIM linewidth estimations based on the observed widths of carbon deposits.

Spot size in HIM	Expected linewidth
7	6±4 nm
6	7±5 nm
4	9±5 nm
2	20±10 nm
0	150±100 nm

Although the linewidth is determined from an indirect method, most inaccuracies in these values are from a different origin than the linewidth estimation method itself. This is because the focus, the stigmation and the current of the ion beam itself varies a lot from day to day. The quality of the obtained ion beam parameters depends on the operator capabilities to fine tune the ion beam, the performance of instrument itself varies only slightly. Additionally, there is sometimes thermal drift of the sample stage that is affecting the damaged area width especially during long exposures. This issue can be mostly overcome when the sample stage is placed to the HIM chamber day before the actual irradiation.

5 Fabrication

Because the main focus of this project was to study the disorder in superconducting nitrides induced by an helium ion beam, and the fabrication of Josephson junctions exploiting this feature, the other fabrication steps were kept as simple as possible. First, high quality nitride (TiN, NbN, NbTiN) thin film was deposited with the infrared pulsed laser deposition (PLD) technique [74]. After film deposition, electron beam lithography (EBL) with negative resist AR-N 7520.17 *new* followed by reactive ion etching (RIE) in fluorine plasma was used to define a wire and a measurement pads on the film. The superconducting wire was then irradiated with 30 keV helium ions to create a thin disordered line that can serve as a weak link in a Josephson junction. Figure 21 shows the fabrication steps used here, and in the following we will go through those in more detail. Because electron beam lithography is a well established and widely used technique, we will especially concentrate on the pulsed laser deposition and helium ion irradiation steps.

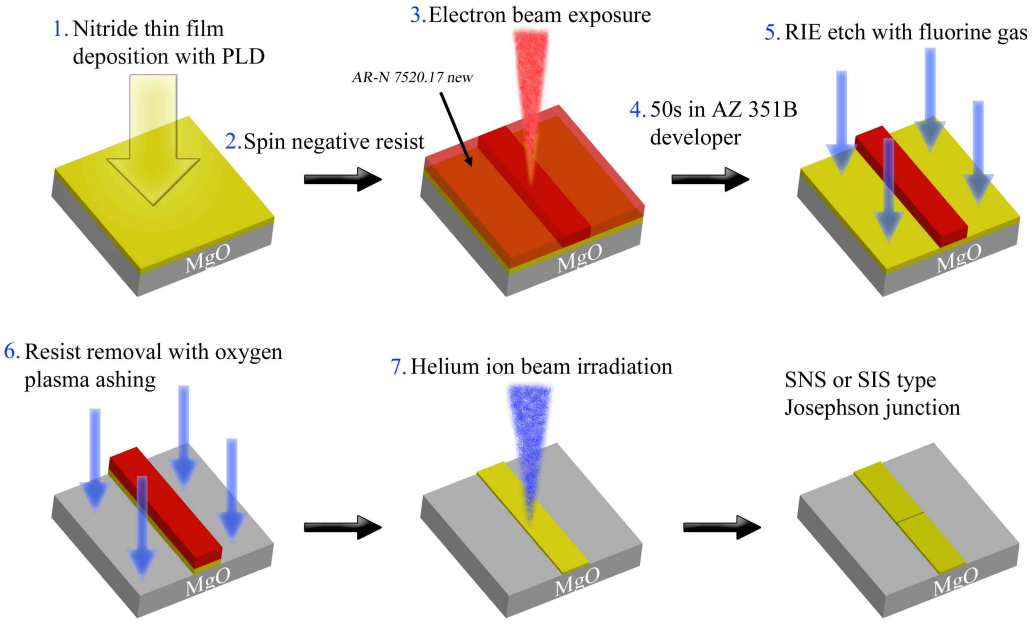

Figure 21. Fabrication steps for making Josephson junctions with direct writing.

5.1 Pulsed laser deposition

Pulsed laser deposition(PLD) is a straight-forward and versatile physical vapour deposition technique for thin film deposition. It is conceptually simple and allows deposition of high quality thin films from large variety of materials. PLD has gained growing interest in thin film deposition during last decades, because of a few benefits over other similar methods: PLD is fast, clean and cost-effective way to produce high quality thin films with complex stoichiometry. Nowadays PLD is used to deposit thin films from insulating, ceramic, metallic, or polymer materials. [78]

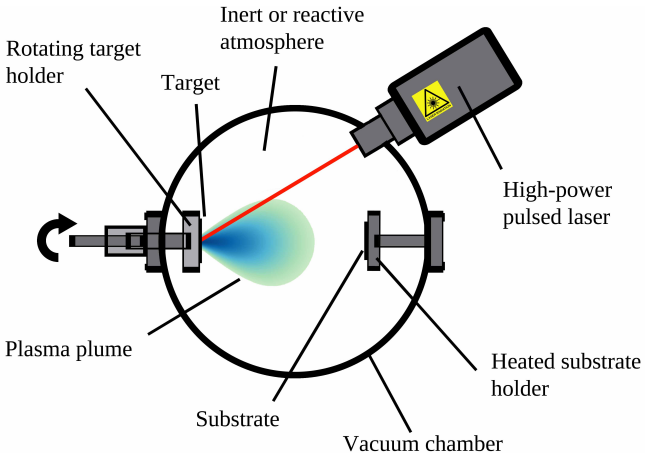

Figure 22. Simplified schematic of a typical pulsed laser deposition setup.

In PLD, a high intensity pulsed laser beam is used to ablate a target material inside vacuum chamber (Figure 22). With high enough intensity, this process results in a plasma plume that expands out of the target material surface. This plasma plume is usually highly forward-peaked and has a high forward velocity. After the ablation process, the plasma plume expands, and possibly slows down in gaseous atmosphere. When the plasma plume finally reaches the substrate, ablated atoms are condensed on the substrate resulting in a film growth. This process can be repeated using desired number of pulses to reach a target thickness of the film.[79]

The physics involved in laser ablation is surprisingly complex, mainly because of the extremely short timescales and high energies involved in the process. The laser beam photons interact primarily with the valence and the conduc-

tion band electronic states. In metals, photons are absorbed through the inverse bremsstrahlung or the photoionization process, the former being dominant process with long wavelength infrared photons [80]. The absorbed energy is relaxed through electron-electron, electron-phonon and phonon-phonon interactions. Because in metals and semiconductors the energy relaxation time is of the order of $10^{-12} - 10^{-11}$ s, with nanosecond pulses, the ablation can be regarded as a thermal process [81].

The pulsed laser deposition system in the Nanoscience Center has been made in-house over a decade ago. This system has been mainly used for deposition of superconducting nitrides, namely TiN[74], NbN [82] and TaN [83]. Because of some limitations of the system, during this project some upgrades and enhancements to the setup were made by the author with the aid of lab engineers. These modifications are discussed briefly in the following.

5.1.1 Development of PLD system at Nanoscience Center

The PLD setup has an Ekspla NL301 HT Nd:YAG laser operating at its fundamental wavelength 1064 nm, with a 10 Hz pulse frequency and a 4 ns pulse duration resulting in $\sim$6 J/cm^2 fluence on the target. The PLD vacuum system consists of turbomolecular pump (Cit Alcatel Annecy 5400) and a scroll pump (Edwards XDS 10) for rough pumping and to serve as the backing pump for the turbo pump.

Previously, the optical system in the setup had a design flaw, as the focal point of reflections from the focusing lens was inside the laser itself. This could possible lead to a situation where laser rod could be damaged by reflection from the

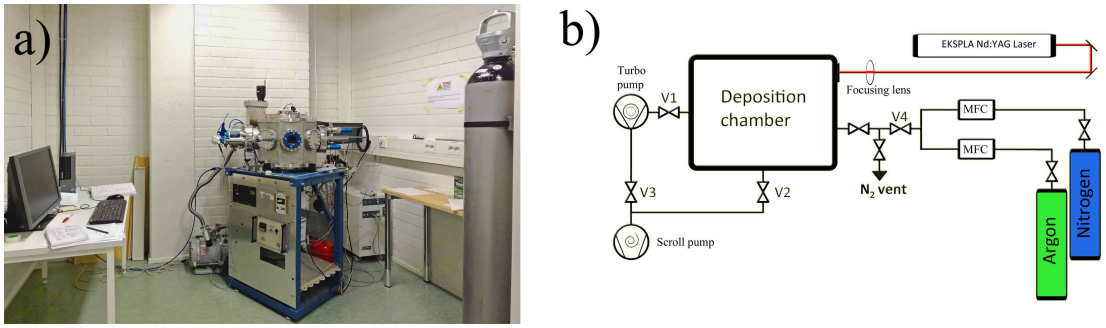

Figure 23. a) Image of the PLD setup and b) PLD setup schematic after upgrades.

focusing lens. Another problem in the old setup was the inefficient target material usage and prominent splashing of micron sized target material droplets on to the film during deposition. To tackle these issues, optical beam path was increased and the lens was mounted on a motorized stage controlling lateral position of the lens, so that focal point could be adjusted laterally. These modifications are discussed in more detail later on.

Before the modifications, the setup was operated completely manually. With the modifications, the lens motor needed to be controlled, a decision was made to enable a computer control over gas the flow and the laser, in order to get more reproducible deposition conditions and to improve usability of the system. Old electronics were completely removed and replaced by a new ones, so that very few things were left to manual control.

The computer control of the PLD system was implemented with Arduino Uno microcontroller, that controls two mass flow controllers (MFC:s) and the stepper motor driver. The microcontroller sends information and receives commands via the serial port of the PC. This communication is handled by graphical user interface (GUI) sofware written by the author, and thus the software is able to control the PLD electronics. The software also communicates with the Ekspla NL301 laser, enabling remote control of the laser.

5.1.2 Optics system upgrades

Previously, the deposition was done by selecting a lateral position of focal point on the target by manually adjustable lens mount, and then using motor to rotate the target stage. This method made a deep circular groove to the target, and even though the deposition rate was good, splashing of micron sized particles was a serious problem. Additionally, the laser focal point adjustment was previously done by adjusting lens mount screws, and then firing laser to the target to see where the focal point had shifted. In order to overcome these issues, a simple lens position sweep using motorized stage was built.

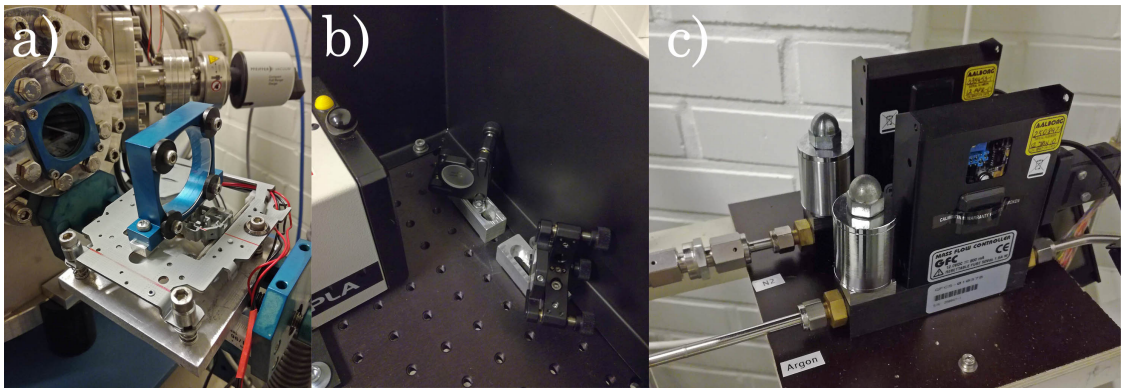

Figure 24. a) The new optical stage made from a DVD drive, b) the new optical beam path using two IR mirrors mounted on an optical table and c) the installed mass flow controllers.

There was no need for a high precision motorized stage, so the decision was made to use a cost-effective and simple approach: the motorized stage was built from an old DVD drive stepper motor mechanism (See Figure 24 a)). A DVD drive was taken apart and then a new wiring was set up for the bipolar stepper motor. The whole motor drive was placed on custom made aluminium plate, and the lens was mounted on top of the drive using an aluminium block. Motorized stage was mounted to bottom aluminium plate by bolts and springs, so that the stage is floating on top of the springs such that the height could be adjusted with adjustment screws. The whole setup is on top of manually operated linear drive, so that now there is a complete xyz position control of the lens. Because the target is rotating, often only the motorized lateral x-axis needs to be adjusted after the first laser alignment. This means that the laser can be operated fully remotely.

To obtain more efficient target usage and to reduce splashing, the possibility to use the lens position sweep was added to control software. This allows to scan the focal point during deposition, so that instead of creating deep circular groove, the laser creates a shallower and wider ring on the target. This reduces splashing of micron sized particles significantly (Figure 25), but also seems to enhance plasma plume production stability and decrease thickness variations in PLD grown film.

Another upgrade to the optics system was to increase the laser beam path. This was done by reversing the laser direction and guiding the laser beam to the PLD chamber using two laser mirrors (ThorLabs NB1-K14). Previously, the whole

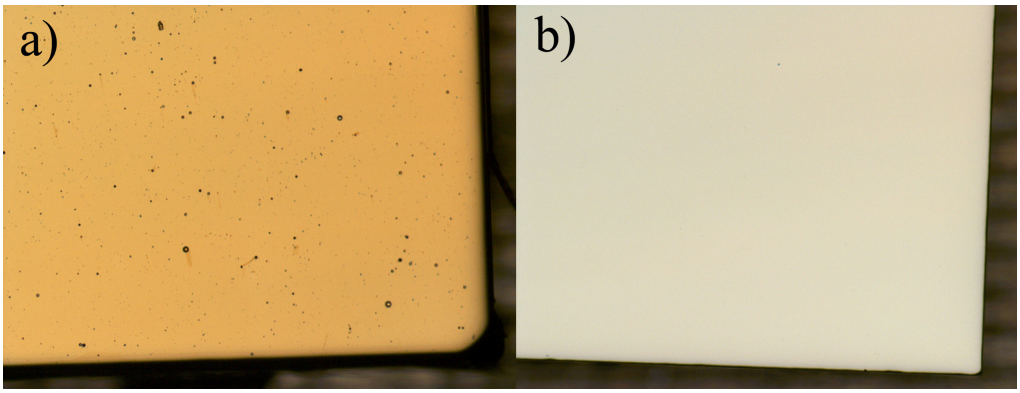

Figure 25. a) TiN film deposited with PLD without optics sweep and b) NbN film deposited with PLD with optics sweep. Decrease in splashed particulates is dramatic. Both of the images are taken with optical microscope and 10x lens.

setup was on top of a aluminium plate, but now it was replaced by a ThorLabs optical table. The two mirrors and the Ekspla NL301 laser unit was now mounted on an optical table as shown in the Figure 24 b). The mirrors were mounted on the table using a standard mirror mount and a custom made aluminium piece for the height adjustment. These changes were done to mainly protect the laser, but also in order to allow greater flexibility for possible future modifications of the setup.

5.1.3 PLD electronics: design and implementation

The PLD electronics were designed to be cost-effective and not overly complicated. The main microcontroller was chosen to be Arduino Uno, because of prior experience on using the controller and it's affordable price. The microcontroller was connected to a computer via USB cable, and communication between the PC and the microcontroller was implemented via the standard serial interface. The microcontroller was set up to control both the mass flow controllers and to read their sensor data, to read data from the newly installed thermometer (DS18B20 temperature sensor) located on the vacuum chamber outer surface and to control lens motor. Part of the circuit diagram of the new PLD electronics is in the Figure 26, where electrical connections to the microcontroller is shown. Electronics of the system were designed and implemented by the author.

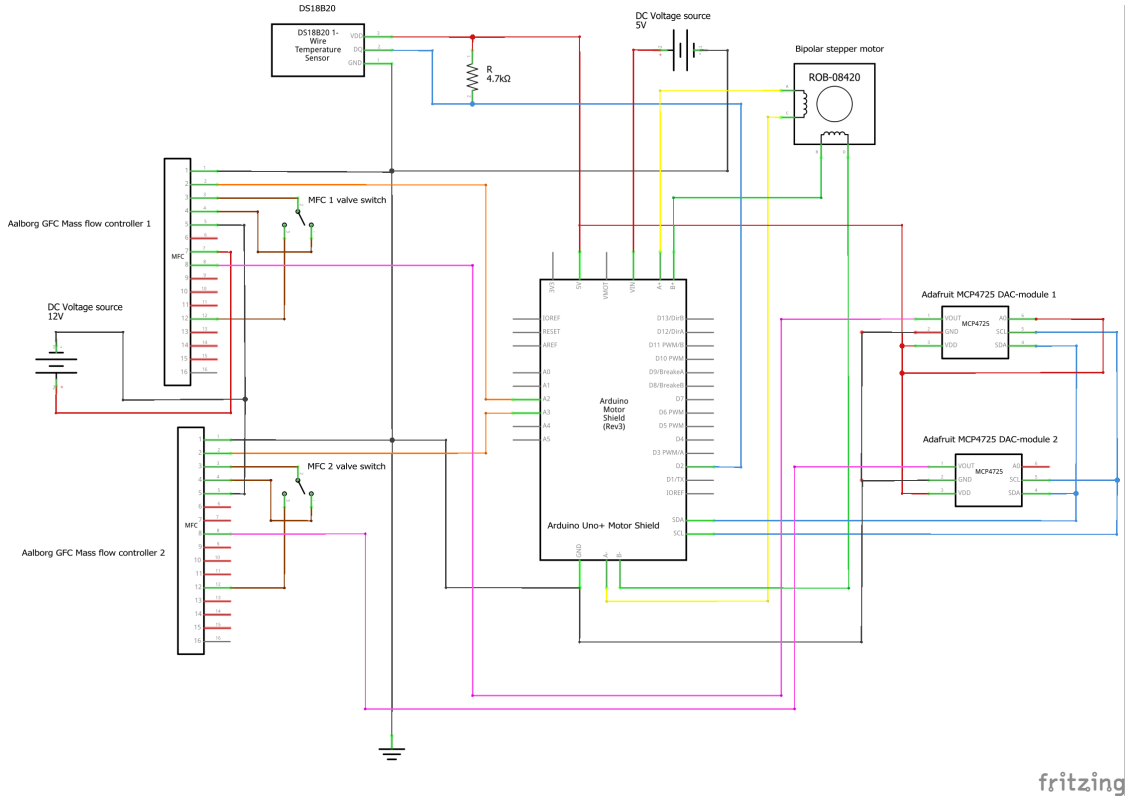

Figure 26. The PLD electroncs circuit diagram, showing wiring of the Arduino Uno microcontroller. Circuit diagram was made with open-source software Fritzing.

Previously, there was already one mass flow controller in the setup controlling N_2 flow, now another similar one was added for a new argon line. The mass flow controller is model GFC17 made by Aalborg. The microcontroller is controlling the flow of the two MFC:s by changing voltage in the 0-5 DC setpoint input terminal at the MFC. This voltage adjustment is achieved by using two Adafruit MCP4725 12-bit digital-analog converter (DAC) modules. The voltage outputs of these modules are controlled by the same SDA and SCL lines of the microcontroller (Figure 26). The MFC:s have also valve open and close switches, that were separated from the microcontroller system to a) get better reliability for these crucial functions and b) because these are used often when the PLD vacuum system is operated.

The Arduino Uno microcontroller was progammed using native Arduino integrated development environment (IDE), and the language used was the default one based on C/C++ languages. The program is available in the author's Git re-

pository as a file named pld_control_arduino.ino. Communication to and from the PC is via serial interface with baud rate of 9600, but because the Arduino incoming message handling is varying and somewhat of a bottleneck, the microcontroller processes commands only every 2 seconds. Every outgoing message from the microcontroller contains all sensor values and current state of the system. Hence, the system status is refreshed only every two seconds, but this was a necessary modification to ensure stability of messaging. It has not been any issue so far, but could be improved in the future.

5.1.4 PLD software

The PLD control software consists of two separate programs: one GUI software on the PC end that sends to and receives commands from the Arduino microcontroller, and program on the microcontroller itself. The PLD control software, surprisingly named as *PLDcontrol*, was designed and implemented by the author. It was written using C# programming language and open-source Windows Forms GUI class library in Visual Studio IDE. This choice was based on the author's prior experience working with these tools. Initially python was also considered, but because the control software needed to be relatively complex, C# was selected over python. Because the operating system of controlling computer is Windows, C# provided also native and easy access to the serial ports and the webcam interfaces. Performance of C# is also much better than with Python, and the compiled executable can be run in most Windows systems without any other installations, which is big advantage. *PLDcontrol* consists of few thousand lines of code and it is maintained in the authors Git repository [84]. This thesis is not about software development, so we won't go through all the details on how the control software for the PLD is constructed. However, to document the main functionalities, we will go through here the main features of the software. Screenshot of the software is shown in Figure 27.

In *PLDcontrol*, there is the possibility to adjust the gas flow setpoint on both of the MFC, and setpoints are communicated to Arduino microcontroller. Microcontroller reads and sends the flow values, and they are shown in the GUI. From the PC one can also control the lens position and movement, and those commands are send to Arduino only when something is changed. Thus, for example the lens motor is sweeps until an incoming message from the PC says otherwise. All

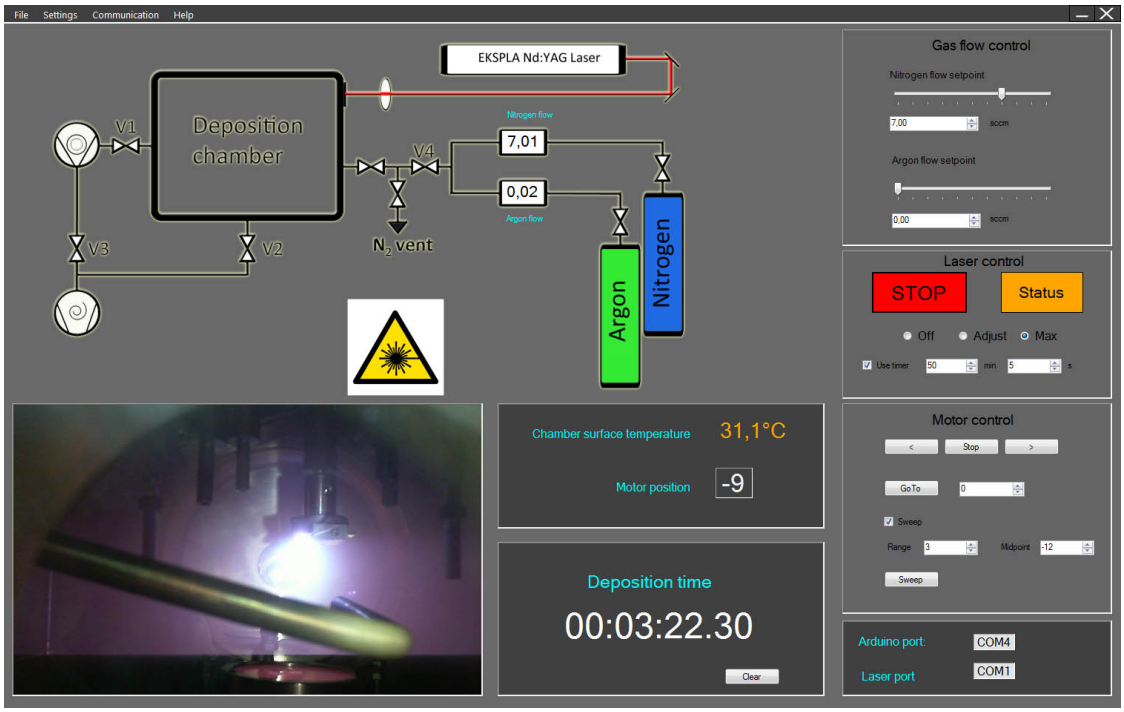

Figure 27. Screenshot of the PLDcontrol software during PLD deposition. All main functionalities of the PLD can be controlled via this software. Screenshot is taken during real deposition, and in the lower left corner one can see webcam view of Ti plasma plume.

commands going to and from the PC are logged to help debugging, and a logfile is accessible via the GUI. Used commands can be checked from the source code [84].

One of the main advantages of this upgrade was ability to control laser programmatically via an RS232 interface. The PC user can now start and stop the laser, and most importantly, one can set a timer on how long laser will be on. Previously, this was done by timing laser pulses with stopwatch, it is obvious how the computer control enhances the reproducibility and the safety of the deposition. Now the laser error messages are also sent to the computer, and from the logfile one can see when errors have occurred. Because now the laser status can be requested from the PC, one can more easily monitor the laser operation and solve possible issues faster when they emerge.

The last feature of PLD software is the ability to see a live webcam view of the deposition chamber. This improves safety, because now there is no need to look at the chamber directly so often. Although laser goggles are always used, the laser is

extremely powerful and one shouldn't look in the chamber too often. The ability to see a webcam view from the GUI software means that also possible problems could be detected earlier. One future improvement could be to install camera with better dynamical range, as huge brightness of the plasma plume saturates image over large area and the precise focal point cannot be determined from the webcam view.

5.1.5 Evaluation of the modifications

Modifications to the PLD system were implemented successfully, and the usage of the system is now easier than before. The main modifications influencing the actual quality of the deposited films were the introduction of the laser sweep, and the ability to use also argon gas during deposition. Former was proved to be very successful, and splashing of micron-sized particles was reduced significantly (Figure 25). Films grown with the laser sweep were almost free from target material particles, which was not the case without a sweep.

The new argon gas line enables more control over deposition pressure during reactive deposition with nitrogen, with the novelty that also a non-reactive deposition can be performed at a controlled pressure atmosphere rather than in high vacuum. This modification should open many new possibilities for the deposition, and elemental superconductors (e.g. Al, Nb, V), metals (Pt, AlMn) as well as HTS superconductors such as MgB_2 and YBCO could be possibly deposited with the system in the future. Another point is that vacuum system performs poorly at low flow rates, because a low pressure causes issues with backflow from the rough pump. Now it is possible to do deposition with low nitrogen flow and adjust pressure to more optimal range with argon gas (30 mTorr and above seems to be good, as roughing base pressure $\sim$ 9 mTorr).

The now mass flow controlller setpoint is now given by the computer, and thus the gas flow rates should be more reproducible. Previously, the setpoint was set by adjusting a potentiometer until the measured gas flow value was what was wanted. Although this approach was working, fluctuations in the measured value when the setpoint was set introduced an error and decreased reproducibility. When the setpoint value is set from the software, this is easier and much more reproducible.

Controlling the laser via the RS232 port with the PC enables a more detailed

status check of the laser, and more importantly, adds the ability to use a timer in depositions. When one can set the deposition time via the PC software, the deposition time is far more accurate than with the old method (handheld stopwatch) and safety of the deposition is increased.

An additional improvement made during this project was that the silver glue used to glue substrates to the sample holder was changed to a water soluble NO-VOC Silver Paint by SPI supplies. This made glueing easier compared to the previous fast curing glue, and possibly reduced level of volatile organic compounds released to the vacuum chamber. The water vapour level in the chamber could be slightly increased by this, but most of the water is evaporated during the glue curing, which is done outside the vacuum chamber. Possible changes in the impurity level could be investigated at the JYFL accelerator laboratory with time-of-flight elastic recoil detection analysis (TOF-ERDA) that gives precise elemental composition.

Overall, it is safe to say that modifications of the setup were successful and proved to be really useful in practice. Further developments of the system could include a loadlock chamber, laser heating of the substrate to get even higher temperatures and a more stable linear stage for the laser optics.

5.1.6 Thin film deposition with PLD

Thin film deposition with the PLD is quite a long process. In order to obtain high-quality films, the vacuum chamber needs to be baked overnight to get good base pressure. First, substrates (amorphous 50 nm thick SiN or cubic (100) oriented MgO (Crystec GmbH)) were glued to the substrate holder with the conductive silver glue. This glueing is an important step, as there should be no bubbles in order to get a good thermal contact to the substrate holder. Glue was cured by heating the substrate holder to $110\,^{\circ}\mathrm{C}$, and maintaining this temperature for 10 minutes before the substrate holder was inserted into the vacuum chamber. Vacuum chamber was first pumped with a rough pump to ~ 15 mTorr pressure, and then the turbo pump was used to pump the chamber to the base pressure. During the pumping, the substrate holder was slowly ($5\,^{\circ}\mathrm{C/min}$) heated to $700\,^{\circ}\mathrm{C}$, and chamber was pumped overnight in order to reach better base pressure. When the substrate heater was at $700\,^{\circ}\mathrm{C}$ and the chamber was pumped overnight, the chamber wall temperature reached to $\sim 40\,^{\circ}\mathrm{C}$ and base pressure was $\sim 2 \cdot 10^{-7}$ Torr.

This procedure was found to be a key factor when high quality superconducting films are deposited [74].

After the chamber baking, the target was conditioned by firing the laser to it for approximately ten minutes, in order to expose new fresh target surface. Targets used in this thesis were Ti target (99.999% purity from Goodfellow Inc.), Nb target (99.95% purity, Matsurf Technologies Inc.) and $Nb_{0.75}Ti_{0.25}$ alloy target (99.95% purity, Matsurf Technologies Inc.). Substrates were protected by a shutter at this stage. This was also good time to tune the sweeping of the optics for the actual deposition, and a slightly larger area was sweeped to make sure that there is a clean surface in the actual deposition. Contaminants released during this process were pumped away, and this pumping was enhanced by raising the substrate temperature to $770\,^{\circ}\mathrm{C}$. Temperature was held at this temperature for 10 minutes, after which the substrate temperature was lowered back down to the deposition temperature. The deposition temperature used with the nitrides was usually $700\,^{\circ}\mathrm{C}$ as higher temperatures should yield better quality films. Some tests with temperatures up to $750\,^{\circ}\mathrm{C}$ were performed, but results did not differ significantly from the lower temperature depositions.

Table 2. PLD parameters, which gave the highest quality superconducting nitride thin films during this project, with corresponding sample characteristics. Resistivity is determined at the lowest temperature where the film is still in the normal state.

Material	TiN	NbTiN	NbN
Deposition temperature	$700\,^{\circ}\mathrm{C}$	$700\,^{\circ}\mathrm{C}$	$700\,^{\circ}\mathrm{C}$
Argon flow	0 sccm	2.00 sccm	0.82 sccm
Nitrogen flow	7.00 sccm	3.00 sccm	1.02 sccm
Pressure	92 mTorr	66 mTorr	36 mTorr
T_c	4.4 K	15.3 K	15.7 K
Resistivity	$14\,\mu\Omega\,\mathrm{cm}$	$78\,\mu\Omega\,\mathrm{cm}$	$150\,\mu\Omega\,\mathrm{cm}$

After these PLD preparation steps, the turbo pump was swithed off, it was slowed with nitrogen flow and gate valve V1 (Figure 23 b)) was closed. The chamber was filled with pure nitrogen to 50 mTorr, and argon (99.99999% purity) and

nitrogen (99.99999% purity) flow rates were set from the GUI for the deposition. Then valve V2 (Figure 23 b)) was opened and the pressure was let to settle. After this, the actual deposition was started: the deposition time was set in the GUI and the laser was started. The usual deposition parameters for each film are shown in Table 2. The growth rate varied, but was around 10 Å/min for all of the nitrides. Critical temperatures reported in Table 2 are the ones obtained with modified setup.

When the deposition was over, the substrate heater was kept at $700\,^{\circ}\mathrm{C}$ at least for 30 minutes in order to anneal the films. After this, the substrate heater was slowly ramping temperature down to room temperature (this takes $\sim$ 4 hours), and the pumps were turned off. The chamber was not opened until next day, to ensure that the films were cooled properly before exposing them to the room air.

5.2 Electron beam lithography

A pattern was defined to the PLD deposited nitride film with electron beam lithography and reactive ion etching. Here, negative resist AR-N 7520.17 *new* was used, because this resist has excellent resistance against plasma etching, also when a negative resist is used, less electron beam exposure time is needed for design used in this thesis. With fluorine based reactive ion etching (RIE) recipes, the etching speed of AR-N resist was approximately 2-3 times lower than that of the standard electron beam lithography resist PMMA, while the electron beam dose used here to expose the resist was approximately half of what would be needed for PMMA.

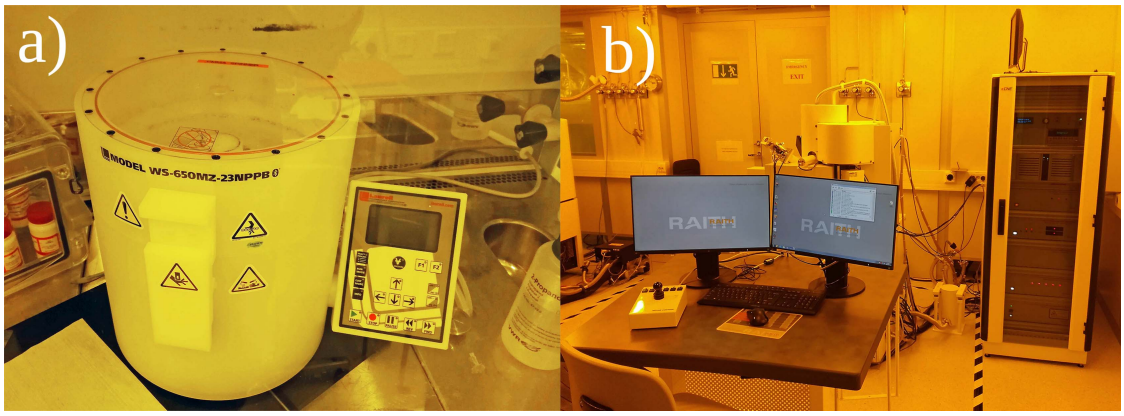

Figure 28. a) Laurell Technologies spinner b) Raith E-Line scanning electron microscope, both located at the NSC cleanroom.

After the PLD deposition, the sample was cleaned in isopropyl alcohol (IPA) bath using the Finnsonic ultrasonic cleaner, to get rid off the silver glue residues and other contaminants. Then, AR-N 7520.17 *new* resist was spinned on top of the sample using the Laurell Technologies spin coater model WS-650MZ-23NPPB (Figure 28a)). The spinning time was 60 seconds, while the spinning speed was 4000 rpm. After spinning, the resist was soft baked at $85\,^{\circ}\mathrm{C}$ for 1 minute. The resulting resist layer thickness was approximately 400 nm.

When the resist was spinned on the sample, Raith E-Line scanning electron microscope (Figure 28b)) was used to expose the resist to define the pattern. In addition to the Raith electron microscope, also the older LEO 1430 scanning electron microscope was used in the early stages of the project. Electron beam lithography with LEO electron microscope was similar as with the Raith microscope, and thus it is not discussed here in detail.

Exposure of the pattern with Raith microscope was done in two separate steps: first superconducting line and pad lines with small features (Figure 29, green pattern) were exposed with lower current, and then pads and rest of the pattern (Figure 29, blue pattern)) were exposed with larger current. Acceleration voltage was 20 kV in all of the exposures.

For the superconducting wire structure, $1000\,\mu\mathrm{m}$ writefield was used, so that the whole structure could be exposed within one writefield. For this structure, high resolution was needed, so the standard $30\,\mu\mathrm{m}$ aperture was used. This aperture yields roughly 0.33 nA current. The dose used for the finer structure was usually

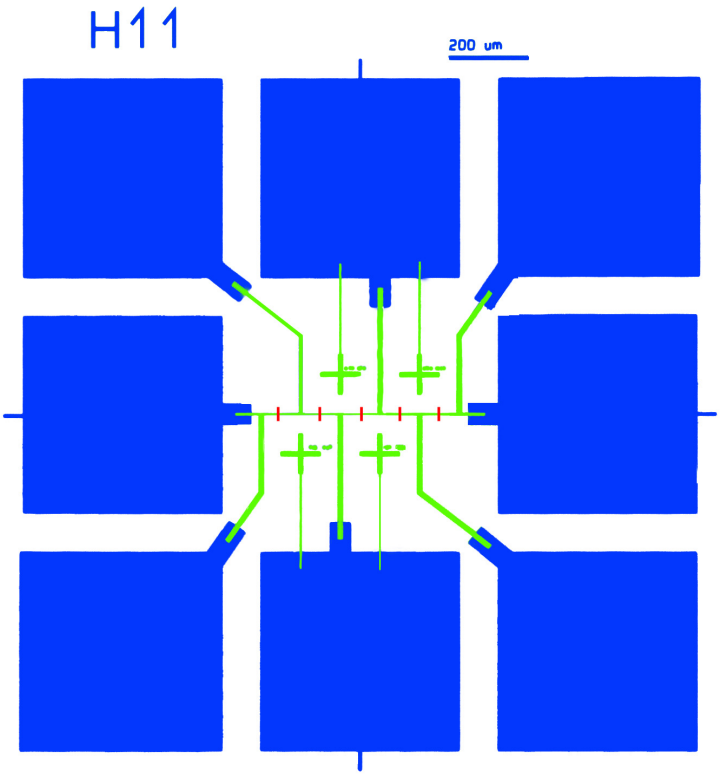

Figure 29. Used pattern geometry. The green pattern is made with smaller current and using single writefield, the blue pattern is made with larger current. Overlap between patterns is to ensure that no gaps are formed if stitching is not perfect. Red lines denote helium ion irradiation to fabricate Josephson junctions to the horizontal line defining the superconducting wire.

$110\,\mu C/cm^2$, and a step size of 200 nm was used most of the time. With these parameters, the first exposure took roughly 5 minutes.

The larger structure was too large to expose in one writefield, so the exposure of the pattern needed to be constructed from multiple different writefields. In order to do this so called stitching, the writefield needed to be aligned. This writefield alignment was done to a small feature on the corner of the sample. In order to get better stitching, $500\,\mu m$ writefield was used for this structure. To get high current and thus reasonably small exposure time, the $120\,\mu m$ aperture and high current mode was used. With these settings beam current was roughly 10.5 nA. Sometimes stitching of the writefields were somewhat off, and there were some gaps or kinks on the pads. However this was a minor inconvenience, because the

actual superconducting wire was done using single writefield.

The resist was developed using an undiluted AZ 351B developer, with a 50 s development time, and the development was stopped by rinsing sample with deionized water. The whole negative resist recipe was developed by the author, and it is proven to be simple and able to produce reasonably good aspect ratios and small feature sizes, but there is probably some room for optimization.

5.3 Reactive ion etching

After the resist development, the exposed nitride thin film was removed with reactive ion etching (RIE). In reactive ion etching chemically reactive plasma, in this case formed from fluorine based compounds, is used to etch thin films. In RIE there is both physical and chemical etching present, and the ratio of these two can be tuned by adjusting the electric field strength and the gas pressure. The RIE equipment used in this project was Oxford Plasmalab 80+ RIE (Figure 30).

Figure 30. Picture of the Oxford Plasmalab 80+ RIE located at NSC cleanroom. The RIE vacuum chamber is seen on the left, and the one on the right is the chemical vapour deposition (CVD) chamber.

RIE etching was done by using CHF_3 gas for NbN, and SF_6 for the TiN and NbTiN thin films. This choice was made because nitrides containing titanium seemed to be etched considerably faster with SF_6 gas. Both recipes had a small oxygen flow in addition to main etching gas. The etching rates were $\sim$20 nm/min for the CHF_3 etching of NbN, and $\sim$15 nm/min for SF_6 etching of both TiN and NbTiN films. These rates were not measured precisely, because etching was stopped effectively to MgO substrate and thus there was no need to determine etching rate very precisely. Also these recipes have not been optimized for nitrides, and some effort for the etching recipe development could be done in the future.

However, edges of the wires were reasonably straight, so these recipes are already performing quite well. RIE recipes used in this thesis are in the Table 3.

Before the actual etching process, an soft oxygen clean (same recipe as standard O_2 clean, but with 60 W RF power) was performed with the RIE to get rid of the excess resist residue and the possible other contaminants. Then, the actual dry etching recipe was run for usually 10 minutes to ensure that films were etched completely through. After this, the resist was removed using standard oxygen clean in RIE for 4 minutes.

Table 3. RIE recipes used in this project

Recipe	NbN etch	TiN, NbTiN etch	Standard O_2 clean
CHF_3 flow	50 sccm	0	0
SF_6 flow	0	100 sccm	0
O_2 flow	5 sccm	5 sccm	50 sccm
Pressure	55 mTorr	70 mTorr	40 mTorr
RF power	100 W	60 W	200 W
Etching rate	$\sim$ 20 nm/min	$\sim$ 15 nm/min	-

After the RIE etching and resist removal, the film thickness was measured with the KLA Tencor P-15 profilometer. This was done because there was still some variation from the estimated thickness even though while PLD thickness control was improved significantly. If the profilometer measurement showed that film was too thick, the sample was RIE etched to the target 30 nm thickness. Because the profilometer had quite high errors when small thickness was measured, the films were not thinned much below 30 nm.

5.4 Helium ion microscopy

5.4.1 Introduction to helium ion microscopes

As the diffraction limit of light microscopes and UV lithography was reached, a quest for more precise imaging technology began in 1940s. To overcome the issue with diffraction, particles were used to create the image. The most obvious choice of the particle is electron, because they are easy to produce with simple electron guns, and the wavelength of electron is already ∼10 picometer with a 30 kV acceleration voltage.

However in some cases, a focused beam of ions is an attractive alternative for electrons. Because of the considerably bigger mass of an ion, the effective wavelength of an ion is significantly shorter than for an electron. Thus, the ion beam size can be decreased to even smaller what is possible with electrons. The quest for an ion beam microscope began with development of liquid metal ion sources: however these ion beams couldn't provide small enough beam sizes, and sample contamination and high sputtering rate was a problem in imaging. Nowadays, gallium ion beams are used for precision milling, but for high precision imaging and pattering a better technology needed to be developed. This was achieved after significant advances in ion source technology that lead to the modified gas field ion source (GFIS) that uses helium as the source gas. The first working HIM prototype was invented in 2005 by ALIS Corporation, and very soon ALIS was purchased by Carl Zeiss AG. Zeiss started to manufacture helium ion microscopes for commercial use in 2007, and has been the only commercial manufacturer of HIM:s ever since. [14], [85]

The basic working principle of GFIS is similar to the Field Ion Microscope (FIM) developed in the 1950s by Erwin Müller. In the helium ion microscope, gas atoms are ionized in the strong electric field near a sharp tip, and the formed ions are subsequently accelerated with an electric field. The ion source emitter tip is made from crystalline wire that is chemically etched to form the initial sharp tip. Inside HIM, this tip is then cooled to cryogenic temperatures (∼85 K) and the so called build process (proprietary of Zeiss) is used to create a pyramid of atoms on parabolic initial tip [85]. Finally, small number of atoms on the very end of this pyramid shape are responsible for >90% of the emission. Usually three atoms in a triangle arrangement ("trimer") is used, as this is most stable. [85]

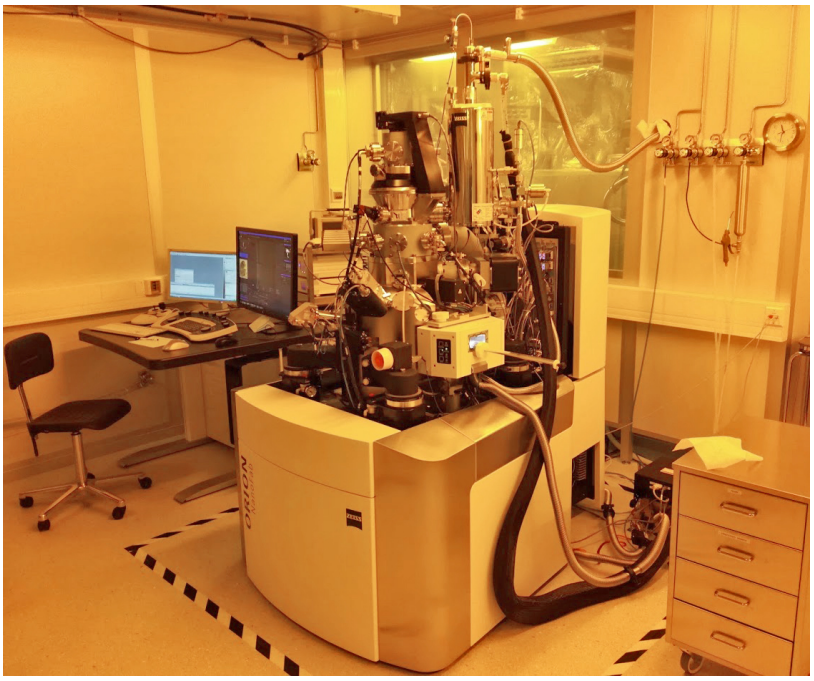

Figure 31. Helium ion microscope at the Nanoscience Center cleanroom.

Accelerated ions are focused and aligned with an ion optical system that consists of solely electrostatic lenses and deflectors. Finally, the focused ions hit to the sample, and the imaging signal is formed from secondary electrons produced in the sample. These secondary electrons are detected by an Everhart-Thornley detector that is the only detector in standard HIM setup. This was true also for the NSC setup (Figure 31) until January 2020, when a new detector for secondary ion mass spectrometry (SIMS) was installed. With this detector, the HIM at NSC is now capable for material analysis with extremely high spatial resolution, although this possibility was not used during this project yet.

Helium (or neon) ions are used in HIM because of the high ionization potential of these noble gases. When electric field is engineered to be strong enough to ionize helium atoms only in the very end of the tip, most of the impurity atoms are ionized earlier, and the contribution of impurity atoms in ion beam is negligibly small.

An advantage of HIM over the usual SEM is the higher resolution due to the smaller beam size and interaction volume. Also, for SEM imaging samples need to be conductive, but with HIM, imaging of insulators is possible, because the

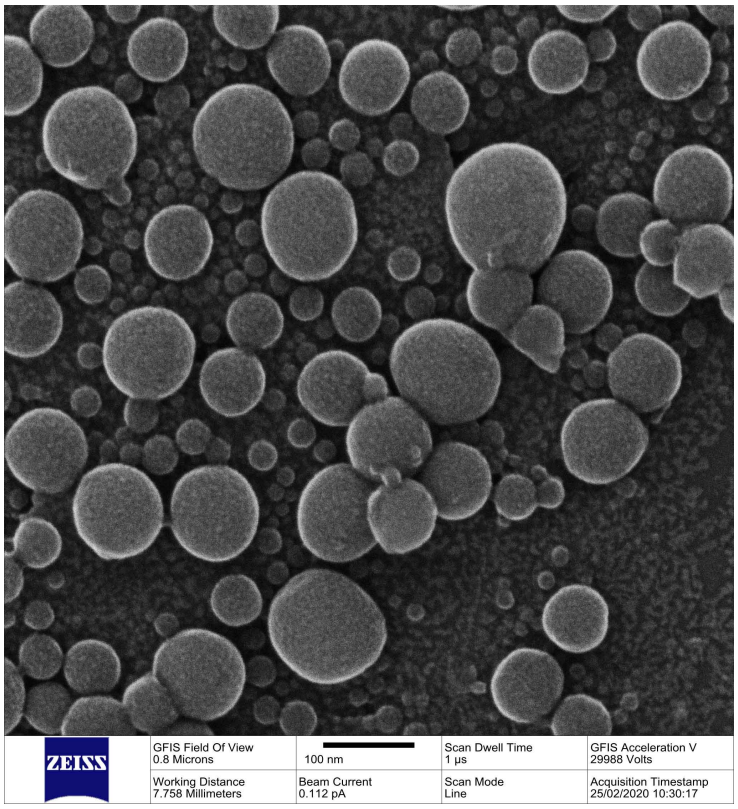

Figure 32. A helium ion microscope image of tin nanoparticles on carbon using spot size 7. This sample was used as a reference, when helium ion beam was aligned and tuned.

accumulation of positive ions can be compensated with electron gun. Additionally, HIM offers high surface sensitivity and new possibilities for material analysis.

5.4.2 Helium ion irradiation

When the pattern (Figure 29) made with e-beam lithography was ready, the next and last step in the Josephson junction fabrication was to irradiate superconducting wire. Usually, before the irradiation a pristine superconducting wire was measured at low temperatures, so that the superconducting critical temperature and current-voltage characteristics could be determined. After the measurements, the wire was cleaned with ultrasonication in IPA bath, after which the possible remaining residues were cleaned with a soft O_2 clean in RIE.

When the sample was ensured to be clean, it was mounted on the HIM sample stage with clamps. In order to be able to do the stigmation and focus adjustments

also on the sample, a small amount of ink from a marker pen was put to a corner of the sample. The ink contains ~ 100 nm sized nanoparticles and it is good for microscope adjustment purposes. A reference sample containing tin nanoparticles (Figure 32) on carbon was also placed on the sample stage, and an image of the stage was downloaded to HIM software (Zen) so that one can easily navigate between the different samples. Then, the sample was inserted in the vacuum chamber via the loadlock and the beam was turned on.

In helium ion microscope, beam tuning is far more important and time-consuming task than in standard SEM. In the beginning of each imaging session, the beam current from trimer or dimer needs to be optimized in order to find best imaging voltage (BIV). Also, a helium ion beam from only one atom needs to be selected and tuned to be in the center of the focus line. Further beam tuning involves the beam shift and tilt alignments, as well as the crossover position and the source distance adjustments. This was done all in the "source maintenance" mode and scanning field ion microscopy (SFIM) of the tip itself, after which the image was optimized against the reference sample. These optimizations include further alignments, and most importantly, the stigmation and the focus adjustment, and needs to be performed individually for each spot size. When satisfactory image quality was obtained, sample imaging and irradiation could be started.

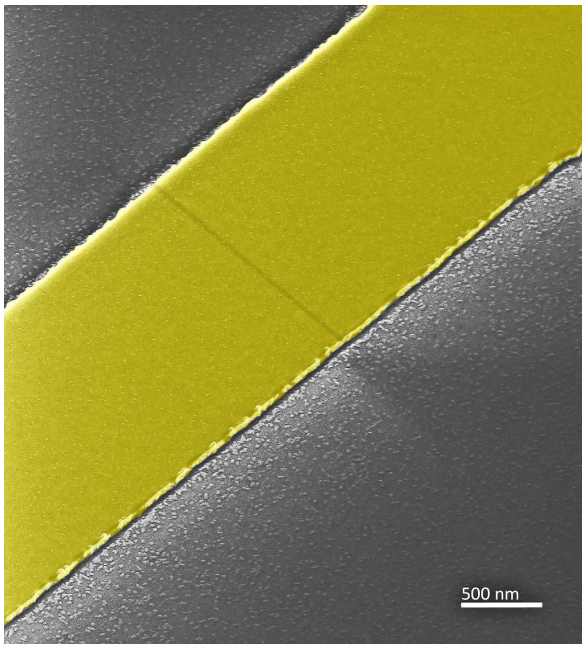

Figure 33. Coloured HIM image of ∼100 nm thick and 2 µm wide TiN line after helium ion irradiation. The darker line is irradiated area, forming a Josephson junction.

First, a correct location was searched by taking quickly images from the sample, so that the sample would not get too much irradiation during this stage. When the correct place was found, either the integrated software from Zeiss or the Raith patterning software was used to irradiate the target area. Although both software have a different working procedure, most important parameters like fluence and stepsize could be used similarly. These parameters were set up before the irradiation, and the software did all the irradiation for the wanted regions. During the first experiments, all of the junctions were irradiated in the same large writefield, but later on each junction was irradiated individually. This proved to be better way to ensure that the irradiation linewidth is as small as possible. When irradiation was finished, the ion beam was switched off and the sample removed from the vacuum chamber.

6 Measurements and results

6.1 Measurement setup

The fabricated Josephson junction samples were characterized with electrical transport measurements at low temperatures. All the measurements were performed in shielded rooms designed to shield against electromagnetic interference (Figure 34). These shielded rooms are basically Faraday cages, and they have their own isolated ground where all the measurement equipment are connected. Because NbN and NbTiN thin films have sufficiently high critical temperatures, measurements were performed only down to liquid helium temperatures (4.2 K) with the so called dipstick measurement. In this type of measurement, the sample is bonded to a sample stage that is on the bottom of the stick with electrical connections on top, and it is then slowly inserted into a liquid helium dewar. The sample stage is made from copper to ensure that the stage temperature is as uniform as possible. A Cernox temperatures sensor is attached to the stage to measure the temperature of the stage.

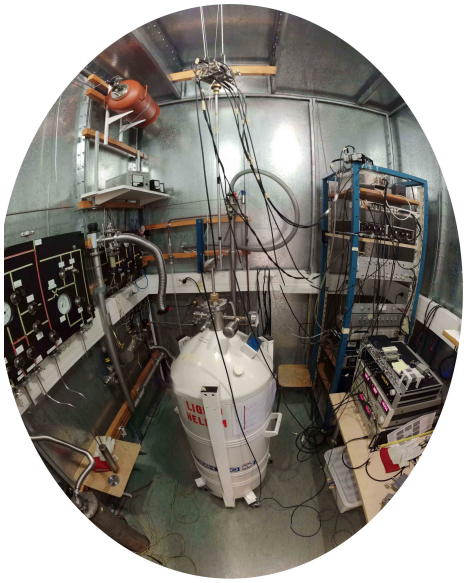

Figure 34. An ongoing dipstick measurement in the NSC shielded room 1. The measurement equipment on the right are connected to the dipstick with coaxial cables. The temperature of the sample stage is controlled by how deep the dipstick is inserted in the helium dewar.

The temperature of the experiment can be controlled by changing the insertion depth of the dipstick in the dewar. This is possible when the end of the dipstick does not touch the liquid helium but is in the helium vapour. Helium vapour has a temperature gradient from 4.2 K to almost the room temperature at the very top of the dewar. However, this temperature gradient is quite large, of the order of 1 K/cm or more, and thus an exact control of the stage temperature is quite difficult.

Figure 35. Kulicke & Soffa 4523A wedge wire bonder that was used to make electrical connections between the sample and the dipstick sample stage.

Samples were glued on the dipstick sample holder stage with GE varnish specifically designed for cryogenic heatsinking. This is to ensure that thermal contact between the sample and the stage is as good as possible, and to ensure that the sample is firmly attached to the stage. The varnish was let to dry for an hour or so, and then electrical contact from the sample to the stage was made with a Kulicke & Soffa 4523A wedge wire bonder (Figure 35). Samples were bonded to the dipstick stage using aluminium wire. The bonder operates by feeding a bonding wire through a sharp needle, and bonding is done by pressing the needle to the sample and applying an ultrasonic pulse to locally weld the bonding wire. After the first bond, the needle is just lifted so that user can select the place for the second bond. The wire is cut by an automatic tearing process after the second bond is finished. The force, ultrasonic power and time as well as other parameters of

the bonding process are controllable by the user, and are usually adjusted slightly during every session to obtain optimal bonding. Bonding was always started from the copper sample stage pad, and the other end of the aluminium wire was bonded to a pad in the sample.

6.2 Electrical measurements

To determine the superconducting critical temperature and how the resistance of the sample evolves as a function of temperature, the resistance of the sample was measured while the temperature of the dipstick stage was changed. The resistance was measured with the usual four point configuration to get rid of lead resistances. The measurement was done using an AC signal and lock-in technique to reduce noise in the measurement. The circuit diagram of the lock-in measurement is shown in Figure 36 a). An AC driving signal is taken from the sinusoidal output of the lock-in amplifier (Stanford Research Systems SR830/SR810), and this alternating current flows through the sample via a series resistor $R1$, in order to make the measurement current biased ($R1 \gg R_{sample}$). For most of the measurements, a $100\,\mathrm{k}\Omega$ series resistance was used, but for the most resistive samples a $1\,\mathrm{M}\Omega$ resistance was needed to make current stable enough. The current going through the sample was first amplified with an Ithaco model 1211 current preamplifier which converts current to a voltage signal, which was subsequently measured by the lock-in amplifier. The signal of the lock-in amplifier was sent to a computer via National Instruments ADC converter. The voltage signal was measured over the junction, and first, the differential signal was amplified with Ithaco 1201 Low Noise voltage preamplifier. Then the amplified difference signal was measured with another lock-in amplifier (SR830/SR810).

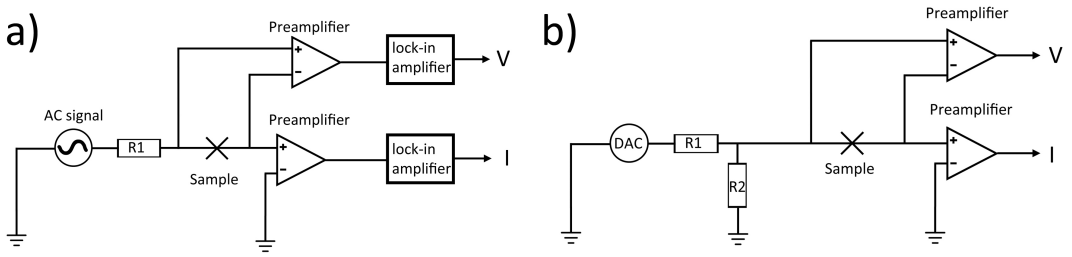

Figure 36. Schematic of a) R(T) measurement and b) IVC measurement setup. Resistances $R1$ and $R2$ were selected so that measurement in a) is current biased with a constant current and b) is voltage biased with a controlled voltage. Ratio of resistances in setup b) also determines the voltage range over the sample (voltage division).

Most of the measurements were performed with a roughly 19.2 Hz frequency and 100 mV lock in excitation voltage. Significantly lower and higher frequencies were filtered away with the integrated filters in the preamplifier (usually <3 Hz and >1 kHz were filtered away). The temperature of the sample was calculated from the calibrated Cernox temperature sensor resistance, which was measured with AVS-47 Resistance Bridge using a $30\,\mu\mathrm{V}$ excitation.

For most of the samples, also current-voltage characteristics (IVC) were determined with the measurement circuit shown in Figure 36 b). These measurements were mainly performed with a voltage bias, so that this bias voltage was sweeped with in-house built computer controllable DAC unit ("Pynskä-boksi"). The current through the sample was measured again with an Ithaco current preamplifer, and the voltage over the sample was measured with an Ithaco voltage preamplifier. DAC sweep was performed from negative voltage to positive voltage, and the DAC output range of the sweep varied from ± 1 V to ± 10 V. The voltage drop across the sample was adjusted by using a resistive voltage divider, with the resistances selected so that the sweep voltages across the sample were in a suitable scale. Often, this meant that a 1:100 voltage divider was used, and that the voltage across the sample was swept from -10 mV to 10 mV. If not otherwise stated, in all the presented current-voltage figures measurement direction is from the positive voltages to the negative, thus the measurement sweep goes from the upper right corner to the lower left corner.

In all measurements, the output signals of resistance bridge, the lock-in amp-

lifiers or the preamplifiers were converted to a digital signal using a National Instruments (NI) ADC converter, and finally, this digital signal was recorded with a measurement computer located outside the shielded room. This data logging and control was done by using dedicated LabView-programs (for R(T) measurements `Aki_dipstick_Version2.vi` and for the IVC measurements `RF Control mx with interval v3.5+pid_Geng-cryostat1.vi` was used, former is written partly by the author).

6.3 Titanium nitride thin film samples

6.3.1 Titanium nitride

Titanium nitride (TiN) is a golden yellow refractory compound, and like most other transition metal nitrides, it is a hard, ceramic material. TiN has a very high melting point ($2930\,^{\circ}\mathrm{C}$) and a NaCl-type crystal structure. Among the studied nitrides in this project, TiN has the lowest superconducting transition temperature (6 K for best bulk samples [86]) and the highest electrical conductivity [74]. Because of its high hardness, its excellent wear- and corrosion resistance and its appealing color, it is widely used in industry as a hard coating for example in tool bits [87]. TiN is considered to be a non-toxic material and has high biocompatibility, and consequently it is also used in medical devices and orthopaedic implants [88]. In microelectronics it is used as a diffusion layer [89] and as a gate electrode [90].

Because of the high electrical conductivity, its expectionally low microwave losses and reasonably high superconducting critical temperature, TiN has been used in superconducting devices such as resonators [91], quantum bits [92] and microwave kinetic inductance detectors [93], [94].

In TiN thin films, the disorder driven superconductor-insulator transition has been observed [65], [68], [70], [95], [96]. Although some early experimental data suggested that T_c suppression in TiN follows well Finkelstein's formula (Eq. (50)) and thus the fermionic scenario [95], further experiments have revealed that the situation may not be that straightforward, and another study suggests that an insulating phase in TiN has localized Cooper pairs [65]. SIT in TiN seems to be quite peculiar, and phenomena such as the giant negative magnetoresistance peak [70] and spatial inhomogeneities of superconducting gap [68] have been observed in TiN films. The same kind of behaviour has been observed in InOx thin films [97], but neither the bosonic nor the fermionic SIT model is able to explain this peculiar behaviour. However, the pseudo-spin model is able to explain these to some extent.

The temperature dependence of conductance in the insulating state does not follow the usual variable range hopping predictions, and instead some kind of hyperactivated behaviour under 100 mK temperatures has been observed [65]. This observation has been referred as the "superinsulating" state, and might be interesting in junction fabrication because the barrier resistance would change

significantly when temperature would be altered. One explanation for the superinsulating state is that it is a low-temperature charge-BKT phase, arising from the superinsulator–superconductor duality [98].

All the experiments on disorder driven superconductor-insulator transition in TiN have been conducted with ultrathin films ($d \sim 5\,\text{nm}$), and the superinsulating state was observed only at low temperatures and in the presence of magnetic fields. In this study, there were no possibility to investigate the possible SIT in TiN further, because we did not have time to perform dilution refrigerator measurements during the project. However T_c suppression in TiN thin films was demonstrated, as discussed below.

6.3.2 Tc suppression

Titanium nitride thin films have a superconducting critical temperature near liquid helium temperatures, and this was problematic for the experiments as we were not able to perform dilution refrigerator measurements. However, when $2\,\mu\text{m}$ wide superconducting wire made to sample i3L with thickness of 100 nm and a bulk film $T_c = 4.45\,\text{K}$, was irradiated with HIM using different fluences, its T_c was suppressed below liquid helium temperatures (Figure 37). T_c was suppressed also with smallest linewidth irradiation made using spot size 6 and fluence of $5 \cdot 10^{18}$ ion/cm^2. Because linewidth in the design was 2 nm and estimated real linewidth was 7 nm (Table 1), effective fluence was calculated to be $\sim 1.4 \cdot 10^{18}$ ion/cm^2. The larger linewidth used was 200 nm, and this area was irradiated using spot size 1 and stepsize of 100 nm. Irradiations were performed using the Raith software. Sheet resistances of the irradiated region with width L were calculated using estimated real linewidth L, and they were $29 \pm 3\Omega$, $34 \pm 3\Omega$ and $450 \pm 150\Omega$.

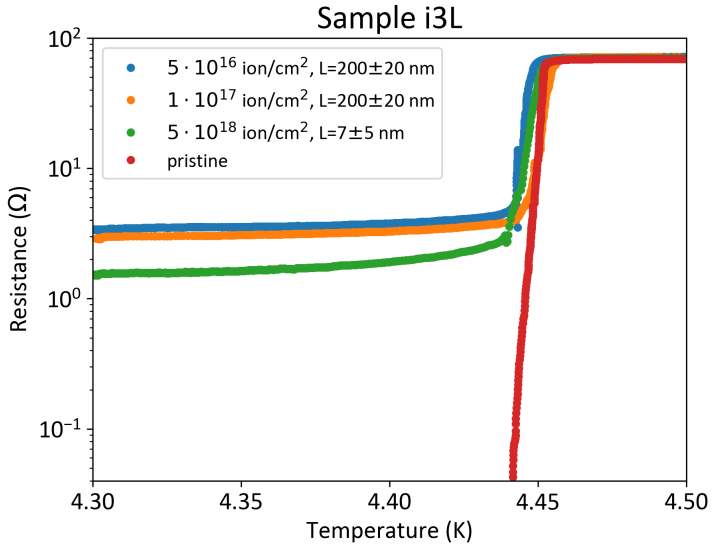

Figure 37. The resistance as a function of temperature of TiN sample i3L after helium ion irradiation. First transition originates when bulk wire becomes superconducting, and remaining resistance is contribution from irradiated region. T_c is suppressed below liquid helium temperatures also with small linewidth irradiation (green dots). Calculated sheet resistances of the irradiated region are $29 \pm 3\Omega$, $34 \pm 3\Omega$ and $450 \pm 150\Omega$ from lowest fluence to highest. Here L is the width of the irradiated region.

The current-voltage characteristics of this sample were also measured. The results of these measurements are plotted in Figure 38, where one can see that the IVC behaviour is somewhat linear and ohmic. This is because the measurement was performed so close to T_c, and thus the superconducting gap was too small to cause any nonlinearities. While T_c was too close to see superconductivity in irradiated lines, it is probable that at low enough temperatures, the smallest linewidth irradiation line should exhibit Josephson junction behaviour. The sheet resistance is high ($450\,\Omega$) but not in kΩ range, hence at low temperatures junction could show either SNS or SIS type behaviour. Although there is yet no direct proof of Josephson junctions fabricated to TiN using helium ion irradiation, it is very likely that they could be fabricated to TiN films using this method.

Interestingly, the pristine TiN wire showed a highly hysteretic IVC (Figure 39), whereas in irradiated lines this hysteresis was suppressed. This is probably caused by some heating effects, but there is no clear explanation yet for the behaviour.

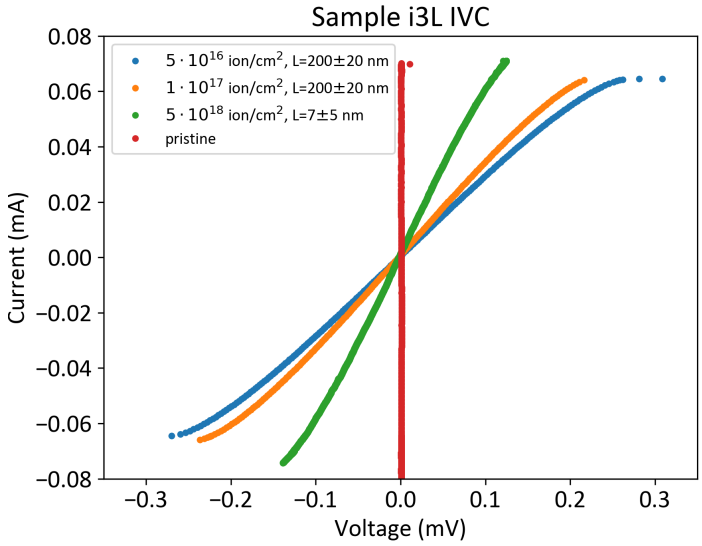

Figure 38. Current-voltage characteristics of TiN sample i3L after helium ion irradiation, measured at 4.2 K. Behaviour is almost ohmic with some nonlinear character. The jump in the IVC is because the critical current of the bulk wire is reached.

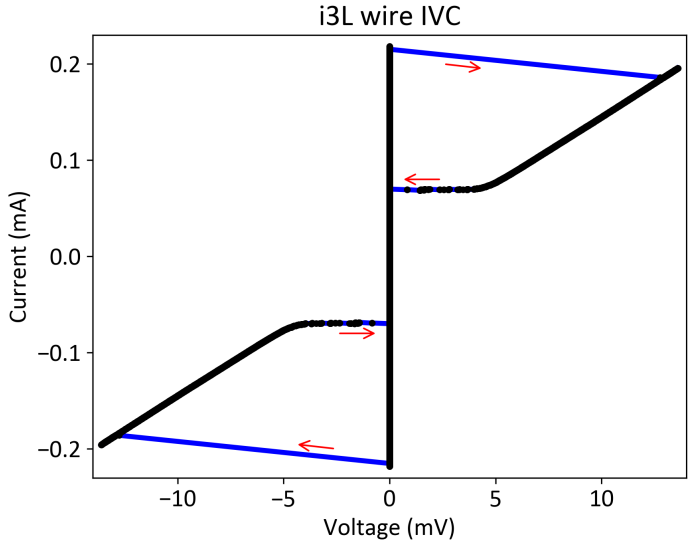

Figure 39. Current-voltage characteristics of $2\,\mu\mathrm{m}$ wide and $\sim$100 nm thick superconducting TiN wire before helium ion irradiation, measured at 4.2 K. IVC shows strong hysteresis, which is probably due to heating effects.

6.4 Niobium nitride thin film samples

6.4.1 Niobium nitride

Niobium nitride (NbN) is a type II superconductor with bulk superconducting critical temperature up to 17.3 K [99]. It is a hard, ceramic material with good chemical resistance, and hence it could be used for example in hard coatings [100], but in most of the applications requiring good mechanical wear resistance or good electrical conductivity, TiN outperforms NbN. However, relatively high T_c makes NbN appealing alternative for superconducting electronics, and this is where most of the applications are: NbN has been used for example in Josephson voltage standards [2], bolometers [101], thermometers [54], [102] and superconducting nanowire single-photon detectors (SNSPDs) [103], to name a few.

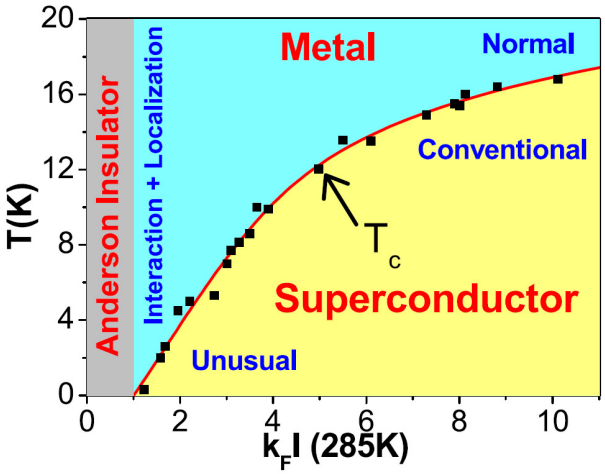

Figure 40. The phase diagram of homogeneously disordered NbN films. The quantum critical point is at $k_F l \sim 1$, and at this point at zero temperature there is direct SIT transition. Figure from [104], reprinted with permission. ©2010 Springer Nature.

Niobium nitride is known to have a disorder-driven superconductor-insulator transition [54], [105]–[108]. In [105]–[108] NbN was driven through the SIT transition by adjusting the film thickness, and thus disorder was not changed directly. These studies showed that with ultrathin films, disorder is high enough to push NbN to the insulating side, and that SIT occurs earlier than the universal value predicted by the dirty boson model [107]. However, reasonably good fits to

Finkel'stein's equation (Eq. 50) have been obtained, suggesting that the fermionic scenario is realised in NbN [106], [107]. In [54], where the author has contributed, NbN was pushed to the insulating side by adjusting the nitrogen content rather than directly the disorder, and the insulating behaviour was used for low-temperature thermometry. The resistance behaviour as a function of temperature over a large voltage range showed variable-range hopping type of behaviour (Section 3.2.2). Therefore, it seems that nitrogen content is changing the level disorder of the film and localizing electrons, thus SIT is driven by disorder also in this case.

6.4.2 Tc suppression

In the beginning, T_c suppression as a function of helium fluence was investigated in NbN thin films. This was done by irradiating relatively wide ($200\,\mathrm{nm}$-$2\,\mu\mathrm{m}$) region to the superconducting wire, and measuring its resistance as a function of temperature in order to determine T_c of the irradiated region. In these measurements, the first resistance drop is when the unirradiated leads become superconducting, and the remaining contribution is from the irradiated region.

When T_c suppression was studied, NbN samples with a thickness of ∼10-70 nm were used. Some of the NbN samples (N6/N7) were fabricated by thinning ∼200 nm NbN films deposited for another project. However, because a substantial reduction of thickness was needed, the thickness homogeneity of the resulted films was decreased compared to films deposited directly to target a thickness. This may be the origin of some of the difficulties encountered when junctions were fabricated to NbN.

NbN was the first material used in this project, and the first samples were fabricated using the older LEO electron microscope and slightly different geometry that is presented in Figure 29. Samples N73a and N73b had $4.54 \pm 0.03\,\mu\mathrm{m}$ and $4.31 \pm 0.03\,\mu\mathrm{m}$ wide superconducting wires with thicknesses of $68 \pm 3\,\mathrm{nm}$ and $57 \pm 3\,\mathrm{nm}$, respectively. Five junctions or irradiated regions were fabricated on both chips, and the resistance measurements of these samples show that T_c is suppressed when high enough fluence is used. In Figure 41, R(T) measurement from the sample N73b is presented, showing that higher fluence results in lower T_c and higher resistance. However, with NbN the T_c reduction was difficult to control, and variations in e.g. ion beam parameters and sample details caused the

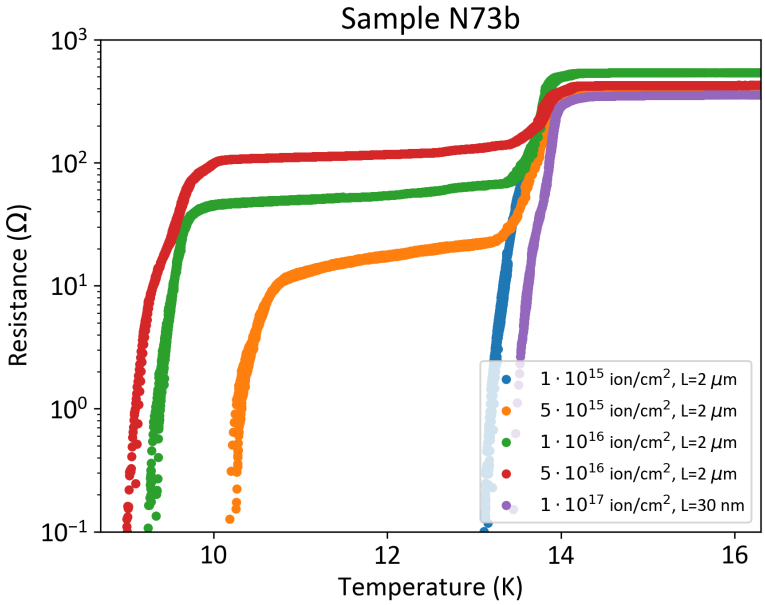

Figure 41. Resistance of sample N73b measured as a function of temperature. The irradiated region is quite big ($2\,\mu\mathrm{m x} 4{,}31\,\mu\mathrm{m}$), and irradiated region resistance is fairly large compared to the normal state resistance of the leads. Higher fluence leads to higher resistance and somewhat lower T_c, except for the case of the narrowest irradiated region (30 nm), where the effective dose was at least order of magnitude smaller due to the irradiation line broadening.

irradiation not always be very reproducible. Also, in the beginning when the first tests with small irradiated line widths were performed, the irradiation line width was 2 nm in the design, but the resulting line width was ~ 30 nm or more. This resulted in an order of magnitude smaller effective fluence, and was caused by a poor beam optimization that was later improved a lot.

Sample N73b was measured twice four months apart, and measured R(T) curves were almost identical. This implies that disorder created by helium ion beam is not decreased or annealed away over time, which is encouraging observation regarding junctions fabricated using this method.

From samples N7 one can deduce that T_c starts to get suppressed when fluence is over $\sim 1 \cdot 10^{15}$ ion/cm^2. Luckily, this value should not be affected too much by initial disorder concentration. However, this is not the case when T_c suppression as a function of fluence is determined. NbN samples had initial T_c varying between

$4 - 15.7$ K, thus implying big differences in initial disorder, and thereby a more meaningful quantity to compare is T_c/T_{c0}. This quantity is plotted in Figure 42. Unfortunately, while the suppression of critical temperature was seen in many other samples, most of the irradiations were performed with a small fluence or when the initial disorder was strong. Therefore, the data in Figure 42 is not complete and the uncertainties are large. Hence, further investigations on this matter should be performed. However, it seems that sheet resistance behaves roughly as $R_\square \propto x^{5/3}$ while critical temperature behaves roughly as $T_c \propto \sqrt{x}$ where x is the helium ion fluence. This behaviour is purely phenomenological and should only be used to get a rough estimate for the required helium ion dose for each application.

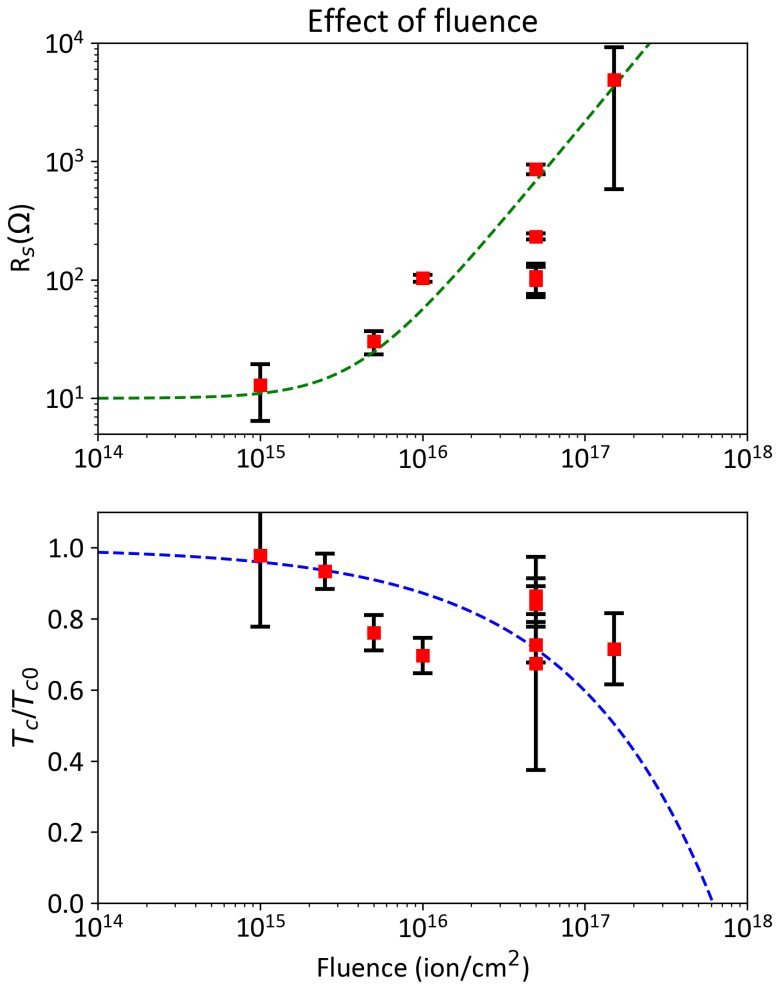

Figure 42. The sheet resistance R_s and the normalized critical temperature T_c/T_{c0} plotted as a function of helium ion fluence. The dashed lines are guides to the eye, and the green line is the function $f_1(x) = 10\,\Omega + A_1 x^{5/3}$, while the blue line is the function $f_2(x) = 1 - A_2\sqrt{x}/15.7\,\mathrm{K}$, where x is the helium ion fluence (in units ion/cm^2), $A_1 = 10^{-24}\,\Omega \cdot (\mathrm{cm}^2/\mathrm{ion})^{5/3}$ and $A_2 = 2 \cdot 10^{-8}\,\mathrm{cm{\cdot}K}/\sqrt{\mathrm{ion}}$. Sample thicknesses are between $15\,\mathrm{nm}$ and $68\,\mathrm{nm}$. In the sheet resistance plot, one data point with high R_s is omitted because the high sheet resistance is due to probably a measurement error.

6.4.3 SNS junctions

As presented above, a T_c suppression of NbN is possible with a helium ion beam. In order to make Josephson junctions, the irradiated line width was decreased down to few tens of nanometers.

The sample N72 was fabricated using originally a 195 nm thick NbN film on MgO substrate with critical temperature of 15.7 K, by thinning the whole film with RIE etching down below 15 nm. Because of such a substantial thinning, the film thickness was not completely homogeneous. There were also some residues on top of the film, for example some nanoparticles from an unknown source at the edge of the sample (Appendix A.2, Figure 74). After the thinning, the critical temperature was decreased down to roughly 7 K, implying that the film is of lesser quality near the substrate. Thus, for these samples initial disorder was probably already quite high. A superconducting wire with width of $2\,\mu\mathrm{m}$ was fabricated on this sample, and subsequently five junctions were fabricated on the wire using helium ion irradiation. Irradiation was performed using spot size of 4 and with different fluences. Irradiation linewidth was estimated from carbon deposit to be ∼40 nm. This differs a lot from values reported in Table 1, because beam was not very well optimized causing a large beam size.

The resistance as a function of temperature for all of the mentioned junctions is plotted in Figure 43, showing that four of the junctions were superconducting above 4.2 K. T_c:s of the superconducting leads are difficult to estimate, but T_c is roughly ~ 6.5 K for the N723, N724 and N725 leads while T_c for the N722 lead is ~ 5.3 K. Equation (6) can be used to estimate the superconducting gap, and these T_c:s correspond to the gap of 1.0 meV and 0.8 meV, respectively.

The junction N721 made with the lowest fluence ($5 \cdot 10^{16}$ ion/cm^2) had the highest resistance, but this is probably because sample was thinner in the region where junction was made. From Figure 43 it can be seen that for many samples the transition is broad with the resistance slowly decreasing over several Kelvin before vanishing, implying either the presence of granularity [109] or thermally activated phase-slipping[1]. The resistance of the sample N721 shows a finite value even at 4.2 K, and because junction was not measured at lower temperatures it is difficult to estimate what is the nature of this junction. Unfortunately, with these junctions electrical transport measurements were not performed before the helium ion irradiation, hence the initial R(T) characteristics are unknown.

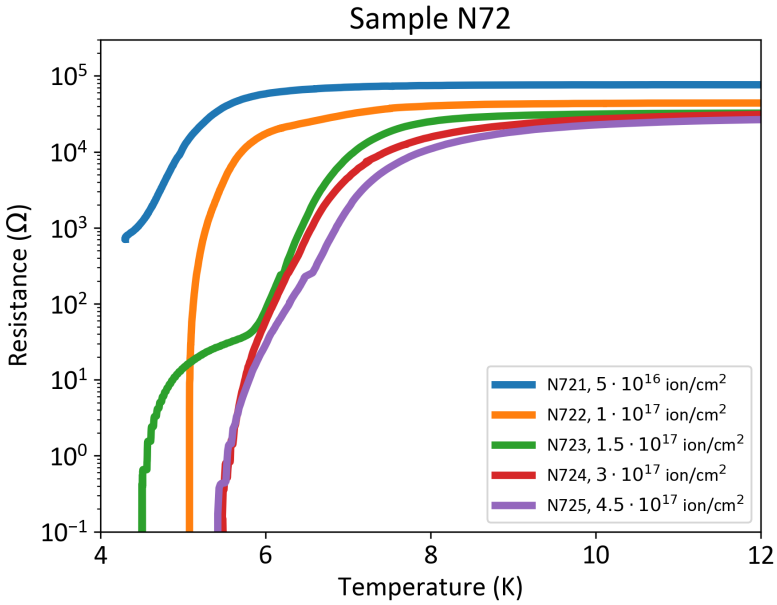

Figure 43. Resistance as a function of temperature of junctions on sample N72 plotted using logarithmic scale. Resistance does not drop as sharply as one would expect, which implies presence of phase slipping and/or granularity [1].

Junction N723 was fabricated using a $1.5 \cdot 10^{17}$ ion/cm^2 fluence, and the film thickness was 15 nm. The IVC characteristics of this junction are shown in Figure 44, and the numerically calculated differential conductance in Figure 45. The IVC behaves slightly abnormally as a function of temperature, but this is expected as also the R(T) behaviour of the junction indicates the presence some additional resistive contributions in the temperature range 4-6 K. The differential resistance of the junction shows a supercurrent at 4.3 K and a relatively linear resistance at larger voltages. At higher temperatures, there is no supercurrent but still a clear drop in resistance is present at zero bias. The critical current of the junction was quite small, only $1\,\mu$A, while the characteristic voltage $I_c R_n$ of the junction was $35 \pm 5\,\mu$V.

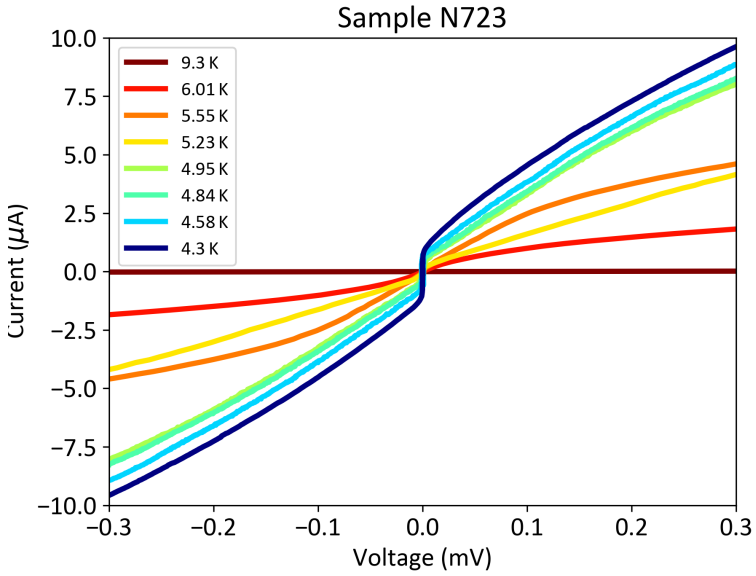

Figure 44. Current-voltage characteristics of junction N723 measured at different temperatures. IVC shows a clear non-hysteretic SNS-type behaviour with a relatively linear behaviour at larger voltages.

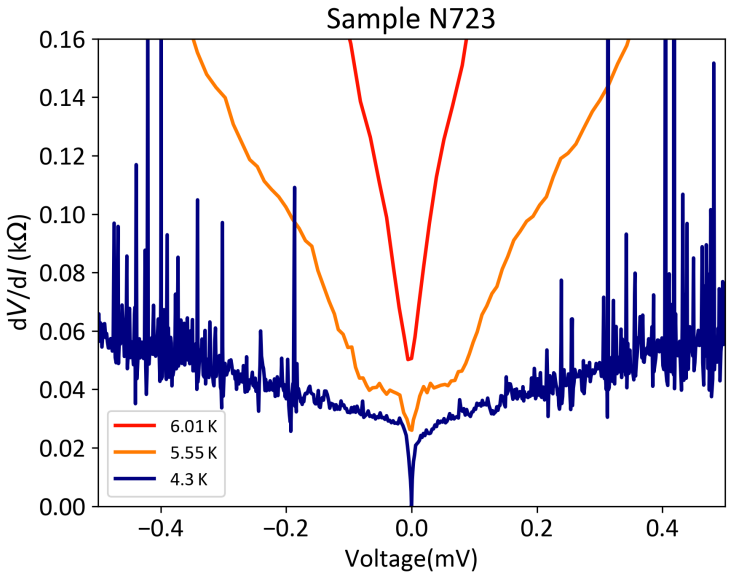

Figure 45. Differential resistance of junction N723 at three different temperatures. The junction resistance drops at zero voltage even at higher temperatures.

Other junctions fabricated on the same chip showed also SNS-type behaviour, but there was some phase slipping observed in these junctions. The resistance as a function of temperature of all junctions on sample N72 are shown in Figure 43, while some of the measured IVC:s can be seen in Figures 46-47. It is disputable whether these are true SNS junctions, or if there is so called phase-slip lines resulting in the measured IVC:s. In phase slips, magnitude of the superconducting order parameter $|\Delta|$ fluctuates to zero, and this allows phase difference rotate by 2π before $|\Delta|$ is restored, resulting to a voltage pulse given by equation (12). These phase slips occur in the center of so called phase slip centers, and these centers can interact, forming the phase slip lines [110], [111]. Hence, the most probable explanation for the jumps observed in IVCs is that these phase slip lines form to the irradiated region. This means that the phase increases at different rates on the two sides of irradiated region, causing jumps to the IVC whenever there is a phase slip event.

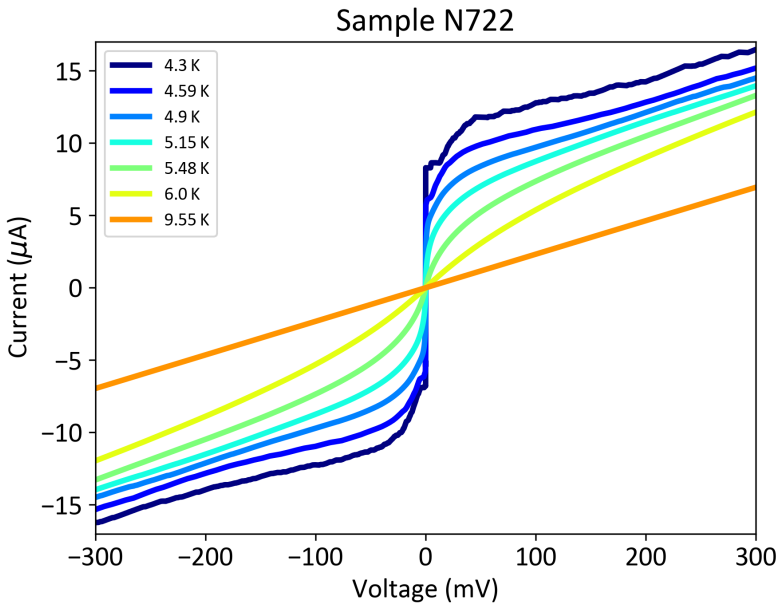

Figure 46. Current-voltage characteristics of junction N722 measured at different temperatures. Clear SNS-type behaviour is observed, and junction does show some minor hysteresis. Critical current of the junction is $8{,}3\,\mu\mathrm{A}$. There are current steps visible in the IVC especially with the small voltages.

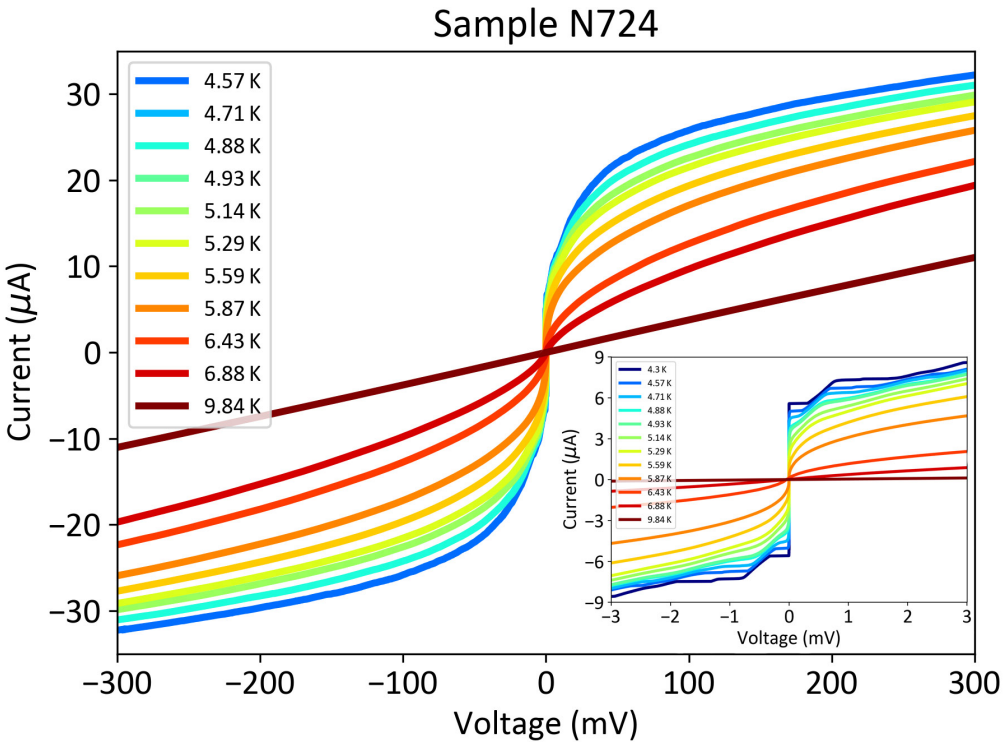

Figure 47. Current-voltage characteristics of junction N724 measured at different temperatures. The junction does not show major hysteretic behaviour, but at lower voltages (inset) current steps are visible. These steps occur also outside of the gap voltage, suggesting that the steps are due to phase slip lines.

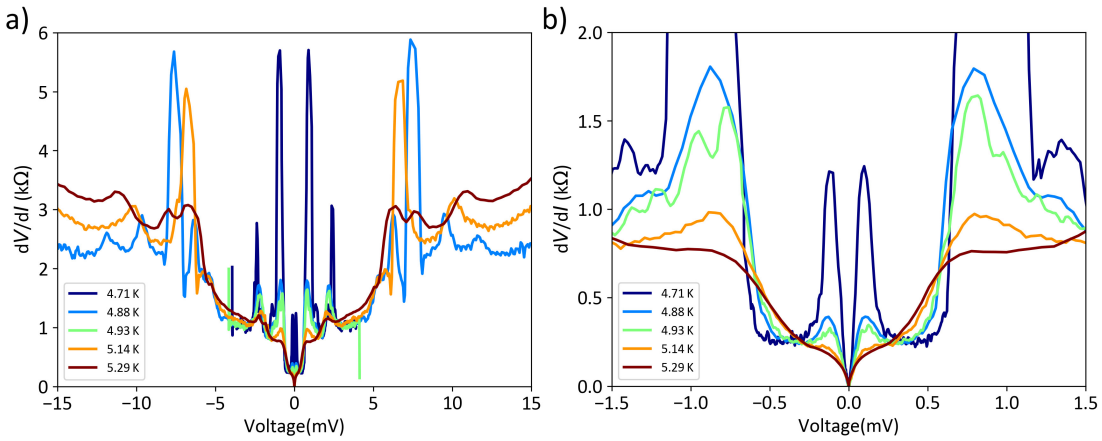

Figure 48. The differential resistance of junction N724 measured at different temperatures, revealing clear symmetric resistance peaks. Figures a) and b) show behaviour at different voltage ranges.

Peculiar R(T) results were encountered also with other samples, like in junctions made from the sample N63l. In these junctions, a finite resistance persisted down to 4.2 K (Figure 49), but current-voltage characteristics (Figure 50) and the numerically calculated differential conductance (Figure 51) showed complex features. Most likely these are due the phase slipping phenomena observed already above. An interesting feature is a clear zero-bias conductance peak in the differential conductance presented in Figure 51.

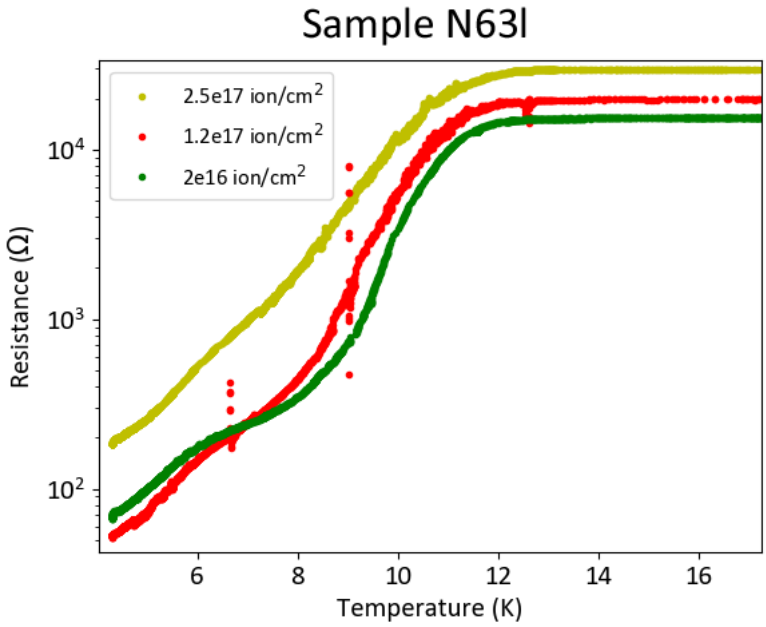

Figure 49. The resistance of junction from sample N63l plotted as a function of temperature using logarithmic scale. A finite resistance persists down to liquid helium temperatures.

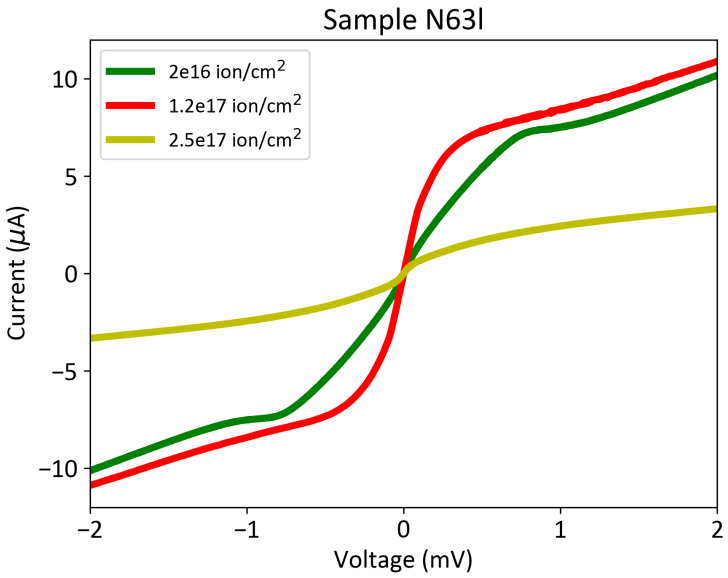

Figure 50. Current-voltage characteristics of junctions from sample N63l measured at 4.2 K. Although resistance of the junction remains finite, IVC shows interesting behaviour near superconducting gap.

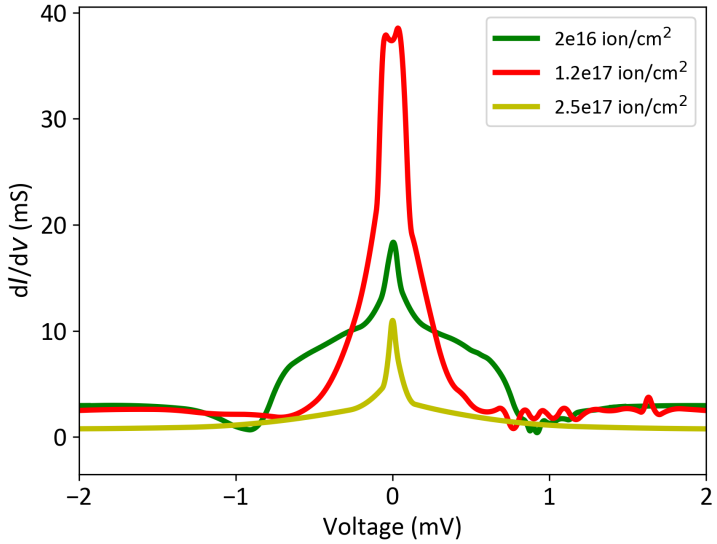

Figure 51. The differential conductance of sample N63l junctions measured at 4.2 K. Zero bias conductance peak is clear, as well as additional features near the superconducting gap (~ 1 meV).

In many SNS junctions fabricated from NbN there was strong hysteresis. For some reason, even if at higher temperatures junction exhibit non-hysteretic SNS behaviour, at lower temperatures hysteresis was often really prominent. The most drastic effect was when in some of the junctions fabricated using small helium ion fluences, suppression of the critical current was observable when voltage bias was decreased, but upon increasing the voltage, supercurrent persisted up to several times larger values, followed by direct hop to normal state of the bulk wire. Explanation behind this behaviour is still unclear. However from with large enough fluences, hysteresis problem was not that severe.

Pushing NbN thin films to the insulating side of SIT using helium ion beam was not demonstrated in this project, probably just because there were not enough tests performed with high enough helium ion fluence. Because NbN hosts disorder driven SIT, it is likely that fabrication of insulating barrier is possible using helium ion irradiation. Thus, further investigations on this matter should be performed in the future.

6.5 Niobium titanium nitride thin film samples

6.5.1 Niobium titanium nitride

Niobium titanium nitride is a compound combining the high T_c of NbN and the low resistivity of TiN, resulting in an attractive alternative for use in superconducting electronics. The best composition depends on the use, but T_c of NbTiN seems to have peak up to $\sim 17\,\mathrm{K}$ with $Nb_{0.6}Ti_{0.4}N$, where resistivity is significantly smaller than in pure NbN [112], [113]. NbTiN can be used in the same superconducting applications as NbN and TiN, and for example it has been used to create rf cavities [112], low noise SIS mixers [114] and SNSPDs [115].

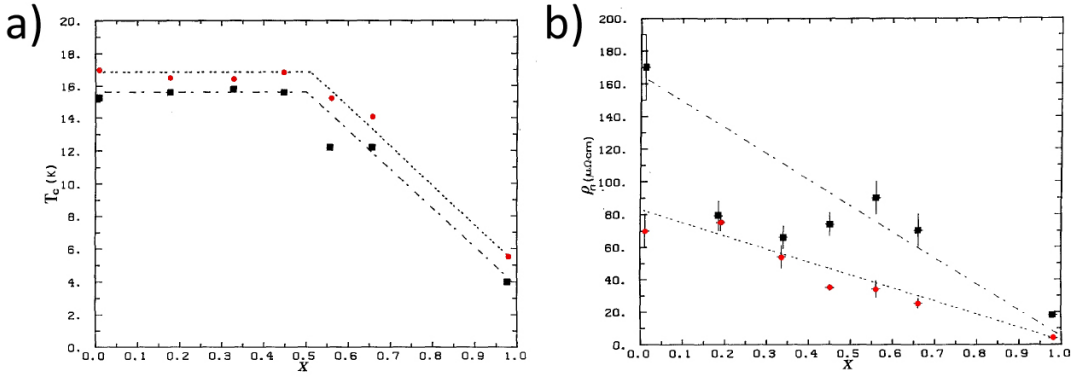

Figure 52. Superconducting critical temperature (a) and low temperature normal state resistivity ρ_n as a function of titanium composition x for $Nb_{1-x}Ti_xN$. Deposition is done with magnetron sputtering, using substrate temperatures of $600\,^{\circ}\mathrm{C}$ (red circles) or $200\,^{\circ}\mathrm{C}$ (black squares). Figure adapted from [112], reprinted with permission. ©1969 Springer Nature.

As was the case with NbN and TiN, NbTiN also hosts a disorder driven superconductor-insulator transition [116]–[118]. In NbTiN, the superconductor-insulator transition is complex as well, and for example the intermediate Bose metal state [118] and the charge-BKT transition [116] have been observed in disordered NbTiN thin films. The intervening Bose metal phase emerged when the sheet resistance exceeded $h/4e^2$. The resistance of insulating NbTiN films did show the same hyperactivated behaviour as in TiN, but the transition was happening at slightly higher temperatures [117].

6.5.2 Tc suppression

Suppression of superconductivity in NbTiN was demonstrated, and some of the measured T_c:s are in Figure 53, showing temperature dependence of the resistance for the irradiated lines fabricated with different fluences on 100 nm thick and $2\,\mu\mathrm{m}$ wide superconducting wire. Irradiation linewidth was 100 nm. Using higher fluence, sheet resistance was increased and T_c was suppressed, and ultimately T_c was suppressed below 4.2 K.

To get an idea how one can control the disorder and T_c using the helium ion beam, in Figures 54 and 55 we plot T_c and the sheet resistance as a function of helium ion fluence, respectively. Here, fluence is not the fluence set to the pattern generator but "true" fluence that is estimated using the ratio between the actual irradiated area size and the irradiation size in the pattern design. Several junctions showed a clear insulating behaviour, thus T_c of these junctions is expected to be zero, but as measurement was only down to 4.2 K, errorbars are shown up to this temperature.

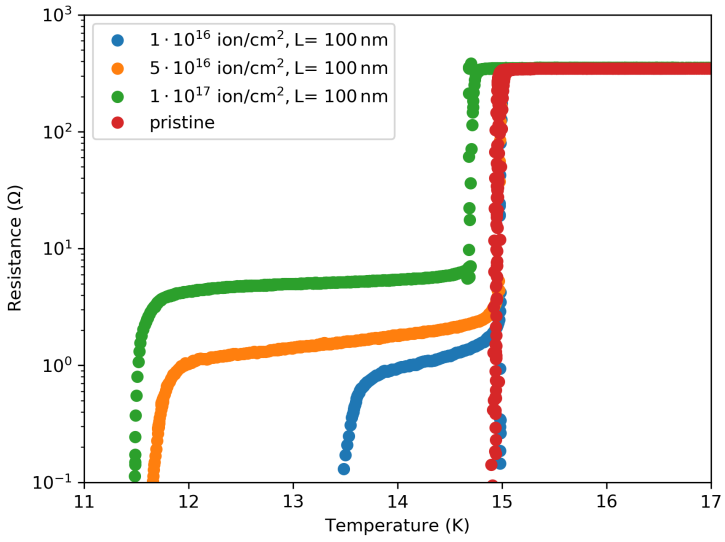

Figure 53. Tc suppression in NbTiN samples after helium ion irradiation with different fluences. Higher fluence results to lower critical temperature. Width of the superconducting wire is $2\,\mu\mathrm{m}$ and thickness is 100 nm.

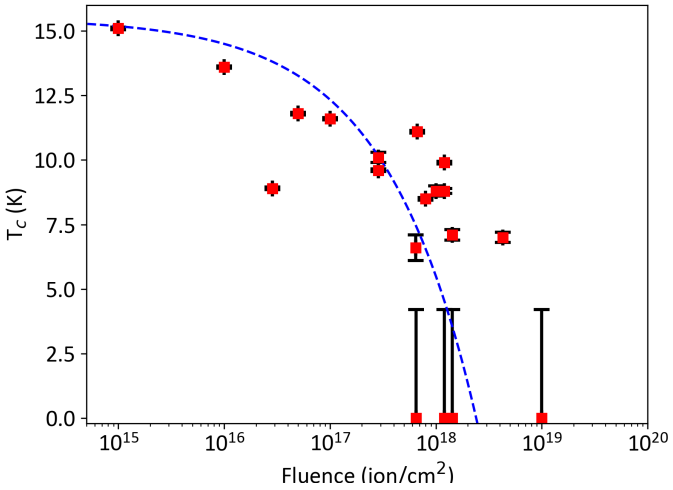

Figure 54. T_c suppression as a function of corrected helium ion fluence in semilogarithmic scale for NbTiN samples. The dashed blue line is a guide to the eye, showing that $T_c \sim 15.5\,K - C\sqrt{x}$ where x is helium ion fluence in ion/cm^2 and $C = 1 \cdot 10^{-8}\sqrt{\text{ion} \cdot \text{K}^2/\text{cm}^2}$.

From Figure 54 one can see that, to a rough approximation, T_c seems to follow behaviour $T_c \sim 15.5\,K - C\sqrt{x}$, where x is helium ion fluence in ion/cm^2 and $C = 1 \cdot 10^{-8}\sqrt{\text{ion} \cdot \text{K}^2/\text{cm}^2}$. This equation can be used to obtain a rough estimate for the required helium ion dose to get a given T_c suppression, but as this equation is purely phenomenological, one should not make any additional conclusions.

Sheet resistances were calculated using Eq. (35), for which length of the irradiated region was estimated using the values in Table 1. The resistance was determined to be the value just before the superconducting transition. Both the resistance and the length values had larger uncertainties, and the total error was calculated using the usual error propagation equation. In Figure 55, the sheet resistance is plotted against the helium ion fluence, and it is evident that there is a lot of spread in the values. Sheet resistance measures indirectly the amount of disorder present in the sample, but from Figure 55 it is difficult to extract any trend, and this is due to large scatter of the sheet resistance values.

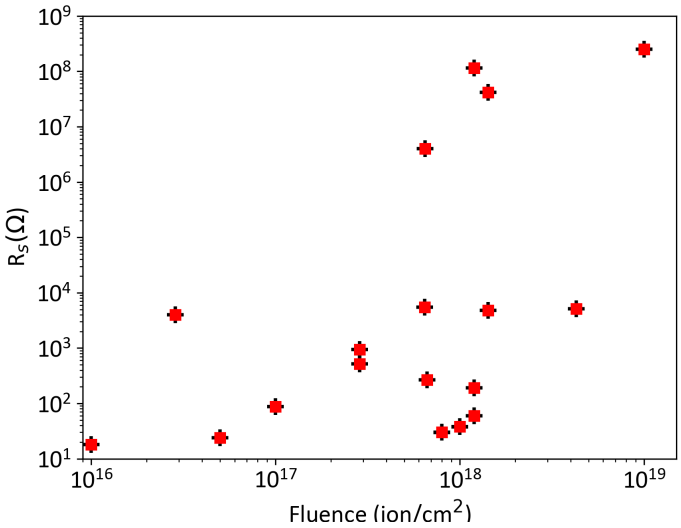

Figure 55. The sheet resistance of the irradiated area as a function of helium ion fluence in logarithmic scale. Differences in beam and sample details result in very different irradiation effects, hence there is big spread in the irradiated area resistance.

In order to compare with theoretical predictions and to get an estimation how disorder affects the superconducting critical temperature, it was also plotted as a function of sheet resistance (Figure 56). The measured data was compared to Finkelstein's prediction, Eq. ((50)) using different mean free times and suitable superconducting temperatures.

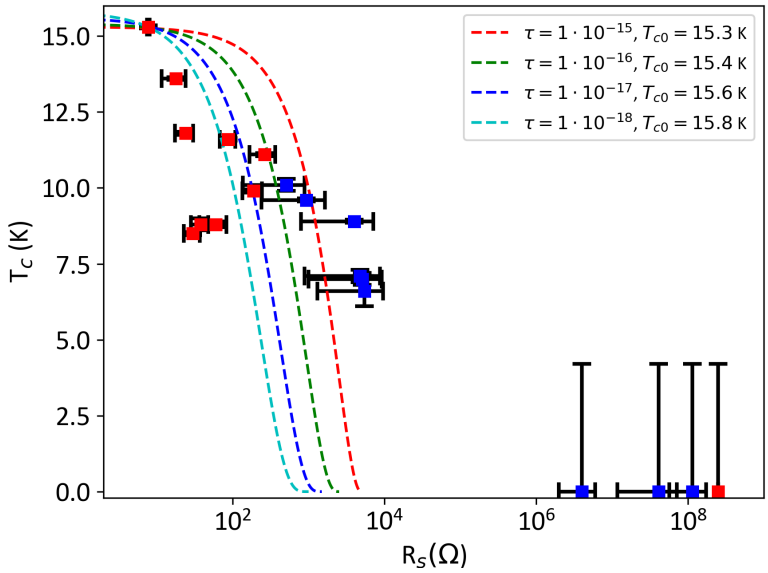

Figure 56. T_c as a function of sheet resistance R_s for the irradiated NbTiN regions. The blue points are from junctions with irradiated region length less than 10 nm, the red points are bigger regions. The dashed lines are the fermionic scenario predictions (Eq. (50)) using different parameter values. Sheet resistance is plotted in logarithmic scale, and hence the deviations from the fermionic scenario are quite large.

The interpretation of Figures 54-56 has several pitfalls. For Figure 56, one should note that it is not possible to get a reasonable fit to Finkelstein's theory, and the deviation from the prediction is quite large. A reasonable value for the mean free time is of the order $\tau = 1 \cdot 10^{-16}$ s [48], [107], which along other values does not fit very well. Figure 56 has a logarithmic scale for R_s, while in linear scale it would be evident how poorly the theoretical prediction fits. However what this implies is not that straightforward.

As was explained previously, the length of the irradiated region is difficult to know, and needs to be estimated using the values in Table 1. However, in reality, each damaged area should be imaged individually to ensure that thermal drift of the stage has not resulted in a wider than expected damaged area. This is especially the case for long exposures, and thus at the end of the project, there was effort to push the irradiation time down by decreasing the width of superconducting wires.

Another major source of uncertainty in the sheet resistance calculation was introduced when the resistance value was determined. In some cases, the resistance was almost linearly decreasing as a function of temperature, and while this also resulted in a larger error to T_c, the biggest error was introduced to the resistance. Also, the determination of the normal state resistance from the current-voltage characteristics asymptote was sometimes difficult, because of a high nonlinearity present also at large voltages, as well as at the vicinity of the superconducting transition in leads. These introduce major uncertainties to Figures 55 and 56.

Apart from the large errors in determination of the sheet resistance and the irradiated region length, the interpretation of Figures 54 and 56 possesses also another problem. Because most of the measurements are from a SNS junctions, the appearance of Josephson supercurrent is problematic when comparison to SIT predictions is wanted. This supercurrent prevent the detection of the normal metal phase for short enough weak links, because the measured T_c is the point where the proximity effect allows the supercurrent to flow regardless of the actual T_c of the weak link. This prevents determination of possible metallic phase in the weak link. Thus Figure 56 should be interpreted more as an loose proof of the presence of Josephson effect in the system, and the validity of SIT theory predictions should not be estimated from it. However, let us point out that red points denoting larger length junctions can be fitted better, so it is possible that the fermionic scenario could apply here.

6.5.3 SNS junctions

Because the suppression of T_c was again demonstrated to be possible, it is evident that SNS junction fabrication should be possible. This turns out to be the case, and some successful SNS-type Josephson junctions were fabricated out of NbTiN. As before, the width of superconducting line was $2\,\mu\mathrm{m}$ in most cases, although in most recent designs this was reduced to 500 nm in order to reduce the irradiation time. SNS junctions were characterized only by means of R(T) and IVC measurements. A lot of NbTiN samples with SNS characteristics were made, and thus only representative set of samples are presented in what follows.

Unlike other NbTiN films, the film J12 was deposited on 50 nm thick SiN on Si substrate. The film thickness was 100 nm, and this was not thinned with RIE, and all the devices fabricated from this film had the same thickness. The critical

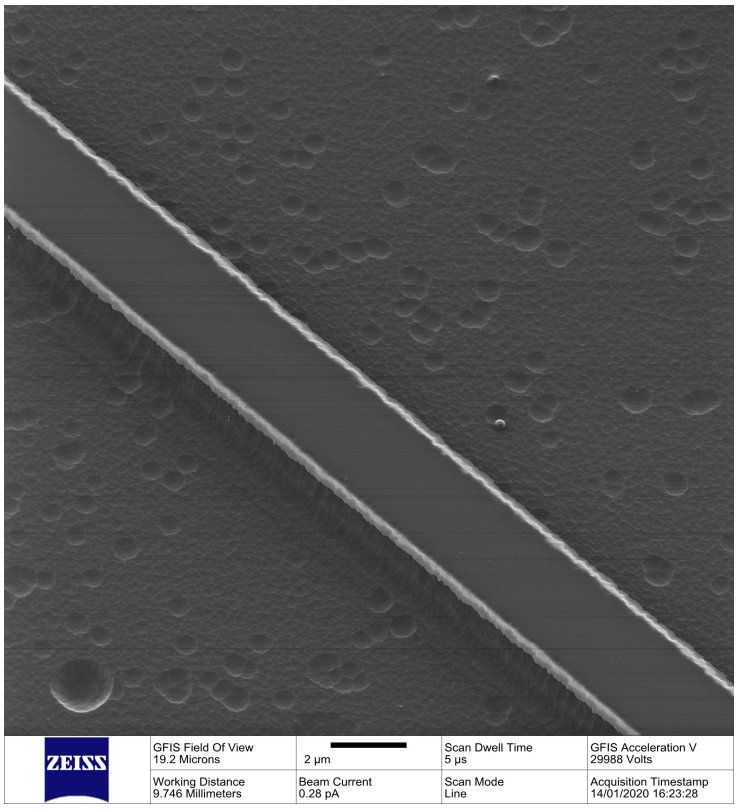

Figure 57. Helium ion microscope image of superconducting wire fabricated using 100 nm thick NbTiN film on SiN/Si substrate. Pattern was overetched, and thus also the underlying silicon substrate was etched.

temperature of the bulk film was 15.3 K, a highest value achieved for NbTiN during this project. Sample J12LD was etched slightly too long, and during etching both NbTiN and SiN were etched through, and after this Si was etched with quite high rate producing $\sim 1\,\mu\mathrm{m}$ deep walls (Figure 57).

Most samples were fabricated using a width of $2\,\mu\mathrm{m}$ for the superconducting lines, and thus the junction area is $\sim 0{,}2\,\mu\mathrm{m}^2$. The most successful SNS junction from this batch was J12LD3, fabricated using $1.2 \cdot 10^{18}$ ion/cm^2 fluence with 20$\pm$10 nm long irradiated area. This sample showed a large hysteresis, critical current of 1.3 mA and characteristic voltage of $I_c R_n = 9 \pm 1$ mV (Figure 58). The normal state resistance was difficult to define because of the nonlinearity of the IVC asymptote and vicinity of the critical current of the leads ($\sim$ 2 mA), and this is the reason for the large uncertainty of the estimated $I_c R_n$ product.

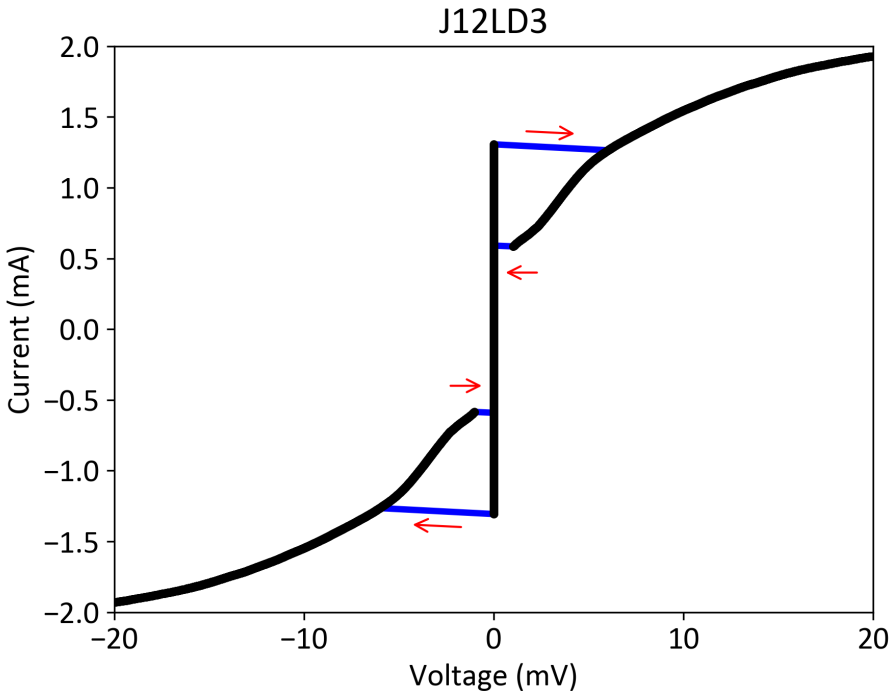

Figure 58. Current-voltage characteristics of sample J12LD3 measured at 4.2 K. The sample was fabricated using $1.2 \cdot 10^{18}$ ion/cm^2 fluence and length of the junction is approximately 20 nm.

For sample J12LD2 fabricated otherwise similary but with a $1 \cdot 10^{18}$ ion/cm^2 fluence, IVC was similar when current was decreased and the retrapping current was same 0.6 mA, but the critical current was same as bulk leads. This is the same behaviour as was observed in some of the NbN samples.

Junction J12LD5 was fabricated using spot size 0 and fluence of $1 \cdot 10^{20}$ ion/cm^2. Spot size 0 results in irradiation linewidth of approximately 150 nm, and because now the linewidth is due to a badly focused beam, the junction has most likely a gaussian disorder distribution. In the design, the linewidth was 2 nm, so that the effective fluence is actually of the order of $1 \cdot 10^{18}$ ion/cm^2. One note is that this junction was irradiated twice, but the first time irradiation of it was little misplaced and did not alter the IVC nor the R(T) behaviour and hence first irradiation can be neglected.

IVC of the junction J12LD5 shows interesting features, seen in Figure 59. In the IVC there is a lot of nonlinear features over the whole measurement range,

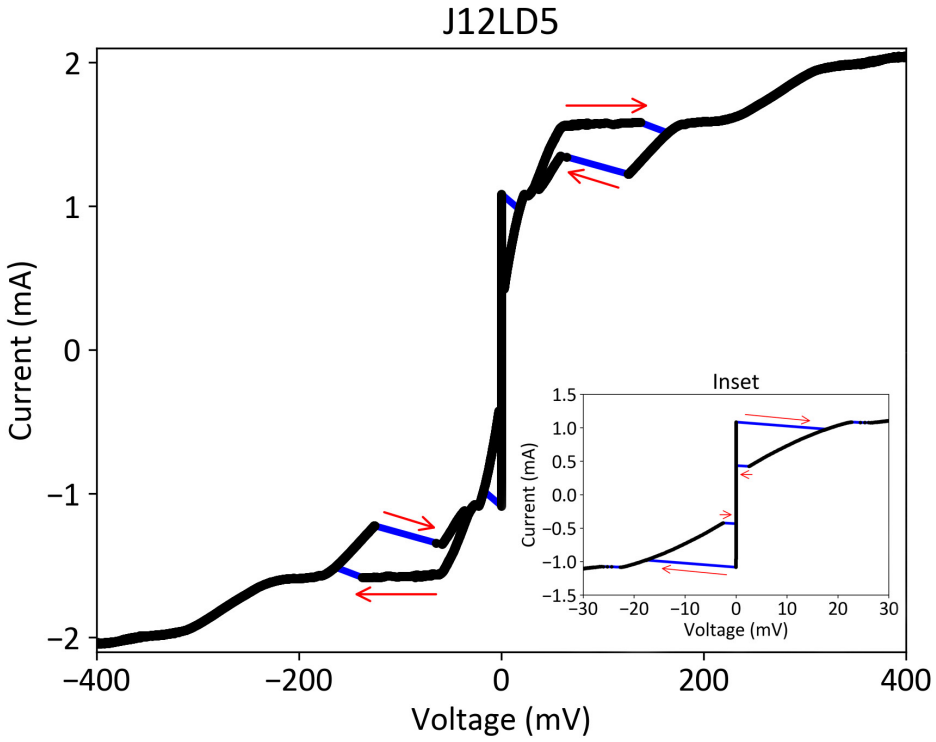

Figure 59. Current-voltage characteristics of sample J12LD5 fabricated using broad helium ion beam, measured at 4.2 K. Hysteresis vanishes at some regions but comes back at large voltage ranges. Inset shows smaller voltage range behaviour that is similar observed in J12LD1.

and hysteresis is quite strong all the way up to ~ 150 mV voltage. Interestingly, there is small non-hysteretic voltage range between $15 - 50$ mV. The origin of these complex features are unknown, but these features are most likely related to fact that the disorder level of the junction is inhomogeneous.

Film J31 was deposited with a shorter deposition time so that the film would be thinner, and from profilometer measurements the film thickness was determined to be 36 ± 3 nm. Because the wider superconducting wire increases helium ion irradiation time, resulting often broadened irradiated lines, for sample J31RD the wire width was decreased to 120 nm. Now, the junction area was just $\sim 4300\text{nm}^2$, so that the junctions are small compared to usual Josephson junctions. From this sample, three successful Josephson junctions were made, exhibiting clear Josephson behaviour. The temperature dependence of the resistance of these junctions is plotted in Figure 60, where is seen that T_c of the superconducting leads

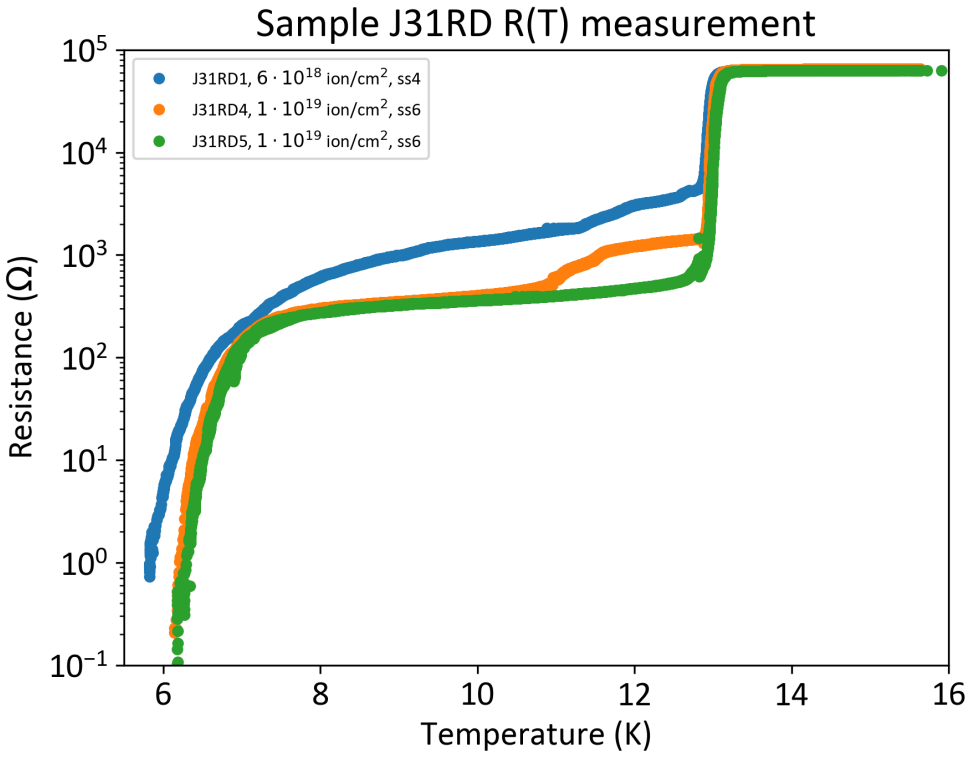

Figure 60. The resistance as a function of the temperature for smaller Josephson junctions. The superconducting critical temperatures are similar, and the same fluence produces almost the same R(T) curves. Additional transition is present in sample J31RD4 near 11 K, but the origin of this is unclear.

is 13.0 K, corresponding to superconducting gap of 2 meV.

Sample J31RD1 was fabricated using a spot size 4 and fluence of $6 \cdot 10^{18}$ ion/cm^2, and the irradiation was done using Zen software and a line irradiation with 1 nm x 1 nm step size. From Table 1 one can estimate that realized length of the junction is 9 ± 5 nm. The resistance of the junction is slightly higher than in the other junctions on the same chip, and after the superconducting transition of the leads, the resistance vanishes smoothly without a clear second transition (Figure 60). Thereby it is rather difficult to determine the critical temperature of the irradiated region precisely. This behaviour can be explained by numerous factors, but it is most likely related to the inhomogeneity of the irradiated region.

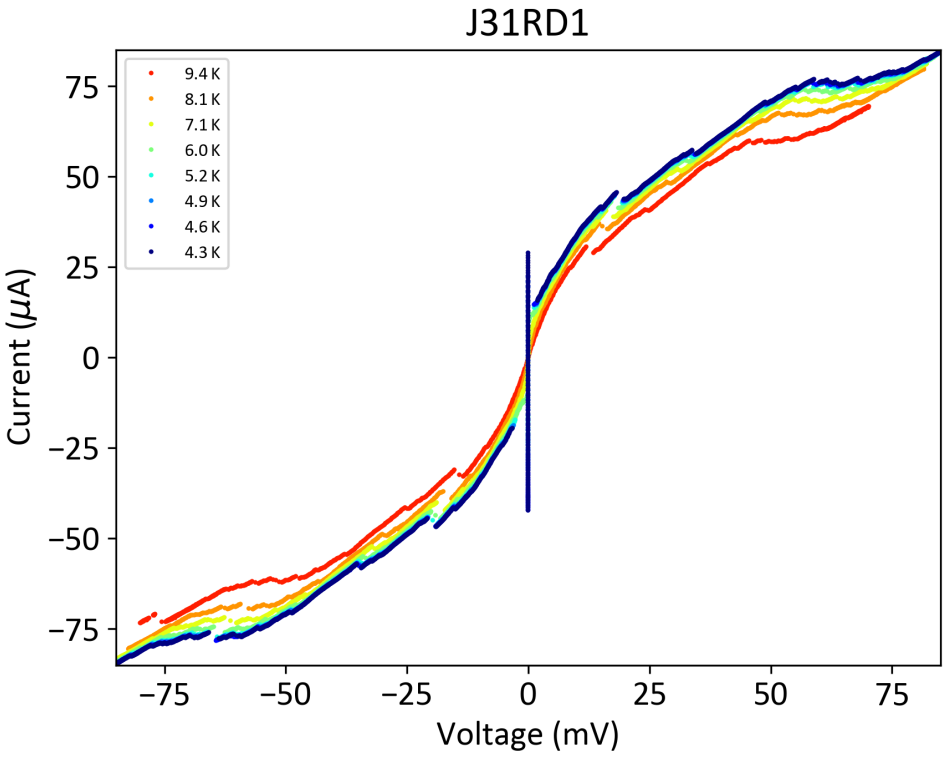

Figure 61. Current-voltage characteristics of sample J31RD1 measured at different temperatures. The IVC is not very hysteretic, but there are clear current steps originating most likely from phase-slip lines.

Current-voltage curves of the junction J31RD1 measured at different temperatures are plotted in Figure 61. The IVC shows very little to none hysteresis, and several current jumps over a large voltage range. These steps are probably due phase slipping observed already with NbN junctions, which might explain some properties of the peculiar R(T) curves. Other noteworthy feature in the IVC is that the supercurrent has considerably higher current value at zero voltage than the current at small voltages in both scanning directions. Again, the IVC is nonlinear up to reasonably high voltages, behaviour encountered in most of the samples. Critical current of the junction is $42\,\mu\mathrm{A}$, and $I_c R_n$ is ridiculously large $40 \pm 5\,\mathrm{mV}$, which implies that it might not be meaningful quantity here.

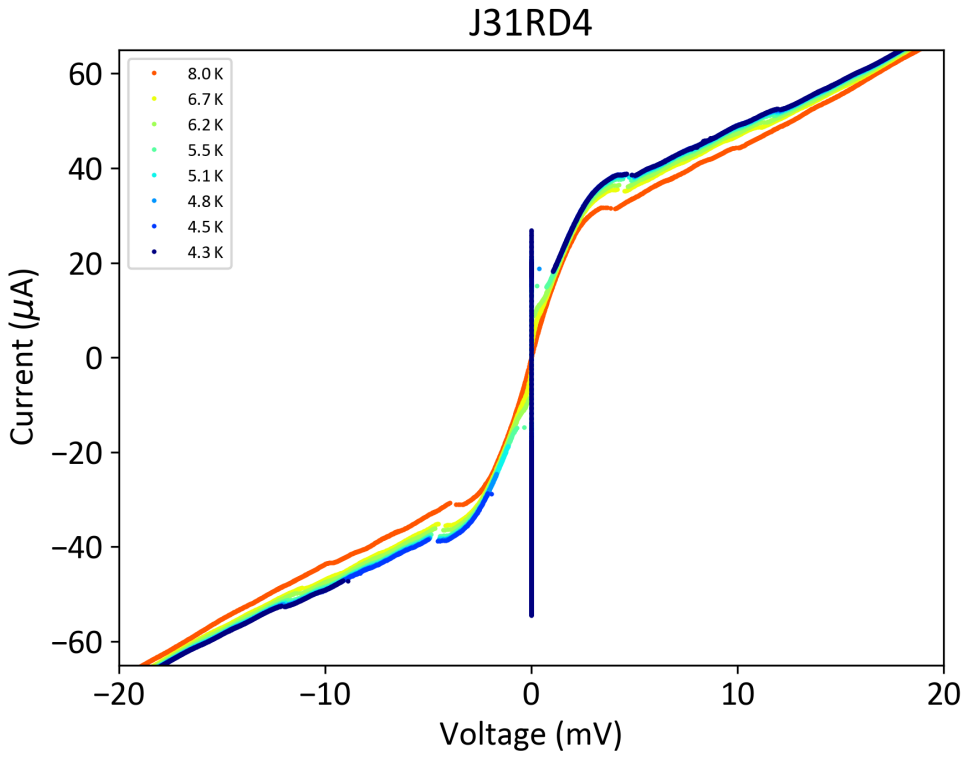

Figure 62. Current-voltage characteristics of sample J31RD4 measured at different temperatures. The IVC does not show as strong phase slipping behaviour as junction J31RD1, but additional "knee" features are present around $4\,\mathrm{mV}$ voltage.

Junction J31RD4 was fabricated using a spot size 6, 3 nm x 3 nm step size in Zen pattern generator and fluence of $1 \cdot 10^{19}$ ion/cm^2 with otherwise same parameters as junction J31RD1. This spot size should produce narrower junction than in J31RD1, with estimated length of $7 \pm 5\,\mathrm{nm}$ (Table 1). Indeed, junction seems to have sharper superconducting transition (Figure 60) and higher critical current (Figure 62). IVC in Figure 62 shows otherwise similar behaviour than junction J31RD4, but now the small steps are not very prominent and otherwise quite linear IVC shows some kind of a knee around $4\,\mathrm{mV}$. R(T) measurement of sample J31RD4 shows additional transition that probably has influence on the measured IVC. The critical current of the junction was $54\,\mu\mathrm{A}$ and characteristic voltage was determined to be $I_c R_n = 15 \pm 2\,\mathrm{mV}$, a slightly more reasonable value than with J31RD1.

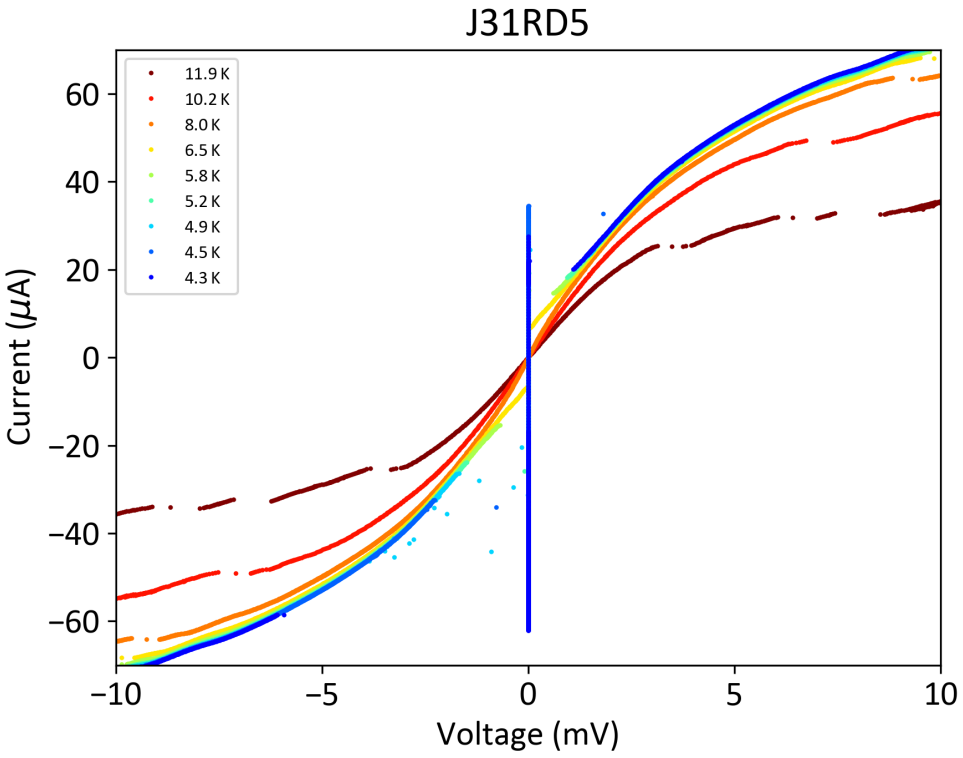

Figure 63. Current-voltage characteristics of sample J31RD5 measured at different temperatures.

Junction J31RD5 was fabricated with the same parameters as junction J31RD4, but now step size of 1 nm x 1 nm was used. This junction shows also some hysteresis at the lowest temperatures, and the IVC shows some steps and nonlinearity at intermediate voltages. Among the three small junctions, J31RD5 has the highest critical current, $60\,\mu\mathrm{A}$, and smallest characteristic voltage $I_c R_n = 10 \pm 2\,\mathrm{mV}$.

All of the junctions J31RD1, J31RD4 and J31RD5 exhibit surprisingly high characteristic voltage. If one uses Ambegaokar–Baratoff equation for SIS tunnel junctions (Eq. (16)) and superconducting gap of the leads ($2\,\mathrm{meV}$), characteristic voltage at 4.2 K is expected to be 3.1 mV. Even though with SNS junctions, this characteristic voltage is expected to be twice as high [33], it is still quite far away from what is observed with these junctions. One possible explanation for the high $I_c R_N$ values is the excess current [1]. This excess current originates from Andreev reflection process, thus indicating that the junctions are indeed SNS junctions.

Another relevant question is how the proximity effect works in a weak link

fabricated this way, as a weak link might consist of localized Cooper pairs or electrons. Because the existence of anomalous Bose metal has been detected in NbTiN, it cannot be ruled out that a Bose metal state arises also in the weak links fabricated here. Because the different nature of the weak link, conventional theories for proximity effect might not apply. This exotic weak link might also explain some of the nonlinearities observed in the IVCs of the fabricated SNS junctions.

6.5.4 Junctions with insulating barriers

When high enough fluence irradiation was used for the NbTiN wires, some samples started to show insulating behaviour. The first sample showing clear insulating behaviour was J1R4, where the irradiated region length was 200 nm. Thickness of the film was ∼100 nm and superconducting wire width was $2\,\mu\mathrm{m}$, the junction area was thereby $\sim 0{,}2\,\mu\mathrm{m}^2$. This sample demonstrated SIS-junction type behaviour, but supercurrent was missing. It is clear that the whole irradiated region cannot be insulating, but the junction is localized somewhere in it. This is possible if the fluence was considerably higher in a localized region. The explanation for this is probably that how Raith pattern generator was sweeping the beam, so that there are lines with higher fluence present. Similar behaviour was observed when the same pattern generator was used for electron beam lithography using a negative resist (Appendix, Figure 75).

The missing supercurrent is probably due to the effect of the electromagnetic environment that suppresses both Cooper pair tunnelling and single electron tunnelling as explained in Section 2.3.1. The high impedance environment needed for dynamical Coulomb blockade originates probably because the junction is small and connected to long and resistive leads ($\sim 10\,\mathrm{k}\Omega$). Also the measurement temperature is quite high, and it is possible that at lower temperatures supercurrent could be observable.

The used fluence was $1 \cdot 10^{18}$ ion/cm^2 but as mentioned, it was probably distributed unevenly. Figure 64 shows the measured IVC characteristics of the sample in linear scale. Reasonable fits to the SIS quasiparticle tunnelling theory, Equation (15), can be achieved using a large Dynes parameter $\Gamma = 0.15$ and a smallish gap value $|\Delta| = 1.0\,\mathrm{meV}$ (Figure 65). T_c of the leads was $15\,\mathrm{K}$, and using Eq. (6) one can estimate superconducting gap to be $|\Delta| = 2.3\,\mathrm{meV}$. Because of how this junction was formed, it is natural that it is more likely of SS'IS'S junction and lower superconducting gap value near the junction is reasonable. This might also produce small "knee" visible near 3.5 mV just over expected location of superconducting gap seen in the Figure 64 [119], [120]. SIS junction simulations were performed by the author using a Python code kindly provided by Mr. Zhuoran Geng.

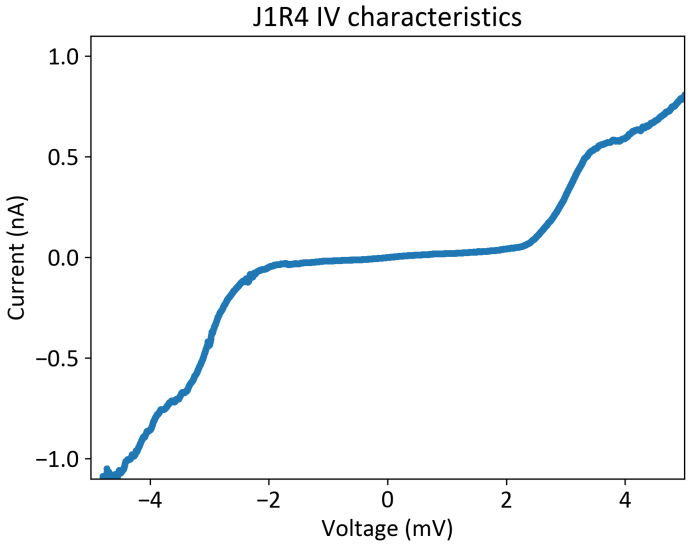

Figure 64. Current-voltage characteristics of sample J1R4. Behaviour is as one would expect for SIS junctions, however the supercurrent is suppressed.

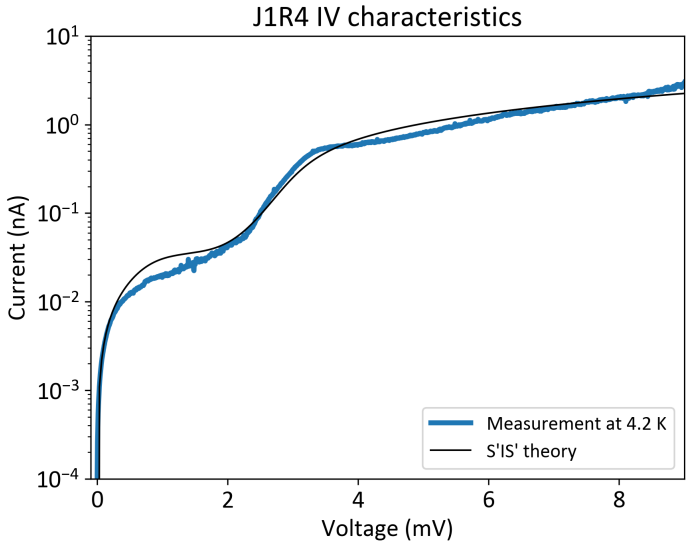

Figure 65. Comparison of quasiparticle tunnelling theory (Eq. (15)) and measured IVC of sample J1R4. Data is fitted quite well with $\Gamma = 0.15$ and $|\Delta| = 1.0\,\text{meV}$. The small knee near $3.5\,\text{mV}$ can not be explained by usual SIS theory, but it can be perhaps explained using the proximity effect and the theory for SS'IS'S junctions [119], [120].

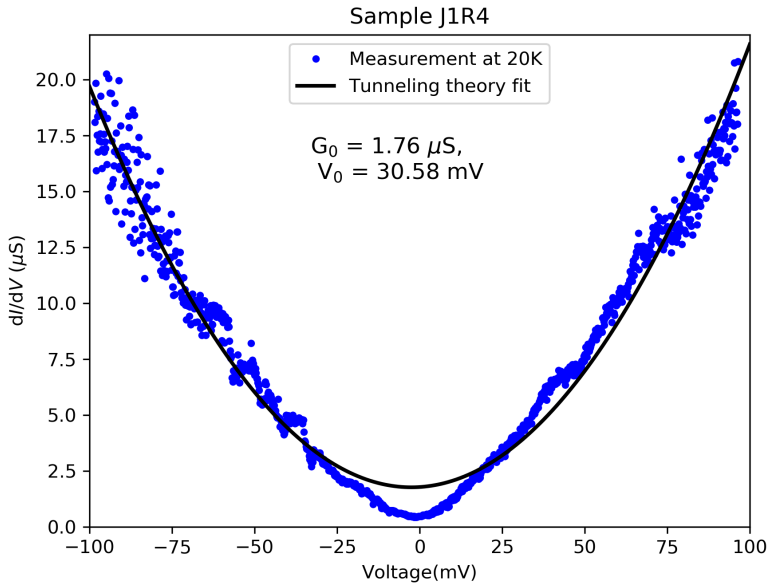

Figure 66. High temperature fit of the Simmons model to the differential conductance of sample J1R4. Fit is reasonable, although some deviation at the low voltage range is present. Parameters obtained from Eq. (31) are $G_0 = 1.76\mu$S, $V_0 = 30.58$ mV, which correspond to 4.6 nm thick barrier with height of ~ 66 meV.

Large bias nonlinearities of the junction persisted at temperatures over the superconducting transition temperature as expected. Thus, in order to extract estimates of the barrier, the IVC measured at 20 K was analysed with the Simmons model describing metal-insulator-metal tunnel junctions. A fit to the Simmons model (Eq (31)) was done to the numerically calculated differential conductance data, and this fit suggested that the barrier thickness is 4.6 nm and height 65.95 meV. This means that the barrier is low and quite wide. It seems that its height is comparable to what is to be expected from AlOx barriers with same thickness [44], which is a promising finding. The simmons model fit to differential conductance data is shown in Figure 66.

After this junction, several samples with insulating barrier were fabricated, now using a much smaller irradiated area lengths so that junction geometry is more clear. These junctions were fabricated using ∼35 nm thick film J32 and superconducting wire width of 500 nm. Junction area was thereby $\sim 0{,}0175\,\mu\mathrm{m}^2$,

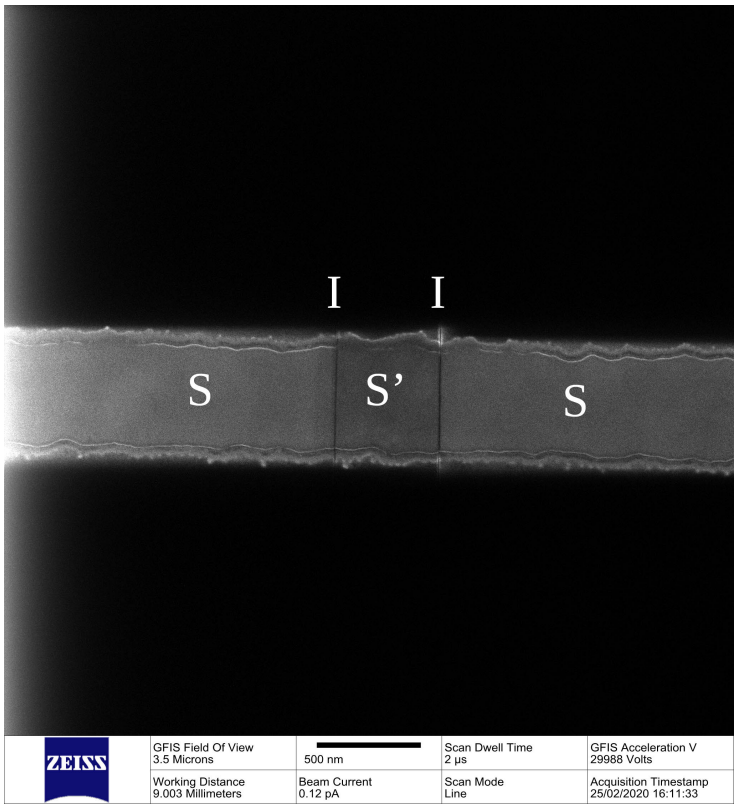

Figure 67. Helium ion image of junction J32LD1. Two separate lines were irradiated using $5.5 \cdot 10^{18}$ ion/cm^2 and $1.1 \cdot 10^{19}$ ion/cm^2, and also middle region was irradiated with low fluence.

and thus the junctions were quite small.

Although it was clear that these junctions had narrow insulating barrier, exact type of the junctions is somewhat unclear. This was partly because there was a significant amount of noise in the measurements, so that sometimes it was difficult to get good IVC measurements. The measurements were performed using a voltage bias, and the measured current often showed some kind of jumping between two levels. This could be due to charge fluctuation induced single electron effects and dynamical Coulomb blockade as discussed earlier. In two of the measured junctions there was strong evidence of the Coulomb blockade effect taking place, as we will discuss next.

Sample J32LD1 was fabricated using high fluence irradiations for two narrow lines and smaller fluence to the region in the middle (Figure 67). The narrow lines were fabricated using spot size of 7 and fluence of $5.5 \cdot 10^{18}$ ion/cm^2 and $1.1 \cdot 10^{19}$

ion/cm^2, so that the junction was asymmetrical. In the middle, the fluence was of the order of $\sim 1 \cdot 10^{16}$ ion/cm^2 and thereby probably too small to substantially suppress T_c.

The target of this fabrication was to produce a SINIS tunnel junction system, but the current-voltage characteristics measurement suggest that there is probably more likely a SIS'IS type of junction. The IVC measurement of sample J32LD1 is shown in Figures 68 and 69. The small voltage range behaviour of the junction (Figure 68) shows the current increasing strongly at roughly near 25 mV, a order of magnitude greater than the superconducting gap, implying that there is Coulomb blockade taking place. When the Coulomb blockade theory for SETs with zero gate voltage is applied, one can estimate that charging energy is ~ 25 meV and capacitance $\sim 6 \cdot 10^{-18}$ F. Excess noise and switching between levels was also present in this sample, particularly clear at the measurement made at lowest temperature. Possible explanation for this is that in the substrate charges jump in a random manner, and this charge is acts as an effective gate charge producing Coulomb oscillation type phenomena.

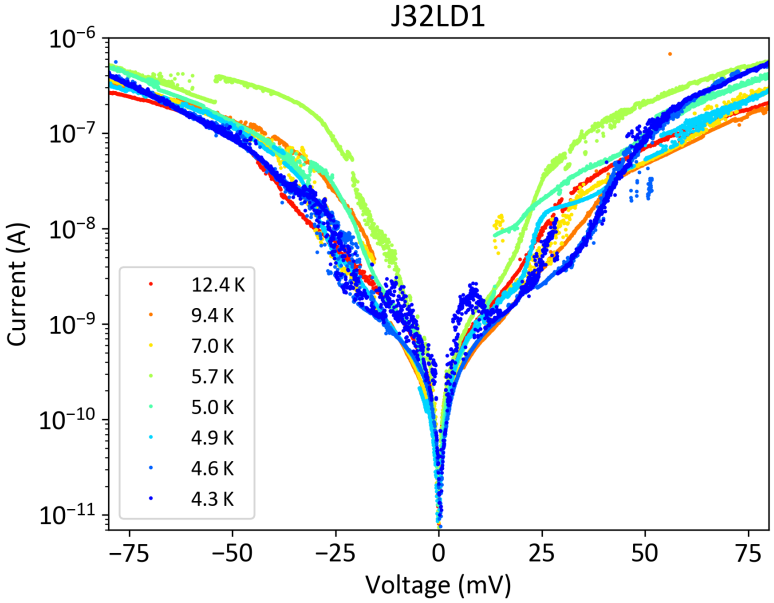

Figure 68. Current-voltage characteristics of junction J32LD1, here the absolute value of the current through the junction is plotted in logarithmic scale. Current is jumping between levels and high level of fluctuations is present.

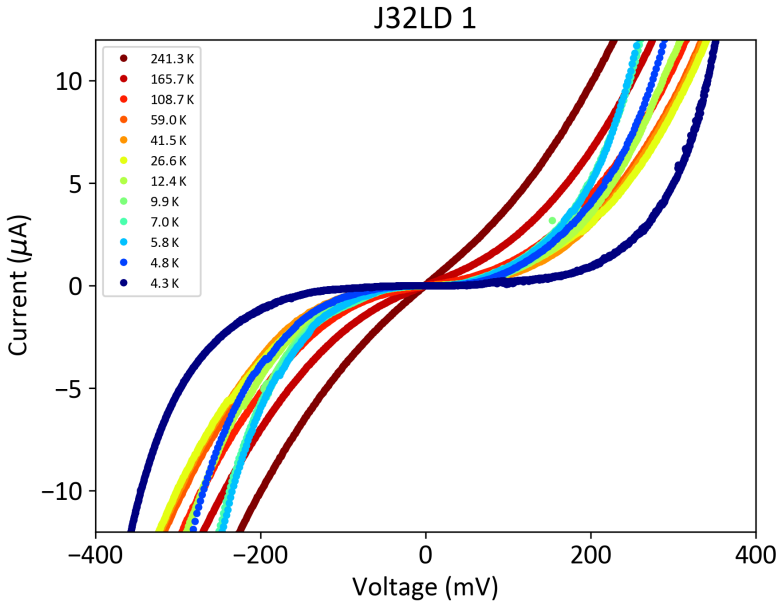

Figure 69. Large voltage range current-voltage characteristics of junction J32LD1. IVC is highly nonlinear over large range of temperatures.

Nonlinearity over a large voltage ranges seen in the Figure 69 was also present in other samples. This nonlinearity is most likely due to fact that the barrier is not a conventional insulator but consists of localized electrons. From Equation (41) one can see that conductivity is exponentially activated when energy is increased, and this is then the same when voltage over the junction is increased. Thus we get a voltage dependent conductivity

$$\sigma(V) = \sigma_0 \mathrm{e}^{-(E_m-(E_F+eV))/k_BT}, \tag{55}$$

which could explain this behaviour. To be able to confirm that the barrier consists of localized electrons, the resistance as a function of temperature for all insulating barriers will be discussed below.

A similar Coulomb-blockade type of behaviour was encountered also with the junction J32RU3, which was fabricated using a single HIM irradiation line. Figure 70 shows the differential resistance measured as a function of voltage for junction J32RU3, presenting zero bias resistance peak suggesting Coulomb-blockade type behaviour. This behaviour of the sample is most likely due to dynamical Coulomb blockade originating from tunnelling in electromagnetic environment as discussed

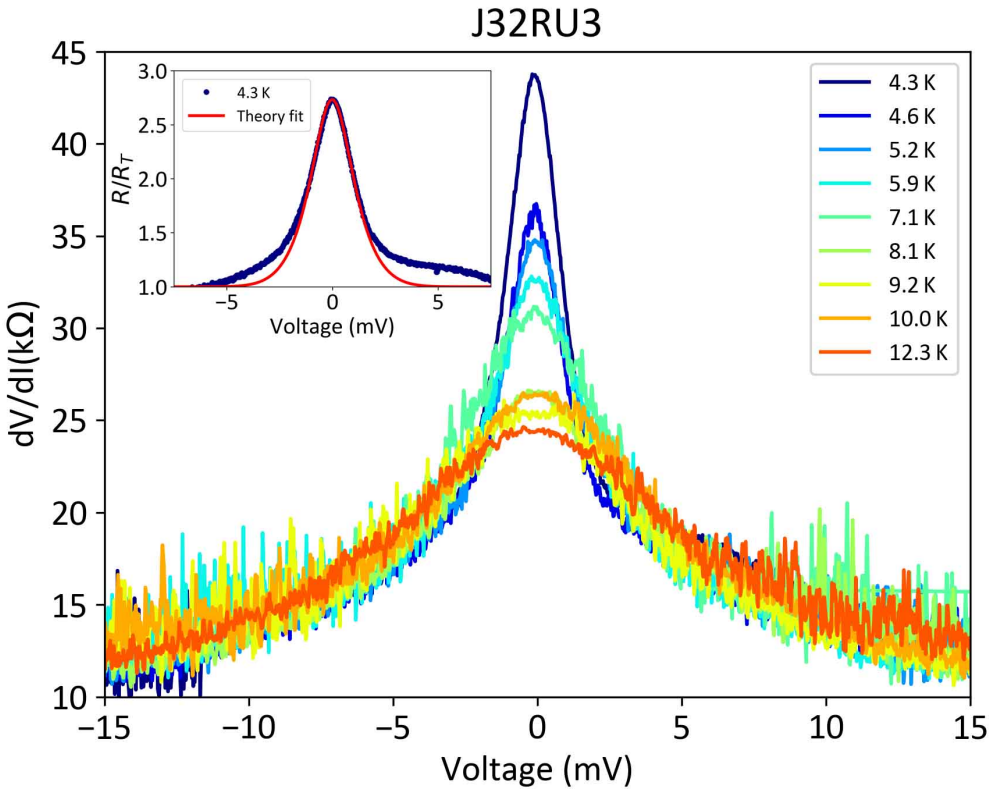

Figure 70. Measured differential resistance of junction J32RU3 as a function of voltage. Resistance peak corresponds to what is expected by dynamical Coulomb blockade theory. Inset shows a dynamical Coulomb blockade theory (Eq.(27),(29)) fit with $E_c = 1.2\,\text{meV}$ to the normalized differential resistance R/R_T measured at 4.3 K.

in section 2.3.1. Because the leads connecting junction are long and narrow, they are quite resistive ($\sim 10\,\text{k}\Omega$), and this may be one explanation for the high impedance environment needed to observe this effect.

In order to estimate charging energy E_c of the junction, dynamical Coulomb blockade theory at finite temperature and high impedance limit (equations (27) and (29)) was fitted to normalized differential conductance measured at 4.3 K (Figure 70). With this simple theory, only small voltage range was fitted, because it does not fully explain shape of the resistance peak, and therefore it was not possible to achieve good fit over the whole voltage. Also normalization is difficult, as differential resistance was decreasing also at relatively large voltages.

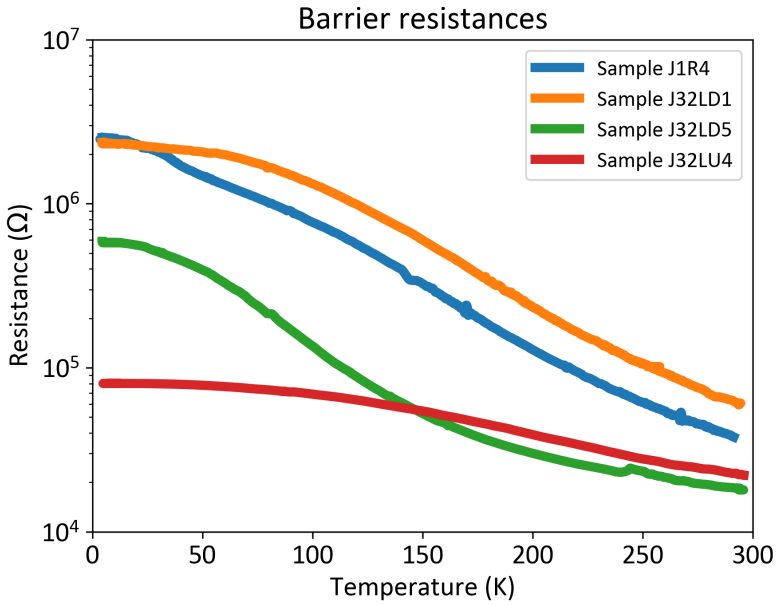

Figure 71. Barrier resistances as a function of temperature for all junctions with clear insulating behaviour. Resistance is increasing exponentially with decreasing temperature, but begins to saturate at low temperatures.

Nevertheless, using $E_c = 1.2\,\text{meV}$ it was possible to get a reasonable fit to the 4.3 K measurement. This charging energy corresponds to the junction capacitance of $\sim 1.3 \cdot 10^{-16}\,\text{F}$. Uncertainties of these values are relatively high because of the simple theory used here. Higher temperatures did not fit as well, and for accurate fits a full, and much more involved, dynamical Coulomb blockade theory should be used. Although this behaviour was not the target when junction was fabricated, this reveals the potential of this method for fabricating extremely small Coulomb blockade thermometers.

To investigate properties of the resulting insulating state, the barrier resistances were measured as a function of temperature from room temperature down to liquid helium temperatures for all junctions with insulating behaviour. This gives some insights to the insulating state properties, as these measurements can be directly compared to for example variable-range hopping theory predictions.

From Figure 71 it can be seen that resistance is increasing exponentially upon decreasing temperature as one would expect for localized electrons. However, there seems to be some saturation at low temperatures which cannot be directly

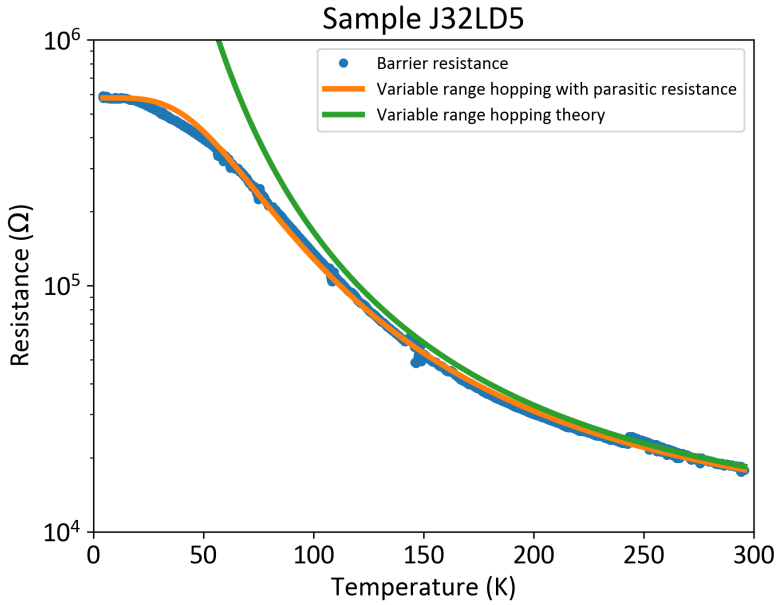

Figure 72. Fit to variable range hopping theory presuming additional series and parallel resistances (orange) and plain variable range hopping theory without additional resistances (green compared to measured temperature dependence of sample J32LD5 barrier resistance. Exponent in the variable range hopping law is $\alpha = 0.3$, reasonably close to Mott's prediction.

explained using e.g. variable range hopping theories. Because all barriers are relatively thin, there might be tunnelling effects contributing to these R(T) curves. One explanation for the resistance saturation is parasitic parallel resistance originating from leak to the ground in the measurement setup. This leak has been observed to be often of the order of $1\,\mathrm{M}\Omega$.

If one assumes an additional series resistance from the leads and a parasitic parallel resistance, reasonable fit to variable range hopping predictions can be achieved. In Figure 72, the resistance as a function of temperature of sample J32LD5 is fitted against variable range hopping prediction (Eq.(45),(46)) using parasitic resistances. The fits gives an exponent $\alpha = 0.3$ close to value predicted by Mott, while $T_0 = 2.7 \cdot 10^5$, and is thus really high. The series resistance in the fit was $8.5\,\mathrm{k}\Omega$, resistance of the barrier at room temperature $60\,\Omega$, and the parasitic parallel resistance $580\,\mathrm{k}\Omega$. The series resistance is about the same as the usual lead resistance is, but the origin of the parallel resistance is not as clear. The pseudo

spin scenario prediction (Eq. (54)) has even stronger temperature dependence than variable range hopping theories, and therefore it does not explain the observed R(T) curves as well. But because origin of parasitic parallel resistance is unknown, one cannot conclusively state that the pseudo spin scenario does not apply here.

7 Conclusions

In this thesis a method to fabricate Josephson junctions in superconducting nitrides using the helium ion irradiation was demonstrated. To our knowledge, this was the first time Josephson junctions were made using this method for conventional low temperature superconductors, thus this work could pave the way for new possibilities in Josephson junction fabrication in the future. In this thesis, suppression of superconductivity was demonstrated in all of the three studied nitrides (TiN, NbN and NbTiN), and subsequently SNS Josephson junctions were fabricated successfully using NbN and NbTiN thin films. Additionally, it was shown that with high enough helium ion fluence NbTiN can be pushed to the insulating side of SIT. Thereby, successful fabrication of insulating barriers was also proven to be possible.

The fabrication steps were designed to be as simple and straightforward as possible. Prior experience in nanofabrication has teached us that usually the best approach is to reduce the number and the complexity of fabrication steps as much as possible to increase success rate. For the fabrication in this thesis, this approach was quite successful, as only especially demanding fabrication step was the HIM irradiation. Towards the end of the project, most of the problems with HIM irradiation were overcome and helium ion irradiation with HIM began to be quite reproducible. Compared to the conventional Josephson junction fabrication, helium ion beam direct writing of the junctions seems to be faster and more straightforward method, because a junction is defined to a wire in a single step.

All the modifications made to the PLD system during this thesis were successful, and now deposition is easier, more flexible and more reproducible than before. Now the PLD can be used to grow not only nitrides, but also elemental superconductors, metals and even complex compounds. Quality of the deposited films has increased, mainly because the lens sweep decreases amount of target material splashes on the film significantly. In addition, overall usability and safety of the system is improved a lot.

Helium ion irradiation was proved to suppress T_c in all the three studied nitrides, and this enables fabrication of Josephson junctions. In addition, T_c suppression by disorder is an interesting topic by itself; although it is somewhat understood, there is very little previous research on superconducting critical

temperature suppression in nitrides by an ion beam. Thereby, this study could pave the way for different ion beam technologies, as well as help to strengthen the understanding of the underlying physics.

In this thesis, suppression of the superconductivity by the disorder induced by an ion beam was directly compared to SIT theories. While lack of datapoints with low enough uncertainties prevents any definite conclusions on this matter, there is some indications that the fermionic scenario might possibly apply with NbTiN. To get better comparison to the SIT theories, more experiments with larger and more homogeneous irradiated regions should be performed in the future. In future studies, possible effect of thickness reduction by ion beam milling could also be investigated.

During this project, Josephson junctions exhibiting SNS type characters were fabricated, although most of the junctions did not behave like ideal Josephson junctions. Large hysteresis was problematic in many of the junctions, especially with NbN. Additionally, SNS junctions fabricated with this method exhibited almost always large nonlinearities even at relatively large voltages. This was often due to the vicinity of the superconducting transition in leads and phase-slipping, but origin of some nonlinearities remained unclear. Another aspect in the SNS type Josephson junctions fabricated, was the exceptionally high I_cR_n values. Even though uncertainties of the determined R_n values were large, because of the nonlinearities in IVC, uncertainty is not large enough to explain these values. A possible explanation for the high I_cR_N values is excess current, and other explanation is that weak link might consist of localized Cooper pairs or electrons. The latter might also explain other peculiar features of measured IVC:s, and further investigations on this matter should be performed.

Nevertheless, high values of I_cR_n are preferred in many applications, and hence this technology is quite promising for Josephson junction fabrication. One potential application for junctions fabricated with this method is RFSQ circuits, where high I_cR_N values are needed. Because of the simplicity and the high resolution of the direct writing method, RFSQ circuits fabricated with this method could potentially be easily scalable.

With high enough fluence, NbTiN films were pushed to the insulating side of the SIT. This is an interesting and an important finding, as now not only SIS junctions can be fabricated, but also the properties of the emerging insulating state can

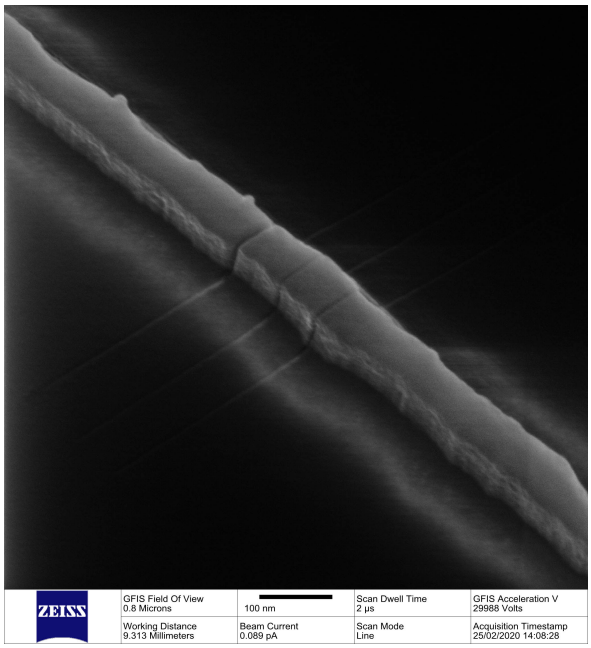

Figure 73. Helium ion microscope image of three small Josephson junctions fabricated to $\sim 50\,\text{nm}$ wide and $\sim 100\,\text{nm}$ thick superconducting TiN wire, demonstrating that with direct writing of Josephson junctions, one can decrease the junction dimensions down to a really small scale. Junctions in the figure have not been measured.

be investigated. The resistance of the insulating barrier increased approximately exponentially, and Mott variable range hopping theory applies reasonably well. Origin of saturation of the resistance at low temperatures should be investigated more thoroughly, in order to determine whether this is a real behaviour of the barrier, or some artifact from the measurement setup.

During this project successful fabrication of SIS junctions was demonstrated. In all of the fabricated SIS junctions supercurrent was suppressed, mostly likely because of dynamical Coulomb blockade that was directly measured in one of the samples. Also small SIS'IS type of sample was fabricated, presenting clear SET-type Coulomb blockade effect. Usually devices exhibiting single-electron effects are difficult to fabricate because of the small size constraints, but with helium ion beam direct writing, fabrication of small enough junctions is far more effortless. Further experiments should investigate the effect of the junction size and how a junction can be fabricated so that there is finite supercurrent over the

junction.

One interesting feature of the fabricated SIS junctions is the large voltage range behaviour. There is a very little existing literature on the topic, but these observed nonlinearities arise most likely because in the barrier electrons are localized by disorder. This nonlinearity could be used in the future for some applications, such as MIM devices.

One benefit of the helium ion beam direct writing is that, with this method, one can produce junctions with extremely small dimensions as can be seen from Figure 73. This would allow one to decrease the size of the superconducting nanoelectronic components in some cases, and opening up new possibilities to fabricate really small and sensitive measurement devices such as magnetometers, voltmeters and thermometers. Fabrication of many different kind of thermometers with dimensions of few tens of nanometers should be possible with this method: thermometry could be based on for example on Josephson junctions, SINIS-junctions or Coulomb blockade. Also really small resistive thermometers could be fabricated to cover a large temperature range using strong temperature dependence of localized electrons as in Ref. [54]. Ability to create small Josephson junctions in a fast and reproducible way with this method could also prove to be excellent approach to fabricate superconducting qubits for quantum computing.

As a conclusion, helium ion beam direct writing proved to be potentially extremely useful in many applications. Based on this project, there is evidence that fabrication of high quality Josephson junctions is possible with He-ion beam writing, enabling fabrication of devices otherwise difficult or impossible to fabricate.

References

[1] M. Tinkham, *Introduction to superconductivity*. Dover Publications, 2004, ISBN: 978-0-486-43503-9.

[2] S. Solve, R. Chayramy, M. Maruyama, C. Urano, N.-H. Kaneko and A. Rüfenacht, "Direct DC 10 v comparison between two programmable josephson voltage standards made of niobium nitride (NbN)-based and niobium (nb)-based josephson junctions", *Metrologia*, vol. 55, no. 2, pp. 302–313, 2018. DOI: 10.1088/1681-7575/aaac44.

[3] T. Faivre, D. Golubev and J. P. Pekola, "Josephson junction based thermometer and its application in bolometry", *Journal of Applied Physics*, vol. 116, no. 9, p. 094 302, 2014. DOI: 10.1063/1.4894516.

[4] Y.-F. Chen, D. Hover, S. Sendelbach, L. Maurer, S. T. Merkel, E. J. Pritchett, F. K. Wilhelm and R. McDermott, "Microwave Photon Counter Based on Josephson Junctions", *Phys. Rev. Lett.*, vol. 107, p. 217 401, 21 2011. DOI: 10.1103/PhysRevLett.107.217401.

[5] M. Nakahara and T. Ohmi, *Quantum computing: From linear algebra to physical realizations*. CRC Press, 2008, ISBN: 9781420012293.

[6] J. Clarke and F. K. Wilhelm, "Superconducting quantum bits", *Nature*, vol. 453, no. 7198, 1031–1042, 2008. DOI: 10.1038/nature07128.

[7] K. K. Likharev and V. K. Semenov, "RSFQ logic/memory family: a new Josephson-junction technology for sub-terahertz-clock-frequency digital systems", *IEEE Transactions on Applied Superconductivity*, vol. 1, no. 1, pp. 3–28, 1991. DOI: 10.1109/77.80745.

[8] J. K. Julin and I. J. Maasilta, "Applications and non-idealities of submicron Al–AlOx–Nb tunnel junctions", *Superconductor Science and Technology*, vol. 29, no. 10, p. 105 003, 2016. DOI: 10.1088/0953-2048/29/10/105003.

[9] H. Hilgenkamp and J. Mannhart, "Grain boundaries in high-Tc superconductors", *Rev. Mod. Phys.*, vol. 74, pp. 485–549, 2 May 2002. DOI: 10.1103/RevModPhys.74.485.

[10] S. K. Tolpygo, S. Shokhor, B. Nadgorny, J. Y. Lin, M. Gurvitch, A. Bourdillon, S. Y. Hou and J. M. Phillips, "High quality YBa2Cu3O7 Josephson junctions made by direct electron beam writing", *Applied Physics Letters*, vol. 63, no. 12, pp. 1696–1698, 1993. DOI: 10.1063/1.110688.

[11] A. J. Pauza, A. M. Campbell, D. F. Moore, R. E. Somekh and A. N. Broers, "High-T_c Josephson junctions by electron beam irradiation", *IEEE Transactions on Applied Superconductivity*, vol. 3, no. 1, pp. 2405–2408, 1993, ISSN: 1558-2515. DOI: 10.1109/77.233417.

[12] S. S. Tinchev, "Investigation of RF SQUIDs made from epitaxial YBCO films", *Superconductor Science and Technology*, vol. 3, no. 10, pp. 500–503, 1990. DOI: 10.1088/0953-2048/3/10/005.

[13] K. Chen, S. A. Cybart and R. C. Dynes, "Planar thin film YBa2Cu3O7-δ Josephson junction pairs and arrays via nanolithography and ion damage", *Applied Physics Letters*, vol. 85, no. 14, pp. 2863–2865, 2004. DOI: 10.1063/1.1803620.

[14] Carl Zeiss AG. (2020). ZEISS ORION NanoFab- microscope, [Online]. Available: https://www.zeiss.com/microscopy/int/products/multiple-ion-beam/orion-nanofab-for-materials.html (visited on 27th March 2020).

[15] S. A. Cybart, E. Y. Cho, T. J. Wong, B. H. Wehlin, M. K. Ma, C. Huynh and R. C. Dynes, "Nano Josephson superconducting tunnel junctions in YBa2Cu3O7-δ directly patterned with a focused helium ion beam", *Nature Nanotech*, vol. 10, pp. 598–602, 2015. DOI: 10.1038/nnano.2015.76.

[16] E. Y. Cho, M. K. Ma, C. Huynh, K. Pratt, D. N. Paulson, V. N. Glyantsev, R. C. Dynes and S. A. Cybart, "YBa2Cu3O7-δ superconducting quantum interference devices with metallic to insulating barriers written with a focused helium ion beam", *Applied Physics Letters*, vol. 106, no. 25, p. 252 601, 2015. DOI: 10.1063/1.4922640.

[17] E. Y. Cho, H. Li, J. C. LeFebvre, Y. W. Zhou, R. C. Dynes and S. A. Cybart, "Direct-coupled micro-magnetometer with Y-Ba-Cu-O nano-slit SQUID fabricated with a focused helium ion beam", *Applied Physics Letters*, vol. 113, no. 16, p. 162 602, 2018. DOI: 10.1063/1.5048776.

[18] B. Muller, M. Karrer, F. Limberger, M. Becker, B. Schroppel, C. Burkhardt, R. Kleiner, E. Goldobin and D. Koelle, "Josephson Junctions and SQUIDs Created by Focused Helium-Ion-Beam Irradiation of YBa2Cu3O7", *Phys. Rev. Applied*, vol. 11, p. 044 082, 4 April 2019. DOI: 10.1103/PhysRevApplied.11.044082.

[19] H. Li, H. Cai, E. Y. Cho, S. J. McCoy, Y.-T. Wang, J. C. LeFebvre, Y. W. Zhou and S. A. Cybart, "High-transition-temperature nanoscale superconducting quantum interference devices directly written with a focused helium ion beam", *Applied Physics Letters*, vol. 116, no. 7, p. 070 601, 2020. DOI: 10.1063/1.5143026.

[20] L. Kasaei, T. Melbourne, V. Manichev, L. C. Feldman, T. Gustafsson, K. Chen, X. X. Xi and B. A. Davidson, "MgB2 Josephson junctions produced by focused helium ion beam irradiation", *AIP Advances*, vol. 8, no. 7, p. 075 020, 2018. DOI: 10.1063/1.5030751.

[21] K. Prikhodko, B. Gurovich and M. Dement'eva, "Study of phase transitions in NbN ultrathin films under composite ion beam irradiation", *IOP Conference Series: Materials Science and Engineering*, vol. 130, p. 012 046, 2016. DOI: 10.1088/1757-899x/130/1/012046.

[22] G. D. Martinez, D. Buckley, I. Charaev, A. Dane, D. E. Dow and K. K. Berggren, *Superconducting Nanowire Fabrication on Niobium Nitride using Helium Ion Irradiation*, 2020. arXiv: 2003.02898 [cond-mat.supr-con].

[23] J. Bardeen, L. N. Cooper and J. R. Schrieffer, "Microscopic Theory of Superconductivity", *Phys. Rev.*, vol. 106, pp. 162–164, 1 1957. DOI: 10.1103/PhysRev.106.162.

[24] T. T. Heikkilä, *The Physics of Nanoelectronics: Transport and Fluctuation Phenomena at Low Temperatures*. Oxford University Press, 2013, ISBN: 978-0-19-959244-9.

[25] P. Coleman, *Introduction to many-body physics*. Cambridge University Press, 2015, ISBN: 9780521864886.

[26] R. C. Dynes, V. Narayanamurti and J. P. Garno, "Direct Measurement of Quasiparticle-Lifetime Broadening in a Strong-Coupled Superconductor",

Phys. Rev. Lett., vol. 41, pp. 1509–1512, 21 1978. DOI: 10.1103/PhysRevLett.41.1509.

[27] Lei Yu, N. Newman and J. M. Rowell, "Measurement of the coherence length of sputtered Nb0.62Ti0.38N thin films", *IEEE Transactions on Applied Superconductivity*, vol. 12, no. 2, pp. 1795–1798, 2002. DOI: 10.1109/TASC.2002.1020339.

[28] A. Y. Mironov, S. V. Postolova and D. A. Nasimov, "Superconducting Properties of Long TiN Wires", *Jetp letters*, vol. 104, no. 11, 766–770, 2016. DOI: 10.1134/S0021364016230107.

[29] B. Josephson, "Possible new effects in superconductive tunnelling", *Physics Letters*, vol. 1, no. 7, pp. 251–253, 1962, ISSN: 0031-9163. DOI: 10.1016/0031-9163(62)91369-0.

[30] M. Tinkham, "Tunneling Generation, Relaxation, and Tunneling Detection of Hole-Electron Imbalance in Superconductors", *Phys. Rev. B*, vol. 6, pp. 1747–1756, 5 1972. DOI: 10.1103/PhysRevB.6.1747.

[31] V. Ambegaokar and A. Baratoff, "Tunneling Between Superconductors", *Phys. Rev. Lett.*, vol. 10, pp. 486–489, 11 1963. DOI: 10.1103/PhysRevLett.10.486.

[32] H. Courtois, M. Meschke, J. T. Peltonen and J. P. Pekola, "Origin of Hysteresis in a Proximity Josephson Junction", *Phys. Rev. Lett.*, vol. 101, p. 067 002, 6 2008. DOI: 10.1103/PhysRevLett.101.067002.

[33] K. K. Likharev, "Superconducting weak links", *Rev. Mod. Phys.*, vol. 51, pp. 101–159, 1 1979. DOI: 10.1103/RevModPhys.51.101.

[34] A. B. Kaul, S. R. Whiteley, T. Van Duzer, L. Yu, N. Newman and J. M. Rowell, "Internally shunted sputtered NbN Josephson junctions with a TaNx barrier for nonlatching logic applications", *Applied Physics Letters*, vol. 78, no. 1, pp. 99–101, 2001. DOI: 10.1063/1.1337630.

[35] Y. V. Nazarov and Y. M. Blanter, *Quantum Transport: Introduction to Nanoscience*. Cambridge University Press, 2009. DOI: 10.1017/CBO9780511626906.

[36] S. Mahapatra and A. M. Ionescu, "Realization of multiple valued logic and memory by hybrid setmos architecture", *IEEE Transactions on Nanotechnology*, vol. 4, no. 6, pp. 705–714, 2005. DOI: 10.1109/TNANO.2005.858602.

[37] P. S. Kumar Karre, P. L. Bergstrom, M. Govind and S. P. Karna, "Single Electron Transistor Fabrication using Focused Ion Beam direct write technique", in *The 17th Annual SEMI/IEEE ASMC 2006 Conference*, 2006, pp. 221–224. DOI: 10.1109/ASMC.2006.1638756.

[38] IONS4SET. (2020). IONS4SET H2020 European Project, [Online]. Available: http://www.ions4set.eu/ (visited on 28th Jun. 2020).

[39] K. K. Likharev, "Single-electron devices and their applications", *Proceedings of the IEEE*, vol. 87, no. 4, pp. 606–632, 1999. DOI: 10.1109/5.752518.

[40] D. Ephron, Y. Xu and M. R. Beasley, "Observation of Coulomb correlations of resonant tunneling and inelastic hopping", *Phys. Rev. Lett.*, vol. 69, pp. 3112–3115, 21 1992. DOI: 10.1103/PhysRevLett.69.3112.

[41] H. Bahlouli, K. A. Matveev, D. Ephron and M. R. Beasley, "Coulumb correlations in hopping through a thin layer", *Phys. Rev. B*, vol. 49, pp. 14 496–14 503, 20 1994. DOI: 10.1103/PhysRevB.49.14496.

[42] G.-L. Ingold and Y. V. Nazarov, *Charge Tunneling Rates in Ultrasmall Junctions*, 2005. arXiv: cond-mat/0508728 [cond-mat.mes-hall].

[43] J. G. Simmons, "Generalized Formula for the Electric Tunnel Effect between Similar Electrodes Separated by a Thin Insulating Film", *Journal of Applied Physics*, vol. 34, no. 6, pp. 1793–1803, 1963. DOI: 10.1063/1.1702682.

[44] K. Gloos, P. J. Koppinen and J. P. Pekola, "Properties of native ultrathin aluminium oxide tunnel barriers", *Journal of Physics: Condensed Matter*, vol. 15, no. 10, pp. 1733–1746, 2003. DOI: 10.1088/0953-8984/15/10/320.

[45] M. Vojta, "Quantum phase transitions", *Reports on Progress in Physics*, vol. 66, no. 12, pp. 2069–2110, 2003. DOI: 10.1088/0034-4885/66/12/r01.

[46] G. Viera, M. Mikikian, E. Bertran, P. R. i. Cabarrocas and L. Boufendi, "Atomic structure of the nanocrystalline Si particles appearing in nanostructured Si thin films produced in low-temperature radiofrequency plasmas", *Journal of Applied Physics*, vol. 92, no. 8, pp. 4684–4694, 2002. DOI: 10.1063/1.1506382.

[47] P. A. Lee and T. V. Ramakrishnan, "Disordered electronic systems", *Rev. Mod. Phys.*, vol. 57, pp. 287–337, 2 1985. DOI: 10.1103/RevModPhys.57.287.

[48] C. Marrache-Kikuchi, "Dimensionality effects in a disordered system in the vicinity of the Superconductor-to-Insulator Transition", PhD thesis, Université Paris Sud - Paris XI, 2014. [Online]. Available: https://tel.archives-ouvertes.fr/tel-00929767.

[49] P. W. Anderson, "Absence of Diffusion in Certain Random Lattices", *Phys. Rev.*, vol. 109, pp. 1492–1505, 5 1958. DOI: 10.1103/PhysRev.109.1492.

[50] N. F. Mott, "The basis of the electron theory of metals, with special reference to the transition metals", *Proceedings of the Physical Society. Section A*, vol. 62, no. 7, pp. 416–422, 1949. DOI: 10.1088/0370-1298/62/7/303.

[51] D. Basko, I. Aleiner and B. Altshuler, "Metal–insulator transition in a weakly interacting many-electron system with localized single-particle states", *Annals of Physics*, vol. 321, no. 5, pp. 1126–1205, 2006, ISSN: 0003-4916. DOI: 10.1016/j.aop.2005.11.014.

[52] P. Phillips and D. Dalidovich, "The Elusive Bose Metal", vol. 302, no. 5643, pp. 243–247, 2003. DOI: 10.1126/science.1088253.

[53] H. Ibach and H. Lüth, *Solid-State Physics: An Introduction to Principles of Materials Science*. Springer-Verlag Berlin Heidelberg, 2009, ISBN: 9783540938040.

[54] T. Nguyen, A. Tavakoli, S. Triqueneaux, R. Swami, A. Ruhtinas, J. Gradel, P. Garcia-Campos, K. Hasselbach, A. Frydman, B. Piot, M. Gibert, E. Collin and O. Bourgeois, "Niobium Nitride Thin Films for Very Low Temperature Resistive Thermometry", *Journal of Low Temperature Physics*, vol. 197, pp. 348–356, August 2019. DOI: 10.1007/s10909-019-02222-6.

[55] A. L. Efros and B. I. Shklovskii, "Coulomb gap and low temperature conductivity of disordered systems", *Journal of Physics C: Solid State Physics*, vol. 8, no. 4, pp. L49–L51, 1975. DOI: 10.1088/0022-3719/8/4/003.

[56] P. Anderson, "Theory of dirty superconductors", *Journal of Physics and Chemistry of Solids*, vol. 11, no. 1, pp. 26–30, 1959, ISSN: 0022-3697. DOI: 10.1016/0022-3697(59)90036-8.

[57] V. F. Gantmakher and V. T. Dolgopolov, "Superconductor-insulator quantum phase transition", *Physics-Uspekhi*, vol. 53, no. 1, pp. 1–49, 2010. DOI: 10.3367/ufne.0180.201001a.0003.

[58] Y.-H. Lin, J. Nelson and A. Goldman, "Superconductivity of very thin films: The superconductor–insulator transition", *Physica C: Superconductivity and its Applications*, vol. 514, pp. 130–141, 2015, ISSN: 0921-4534. DOI: 10.1016/j.physc.2015.01.005.

[59] D. B. Haviland, Y. Liu and A. M. Goldman, "Onset of superconductivity in the two-dimensional limit", *Phys. Rev. Lett.*, vol. 62, pp. 2180–2183, 18 1989. DOI: 10.1103/PhysRevLett.62.2180.

[60] A. Larkin, "Superconductor-insulator transitions in films and bulk materials", *Annalen der Physik*, vol. 8, no. 7-9, pp. 785–794, 1999. DOI: 10.1002/(SICI)1521-3889(199911)8:7/9<785::AID-ANDP785>3.0.CO;2-3.

[61] M. P. A. Fisher, P. B. Weichman, G. Grinstein and D. S. Fisher, "Boson localization and the superfluid-insulator transition", *Phys. Rev. B*, vol. 40, pp. 546–570, 1 1989. DOI: 10.1103/PhysRevB.40.546.

[62] K. Efetov, "Phase Transition in Granulated Superconductors", *Sov.Phys.JETP*, vol. 51, no. 5, pp. 1015–1022, 1980. [Online]. Available: http://www.jetp.ac.ru/cgi-bin/e/index/e/51/5/p1015?a=list.

[63] A. Gold, "Impurity-induced phase transition in the interacting Bose gas: 1. Analytical results", *Z. Physik B - Condensed Matter*, vol. 52, pp. 1–8, 1983. DOI: 10.1007/BF01305892.

[64] B. Sacépé, T. Dubouchet, C. Chapelier, M. Sanquer, M. Ovadia, D. Shahar, M. Feigel'man and L. Ioffe, "Localization of preformed cooper pairs in disordered superconductors", *Nature Physics*, vol. 7, pp. 239–244, 2011. DOI: 10.1038/nphys1892.

[65] V. M. Vinokur, T. I. Baturina, M. V. Fistul, A. Y. Mironov, M. R. Baklanov and C. Strunk, "Superinsulator and quantum synchronization", *NATURE*, vol. 452, no. 7187, 613–U5, APR 3 2008. DOI: 10.1038/nature06837.

[66] A. Finkel'stein, "Suppression of superconductivity in homogeneously disordered systems", *Physica B: Condensed Matter*, vol. 197, no. 1, pp. 636–648, 1994, ISSN: 0921-4526. DOI: 10.1016/0921-4526(94)90267-4.

[67] ——, "Metal-insulator transition in a disordered system", *Sov.Phys.JETP*, vol. 59, no. 1, p. 212, 1984. [Online]. Available: http://www.jetp.ac.ru/cgi-bin/e/index/e/59/1/p212?a=list.

[68] B. Sacepe, C. Chapelier, T. I. Baturina, V. M. Vinokur, M. R. Baklanov and M. Sanquer, "Disorder-Induced Inhomogeneities of the Superconducting State Close to the Superconductor-Insulator Transition", *PHYSICAL REVIEW LETTERS*, vol. 101, no. 15, 2008. DOI: 10.1103/PhysRevLett.101.157006.

[69] M. Feigel'man, L. Ioffe, V. Kravtsov and E. Cuevas, "Fractal superconductivity near localization threshold", *Annals of Physics*, vol. 325, no. 7, pp. 1390–1478, 2010, ISSN: 0003-4916. DOI: 10.1016/j.aop.2010.04.001.

[70] T. I. Baturina, C. Strunk, M. R. Baklanov and A. Satta, "Quantum Metallicity on the High-Field Side of the Superconductor-Insulator Transition", *Phys. Rev. Lett.*, vol. 98, p. 127 003, 12 2007. DOI: 10.1103/PhysRevLett.98.127003.

[71] J. Ziegler. (2013). SRIM and TRIM website, [Online]. Available: http://www.srim.org (visited on 23rd March 2020).

[72] R. Ropp, *Encyclopedia of the Alkaline Earth Compounds*, R. Ropp, Ed. Elsevier, 2013, ISBN: 978-0-444-59550-8. DOI: 10.1016/B978-0-444-59550-8.00003-X.

[73] ChemicalBook. (2016). Chemical Book website, [Online]. Available: https://www.chemicalbook.com/ChemicalProductProperty_EN_CB6761156.htm (visited on 23rd March 2020).

[74] A. Torgovkin, S. Chaudhuri, A. Ruhtinas, M. Lahtinen, T. Sajavaara and I. J. Maasilta, "High quality superconducting titanium nitride thin film growth using infrared pulsed laser deposition", *Superconductor Science and Technology*, vol. 31, no. 5, p. 055 017, April 2018. DOI: 10.1088/1361-6668/aab7d6.

[75] J. F. Shackelford, Y.-H. Han, S. Kim and S.-H. Kwon, *CRC Materials Science and Engineering Handbook*. CRC Press, 2015, ISBN: 9781482216530.

[76] M. Guziewicz, A. Laszcz, J. Domagala, K. Golaszewska, J. Ratajczak, R. Kruszka, M. Juchniewicz, A. Czerwinski and W. Slysz, "Structural analysis of epitaxial NbTiN films", *Proc SPIE*, vol. 8902, Jul. 2013. DOI: 10.1117/12.2031303.

[77] A. Veen, H. Schut, A. Fedorov, F. Labohm, E. Neeft and R. Konings, "The formation of microvoids in MgO by helium ion implantation and thermal annealing", *NUCL INSTRUM METH PHYS RES B*, vol. 148, pp. 768–772, 1999. DOI: 10.1016/S0168-583X(98)00853-2.

[78] D.-D. McAlevy Bubb and R. F. Haglund Jr., *Pulsed laser deposition of thin films*. John Wiley and Sons, Ltd, 2006, ISBN: 9780470052129.

[79] J. Schou, "Physical aspects of the pulsed laser deposition technique: The stoichiometric transfer of material from target to film", *Applied Surface Science*, vol. 255, no. 10, pp. 5191–5198, 2009, Laser and Plasma in Micro- and Nano-Scale Materials Processing and Diagnostics, ISSN: 0169-4332. DOI: 10.1016/j.apsusc.2008.10.101.

[80] S. Amoruso, "Modeling of UV pulsed-laser ablation of metallic targets", *Applied Physics A: Materials Science and Processing*, vol. 69, no. 3, pp. 323–332, 1999. DOI: 10.1007/s003390051008.

[81] D. von der Linde and K. Sokolowski-Tinten, "The physical mechanisms of short-pulse laser ablation", *Applied Surface Science*, vol. 154-155, pp. 1–10, 2000, ISSN: 0169-4332. DOI: https://doi.org/10.1016/S0169-4332(99)00440-7.

[82] S. Chaudhuri, M. R. Nevala, T. Hakkarainen, T. Niemi and I. J. Maasilta, "Infrared pulsed laser deposition of niobium nitride thin films", *IEEE Transactions on Applied Superconductivity*, vol. 21, no. 3, pp. 143–146, 2011. DOI: 10.1109/TASC.2010.2081656.

[83] S. Chaudhuri, I. J. Maasilta, L. Chandernagor, M. Ging and M. Lahtinen, "Fabrication of superconducting tantalum nitride thin films using infrared pulsed laser deposition", *Journal of Vacuum Science & Technology A*, vol. 31, no. 6, p. 061 502, 2013. DOI: 10.1116/1.4812698.

[84] A. Ruhtinas. (2019). PLD control software repository, [Online]. Available: https://github.com/akperuht/pldcontrol (visited on 11th Jun. 2019).

[85] R. Hill, J. A. Notte and L. Scipioni, *Chapter 2 - scanning helium ion microscopy*, P. W. Hawkes, Ed., ser. Advances in Imaging and Electron Physics. Elsevier, 2012, vol. 170, pp. 65–148. DOI: 10.1016/B978-0-12-394396-5.00002-6.

[86] W. Spengler, R. Kaiser, A. N. Christensen and G. Müller-Vogt, "Raman scattering, superconductivity, and phonon density of states of stoichiometric and nonstoichiometric TiN", *Phys. Rev. B*, vol. 17, pp. 1095–1101, 3 1978. DOI: 10.1103/PhysRevB.17.1095.

[87] S. Zhang and W. Zhu, "TiN coating of tool steels: A review", *Journal of Materials Processing Technology*, vol. 39, no. 1, pp. 165–177, 1993, ISSN: 0924-0136. DOI: 10.1016/0924-0136(93)90016-Y.

[88] H. Ito, R. P. van Hove, I. N. Sierevelt, B. J. van Royen and P. A. Nolte, "Titanium-Nitride Coating of Orthopaedic Implants: A Review of the Literature", *BioMed Research International*, 2015, ISSN: 2314-6133. DOI: 10.1155/2015/485975.

[89] L. Gao, J. Gstöttner, R. Emling, M. Balden, C. Linsmeier, A. Wiltner, W. Hansch and D. Schmitt-Landsiedel, "Thermal stability of titanium nitride diffusion barrier films for advanced silver interconnects", *Microelectronic Engineering*, vol. 76, no. 1, pp. 76–81, 2004, Materials for Advanced Metallization 2004, ISSN: 0167-9317. DOI: 10.1016/j.mee.2004.07.020.

[90] L. Lima, J. Diniz, I. Doi and J. [Fo], "Titanium nitride as electrode for MOS technology and Schottky diode: Alternative extraction method of titanium nitride work function", *Microelectronic Engineering*, vol. 92, pp. 86–90, 2012, 27th Annual Advanced Metallization Conference 2010, ISSN: 0167-9317. DOI: 10.1016/j.mee.2011.04.059.

[91] S. Ohya, B. Chiaro, A. Megrant, C. Neill, R. Barends, Y. Chen, J. Kelly, D. Low, J. Mutus, P. J. J. O'Malley, P. Roushan, D. Sank, A. Vainsencher, J. Wenner, T. C. White, Y. Yin, B. D. Schultz, C. J. Palmstrøm, B. A. Mazin, A. N. Cleland and J. M. Martinis, "Room temperature deposition of sputtered TiN films for superconducting coplanar waveguide resonators", *Superconductor Science and Technology*, vol. 27, no. 1, p. 015 009, 2013. DOI: 10.1088/0953-2048/27/1/015009.

[92] J. B. Chang, M. R. Vissers, A. D. Córcoles, M. Sandberg, J. Gao, D. W. Abraham, J. M. Chow, J. M. Gambetta, M. Beth Rothwell, G. A. Keefe, M. Steffen and D. P. Pappas, "Improved superconducting qubit coherence using titanium nitride", *Applied Physics Letters*, vol. 103, no. 1, p. 012 602, 2013. DOI: 10.1063/1.4813269.

[93] P. Diener, H. Leduc, S. Yates, Y. Lankwarden and J. Baselmans, "Design and Testing of Kinetic Inductance Detectors Made of Titanium Nitride", *Journal of Low Temperature Physics*, vol. 167, Sep. 2013. DOI: 10.1007/s10909-012-0484-z.

[94] H. G. Leduc, B. Bumble, P. K. Day, B. H. Eom, J. Gao, S. Golwala, B. A. Mazin, S. McHugh, A. Merrill, D. C. Moore, O. Noroozian, A. D. Turner and J. Zmuidzinas, "Titanium nitride films for ultrasensitive microresonator detectors", *Applied Physics Letters*, vol. 97, no. 10, p. 102 509, 2010. DOI: 10.1063/1.3480420.

[95] N. Hadacek, M. Sanquer and J.-C. Villégier, "Double reentrant superconductor-insulator transition in thin TiN films", *Phys. Rev. B*, vol. 69, p. 024 505, 2 2004. DOI: 10.1103/PhysRevB.69.024505.

[96] E. F. C. Driessen, P. C. J. J. Coumou, R. R. Tromp, P. J. de Visser and T. M. Klapwijk, "Strongly Disordered TiN and NbTiN s-Wave Superconductors Probed by Microwave Electrodynamics", *PHYSICAL REVIEW LETTERS*, vol. 109, no. 10, 2012. DOI: 10.1103/PhysRevLett.109.107003.

[97] B. Sacepe, T. Dubouchet, C. Chapelier, M. Sanquer, M. Ovadia, D. Shahar, M. Feigel'man and L. Ioffe, "Localization of preformed Cooper pairs in disordered superconductors", *Nature Physics*, vol. 7, no. 3, 239–244, 2011. DOI: 10.1038/NPHYS1892.

[98] T. I. Baturina and V. M. Vinokur, "Superinsulator–superconductor duality in two dimensions", *Annals of Physics*, vol. 331, pp. 236–257, 2013, ISSN: 0003-4916. DOI: 10.1016/j.aop.2012.12.007.

[99] R. Ningthoujam and N. Gajbhiye, "Synthesis, electron transport properties of transition metal nitrides and applications", *Progress in Materials Science*, vol. 70, pp. 50–154, 2015, ISSN: 0079-6425. DOI: 10.1016/j.pmatsci.2014.11.004.

[100] J. Olaya, S. Rodil and S. Muhl, "Comparative study of niobium nitride coatings deposited by unbalanced and balanced magnetron sputtering", *Thin Solid Films*, vol. 516, no. 23, pp. 8319–8326, 2008, ISSN: 0040-6090. DOI: 10.1016/j.tsf.2008.03.043.

[101] R. Romestain, B. Delaet, P. Renaud-Goud, I. Wang, C. Jorel, J.-C. Villegier and J.-P. Poizat, "Fabrication of a superconducting niobium nitride hot electron bolometer for single-photon counting", *New Journal of Physics*, vol. 6, pp. 129–129, October 2004. DOI: 10.1088/1367-2630/6/1/129.

[102] S. Chaudhuri, M. R. Nevala and I. J. Maasilta, "Niobium nitride-based normal metal-insulator-superconductor tunnel junction microthermometer", *Applied Physics Letters*, vol. 102, no. 13, p. 132 601, 2013. DOI: 10.1063/1.4800440.

[103] R. Cheng, S. Wang and H. X. Tang, "Superconducting nanowire single-photon detectors fabricated from atomic-layer-deposited NbN", *Applied Physics Letters*, vol. 115, no. 24, p. 241 101, 2019. DOI: 10.1063/1.5131664.

[104] M. Mondal, M. Chand, A. Kamlapure, J. Jesudasan, V. C. Bagwe, S. Kumar, G. Saraswat, V. Tripathi and P. Raychaudhuri, "Phase Diagram and Upper Critical Field of Homogeneously Disordered Epitaxial 3-Dimensional NbN Films", *Journal of Superconductivity and Novel Magnetism*, vol. 24, no. 1-2, 341–344, 2011. DOI: 10.1007/s10948-010-1038-8.

[105] J. Yong, T. R. Lemberger, L. Benfatto, K. Ilin and M. Siegel, "Robustness of the Berezinskii-Kosterlitz-Thouless transition in ultrathin NbN films near the superconductor-insulator transition", *Phys. Rev. B*, vol. 87, p. 184 505, 18 2013. DOI: 10.1103/PhysRevB.87.184505.

[106] Y. Noat, V. Cherkez, C. Brun, T. Cren, C. Carbillet, F. Debontridder, K. Ilin, M. Siegel, A. Semenov, H.-W. Hübers and D. Roditchev, "Unconventional superconductivity in ultrathin superconducting NbN films studied by scanning tunneling spectroscopy", *Phys. Rev. B*, vol. 88, p. 014 503, 1 2013. DOI: 10.1103/PhysRevB.88.014503.

[107] K. Makise, T. Odou, S. Ezaki, T. Asano and B. Shinozaki, "Superconductor–insulator transition in two-dimensional NbN/MgO and NbN/AlN/MgO films", *Materials Research Express*, vol. 2, no. 10, p. 106 001, 2015. DOI: 10.1088/2053-1591/2/10/106001.

[108] S. Ezaki, K. Makise, B. Shinozaki, T. Odo, T. Asano, H. Terai, T. Yamashita, S. Miki and Z. Wang, "Localization and interaction effects in ultrathin epitaxial NbN superconducting films", *Journal of Physics: Condensed Matter*, vol. 24, no. 47, p. 475 702, 2012. DOI: 10.1088/0953-8984/24/47/475702.

[109] H. M. Jaeger, D. B. Haviland, B. G. Orr and A. M. Goldman, "Onset of superconductivity in ultrathin granular metal films", *Phys. Rev. B*, vol. 40, pp. 182–196, 1 1989. DOI: 10.1103/PhysRevB.40.182.

[110] A. G. Sivakov, A. M. Glukhov, A. N. Omelyanchouk, Y. Koval, P. Müller and A. V. Ustinov, "Josephson Behavior of Phase-Slip Lines in Wide Superconducting Strips", *Phys. Rev. Lett.*, vol. 91, p. 267 001, 26 2003. DOI: 10.1103/PhysRevLett.91.267001.

[111] D. A. Bennett, D. R. Schmidt, D. S. Swetz and J. N. Ullom, "Phase-slip lines as a resistance mechanism in transition-edge sensors", *Applied Physics Letters*, vol. 104, no. 4, p. 042 602, 2014. DOI: 10.1063/1.4863664.

[112] R. D. Leo, A. Nigro, G. Nobile and R. Vaglio, "Niobium-titanium nitride thin films for superconducting rf accelerator cavities", *Journal of Low Temperature Physics*, vol. 78, 41–50, 1990. DOI: 10.1007/BF00682108.

[113] C. M. Yen, L. E. Toth, Y. M. Shy, D. E. Anderson and L. G. Rosner, "Superconducting Hc-Jc and Tc Measurements in the Nb–Ti–N, Nb–Hf–N, and Nb–V–N Ternary Systems", *Journal of Applied Physics*, vol. 38, no. 5, pp. 2268–2271, 1967. DOI: 10.1063/1.1709868.

[114] B. D. Jackson, G. de Lange, T. Zijlstra, M. Kroug, T. M. Klapwijk and J. A. Stern, "Niobium titanium nitride-based superconductor-insulator-superconductor mixers for low-noise terahertz receivers", *Journal of Applied Physics*, vol. 97, no. 11, p. 113 904, 2005. DOI: 10.1063/1.1927281.

[115] X. Yang, L. You, L. Zhang, C. Lv, H. Li, X. Liu, H. Zhou and Z. Wang, "Comparison of Superconducting Nanowire Single-Photon Detectors Made of NbTiN and NbN Thin Films", *IEEE Transactions on Applied Superconductivity*, vol. 28, no. 1, pp. 1–6, 2018. DOI: 10.1109/TASC.2017.2776288.

[116] A. Y. Mironov, D. M. Silevitch, T. Proslier, S. V. Postolova, M. V. Burdastyh, A. K. Gutakovskii, T. F. Rosenbaum, V. V. Vinokur and T. I. Baturina, "Charge Berezinskii-Kosterlitz-Thouless transition in superconducting NbTiN films", *Scientific Reports*, vol. 8, no. 1, p. 4082, 2018, ISSN: 2045-2322. DOI: 10.1038/s41598-018-22451-1.

[117] M. V. Burdastyh, S. V. Postolova, T. I. Baturina, T. Proslier, V. M. Vinokur and A. Y. Mironova, "Superconductor–Insulator Transition in NbTiN Films", *JETP LETTERS*, vol. 106, 749–753, 2017. DOI: 10.1134/S0021364017230060.

[118] M. V. Burdastyh, S. V. Postolova, T. Proslier, S. S. Ustavshikov, A. V. Antonov, V. M. Vinokur and A. Y. Mironova, "Superconducting phase transitions in disordered NbTiN films", *Scientific Reports*, vol. 10, p. 1471, 2020. DOI: 10.1038/s41598-020-58192-3.

[119] A. A. Golubov, E. P. Houwman, J. G. Gijsbertsen, V. M. Krasnov, J. Flokstra, H. Rogalla and M. Y. Kupriyanov, "Proximity effect in superconductor-insulator-superconductor Josephson tunnel junctions: Theory and experiment", *Phys. Rev. B*, vol. 51, pp. 1073–1089, 2 1995. DOI: 10.1103/PhysRevB.51.1073.

[120] A. Golubov, M. Gurvich, M. Kupriyanov and S. Polonskii, "Josephson effect in tunnelling SS'IS'S structures", *ZHURNAL EKSPERIMENTALNOI I TEORETICHESKOI FIZIKI*, vol. 103, no. 5, 1851–1868, 1993.

A Appendices

A.1 Uncertainty calculation

If uncertainties are assumed to be independent, propagates in calculation in following manner:

$$\delta q = \sqrt{\sum_i \left(\frac{\partial q}{\partial x_i} \delta x_i \right)^2} \tag{56}$$

where q is a function of independent variables x_i and δx_i are uncertainties of the variables. When applied to sheet resistance formula (Eq. 35) one gets

$$\delta R_\square = \sqrt{\left(\frac{w}{l} \delta r \right)^2 + \left(\frac{R}{l} \delta w \right)^2 + \left(\frac{Rw}{l^2} \delta l \right)^2}. \tag{57}$$

Respectively, resistivity ρ is $R_\square$ multiplied by thickness t, and thus uncertainty of resistivity is

$$\delta \rho = \sqrt{\left(\frac{wt}{l} \delta r \right)^2 + \left(\frac{Rt}{l} \delta w \right)^2 + \left(\frac{Rwt}{l^2} \delta l \right)^2 + \left(\frac{Rw}{l} \delta t \right)^2}. \tag{58}$$

A.2 Figures

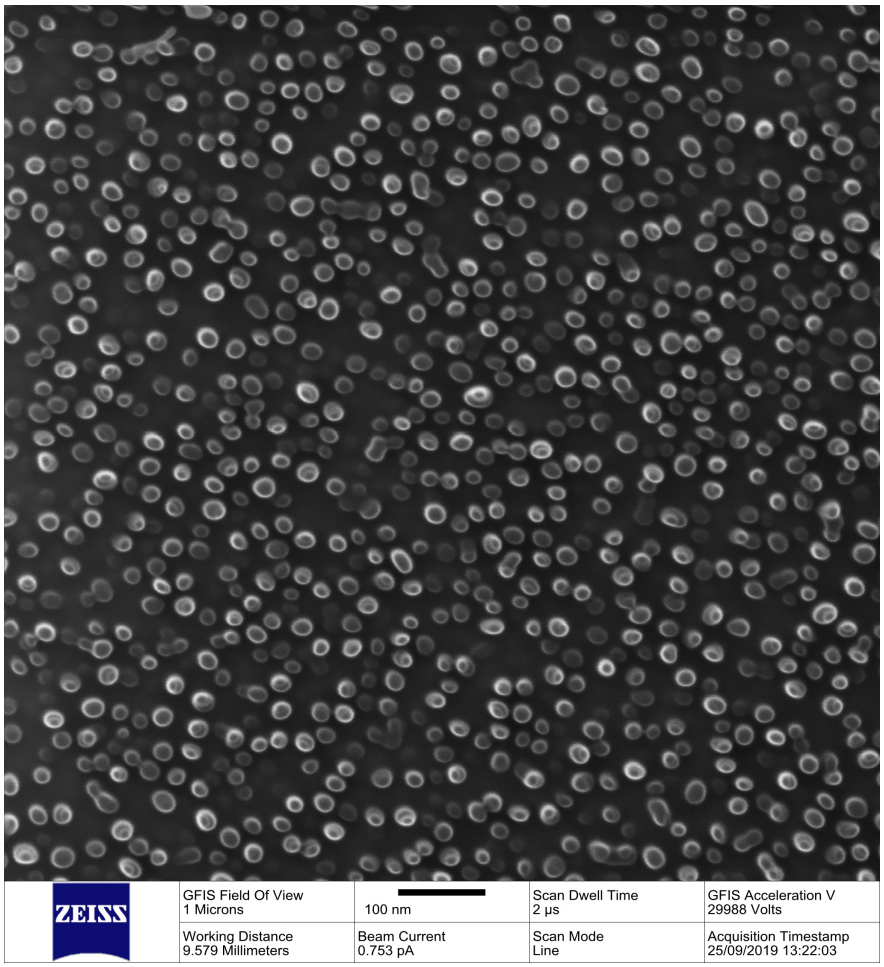

Figure 74. Nanoparticles on top of N72 film. Particles were only at some areas, and on top of the actual junctions there were none. Origin and composition of these particles is unknown.

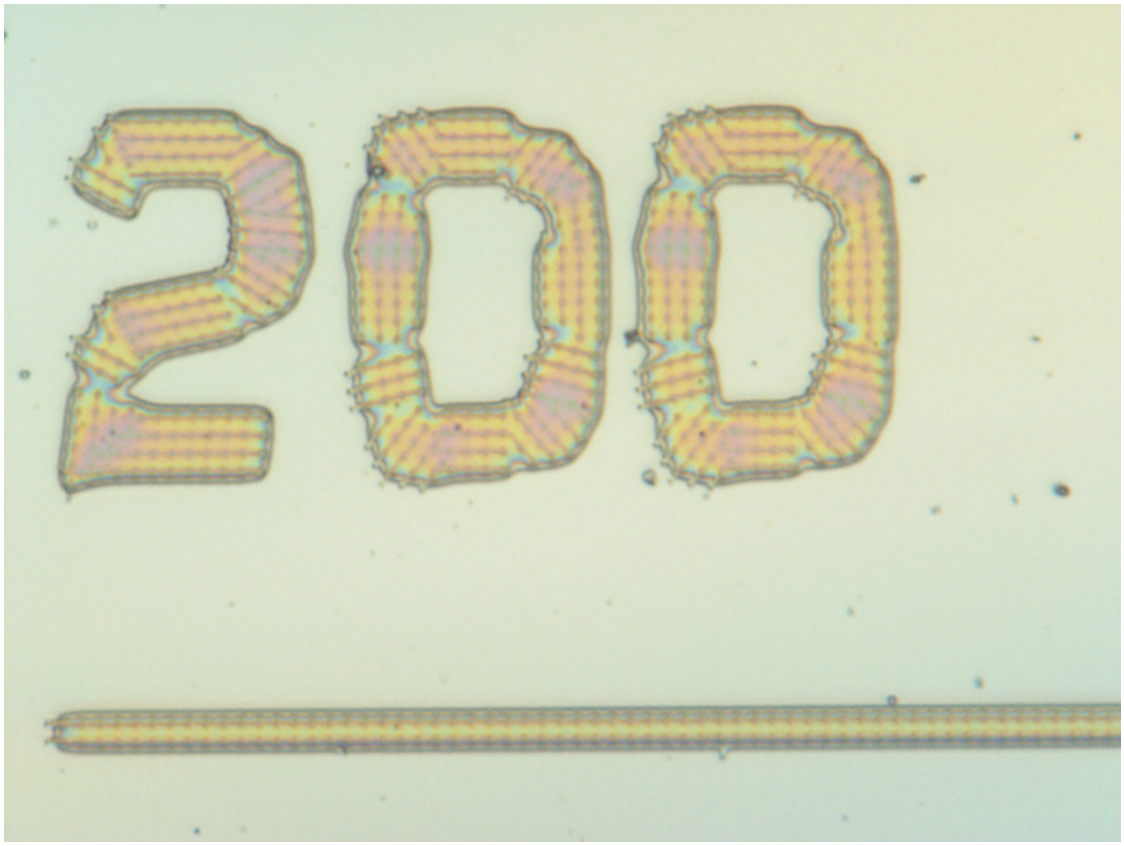

Figure 75. Negative resist after electron beam lithography and development. Patterning generator has applied larger doses to some lines. This behaviour was observed only in very few occasions, and probably there was something wrong with lithography parameters in these cases.